

An aerial photograph of a river system. The river is dark green, flowing from the top right towards the bottom left. Along the left bank, there are several small, curved, submerged structures (groynes) made of light-colored material, likely stone or concrete. The right bank features a large, prominent, light-colored sandbar or shoal. The surrounding landscape is green, with fields and some trees. A road or path runs parallel to the river on the left side.

# Physical modelling of submerged groynes

J.M. Harms  
July 2021



# Physical modelling of submerged groynes

By

Johan M. Harms

In partial fulfilment of the requirements for the degree of

**Master of Science**  
in Civil Engineering

At the Delft University of Technology  
to be defended publicly on Thursday July 29, 2021 at 14:30

Supervisor:	Prof. dr. ir. Wim Uijtewaal	TU Delft
Thesis committee:	Dr. ir. Jeremy Bricker	TU Delft
	Dr. ir. Erik Mosselman	TU Delft
	Dr. ir. Burhan Yildiz	TU Delft
	Dr. ir. Bas Hofland	TU Delft
	Dr. ir. Arjan Sieben	Rijkswaterstaat
	Dr. ir. Mohammed Yossef	Deltares

An electronic version of this thesis is available at <http://repository.tudelft.nl/>.



## Preface

Before you lies the master thesis 'Physical modelling of submerged groynes', which report on measurements of flow in a physical model. It has been written to the partial fulfilment of the graduation requirement of master of Hydraulic Engineering at the Delft University of Technology. I was engaged in research and writing this thesis report from September 2020 to July 2021.

Most of the research was done at the hydraulic laboratory of the Faculty of Civil Engineering and Geoscience. The research was challenging, especially with restriction due to Covid, which severely limited some of the works in the laboratory. But with a bit of patience all measurements that were required for answering the questions that I identified could be done.

This paper is part of a wider research on the flow over submerged groynes, in which I was privileged to have a large committee of committed supervisors all giving valuable feedback and helping me along with their professional knowledge. I would like to thank my supervisor Wim Uijttewaal for his critical feedback and many discussions on the interpretation of the observed flow, and Burhan Yildiz<sup>1</sup> for his help in setting up the experiments and helping me many times with the execution of measurements. I would like to my other supervisors for their excellent guidance and support during the process, and all contributed to the report you have before you. I would also like to thank the lab personal, Arno, Pieter and Chantal, who helped me with so many things and allowed me to perform the measurements, and keep me company during the lonely hours in the lab during Covid. A special thanks is for my wife, who kept me motivated on the journey and helped me along during the long hours of work I needed to write this paper.

I hope you enjoy your reading.

Johan Harms

---

<sup>1</sup> Burhan Yildiz is granted a scholarship for his Post Doc study funded by TUBITAK from Turkey.

## Summary

Currently multiple projects investigate the effect of lowering the crest of groynes in the Dutch rivers with the aim to lower the backwater effect of groynes under high water levels. There is a major uncertainty however in the modelling of groynes, and therefore in the prediction of the effect of groyne lowering. Currently submerged groynes are modelled subgrid as weirs. The flow processes differ however between groynes and weirs as discharge over a groyne is not purely defined by the contraction and expansion over the groyne, but also by lateral shear and interaction with the surrounding main channel and floodplain. The result is a lower resistance of the cross section than expected from weir modelling. For this reason a numerical investigation was started, comparing the modelling of groynes as different subgrid weirs in a 2D model and the modelling of groynes included in the bed topography in a 3D (non-)hydrostatic model. There were large differences between all different methods of groyne modelling. Furthermore the available experimental data did not suffice to explain the differences.

For that reason a new physical model has been set up in the Delft University of Technology, at the hydraulic laboratory of the Faculty of Civil Engineering and Geoscience. The experiment includes a 1:30 scale model of a representative transect of the Waal river. The model is 5 m wide and 30 m long and includes 6 groynes and 5 groyne fields. It further includes a part of the main channel at one side and a part of the floodplain at the other side of the groyne fields. Gravel is fixed to the bed to ensure hydraulically rough flow conditions. In the experiment many measurements were done. The first aim of the measurements was to obtain a good spread of points to validate numerical models on. The second aim was to gain insight in the different flow processes in order to describe the differences between groyne and weir flow and quantify the resistance groynes have on a flow.

An important observation was the existence of a region of low flow, at the tip of the groyne. The observation indicates a complex three-dimensional flow which effectively redistributes discharge over the transverse. The contribution of this flow to the two-dimensional momentum balance is then directly as a secondary circulation and indirectly by alternating the distribution of discharge. Complex flow furthermore invalidates the hydrostatic pressure assumption. The observed flow needs further investigation with either more accurate measurement devices or in a 3D non-hydrostatic model. Another observation includes the contraction and expansion of flow over the groyne crest. The expansion of flow over the main body of the groyne seems comparable to the expansion of flow over a weir, which can be predicted as Carnot head losses. The observation of expansion losses is however clouded by other flow processes, such as bed shear stress, the lateral flow around the groyne and possible three-dimensional processes induced by the groyne tip, so that the observed head loss over the groyne is only partially explained by weir-like expansion losses.

The comparability between groyne flow and weir flow does not seem to hold at the groyne tip, where no separation of flow is observed. Measurements were performed 10 cm away from the transition between the groyne tip and main body of the groyne. This means that at full scale there is a region of 3 m on either side of this geometrical transition where the transition lies between weir-like overflow and non-weir-like overflow.

With the here performed simulations it is possible to adapt weir head loss formulas on the observed head losses over groyne. It should be possible to validate a three-dimensional non-hydrostatic model, which can further quantify the effect of three-dimensional flow and differentiate the different contributions to groyne head loss. Based on these models proper tuning parameters can be chosen to represent the complex flow in a two-dimensional model and separately model the weir-like expansion.

## Table of content

Preface.....	v
Summary .....	vi
List of symbols .....	ix
List of abbreviations .....	x
List of figures.....	xi
List of tables .....	xiv
1 Introduction.....	1
1.1 Research objectives .....	3
1.2 Methodology .....	3
1.3 Outline of report .....	3
2 Literature study on groyne modelling.....	4
2.1 Shear stress modelling.....	4
2.1.1 Bed shear .....	4
2.1.2 Reynolds stress .....	5
2.1.3 Differential advection .....	6
2.2 Compound channel flow .....	6
2.3 Emerged groynes.....	8
2.4 Submerged groynes .....	8
2.4.1 Weir flow .....	9
2.4.2 Flow around obstacles.....	13
2.4.3 Interaction with mean flow .....	13
2.4.4 Synthesis of flow processes associated with submerged groynes .....	14
2.4.5 Modelling of submerged groyne resistance .....	16
2.5 Summary .....	19
3 Methodology .....	20
3.1 Model description .....	20
3.2 Measurement techniques .....	22
3.2.1 EMS.....	22
3.2.2 PTV.....	23
3.2.3 Laser altimeters .....	24
3.3 Boundary conditions and measurement locations .....	24
3.3.1 Hydraulic conditions.....	24
3.3.2 Measurement points in a cross section.....	25
3.3.3 Measurement series without groynes .....	25
3.3.4 Measurement series with groynes .....	26
3.3.5 Summary simulations .....	27
3.4 Data processing .....	28

4	Results .....	29
4.1	Visual observation.....	29
4.2	Water level slopes and groyne head loss .....	30
4.3	Water surface flow .....	31
4.4	Flow observations around groyne .....	33
4.5	Flow dynamics away from the groyne .....	35
4.6	Summary .....	36
5	Discussion.....	38
5.1	Weir-like expansion over groyne .....	38
5.2	Three-dimensional flow .....	41
5.3	Lateral flow .....	42
5.4	Total groyne resistance.....	44
5.5	Summary .....	46
6	Conclusions .....	46
7	Recommendations.....	49
	Bibliography.....	51
	Appendix A .....	55
	Appendix B .....	59
	Appendix C .....	63
	Appendix D .....	69
	Appendix E .....	71
	Appendix F .....	74
	Appendix G.....	77
	Appendix H.....	82
	Appendix I.....	87



## List of symbols

$A$	Cross-sectional flow area of a channel	$\text{m}^2$
$B$	Width of a channel	$\text{m}$
$C$	Chézy friction coefficient	$\text{m}^{1/2}/\text{s}$
$C_{effective}$	Effective Chézy friction coefficient in the groynes region	$\text{m}^{1/2}/\text{s}$
$C_{base}$	Base bottom friction Chézy friction coefficient in the groynes region	$\text{m}^{1/2}/\text{s}$
$C_D$	Drag coefficient over groynes	-
$C_Q$	Discharge coefficient in weir formula (24)	-
$C_1$	Modelling parameter in (24)(26)	-
$C_2$	Modelling parameter in (24)(27)	-
$d$	Total water depth; $d = h - z_b$	$\text{m}$
$Fr$	Froude number; $Fr = \frac{u}{\sqrt{gd}}$	-
$g$	Acceleration of gravity	$\text{m}/\text{s}^2$
$H$	Energy head; $H = h + \frac{U^2}{2g}$	$\text{m}$
$h$	Water level height relative to $z_0$	$\text{m}$
$h_g$	Height of the groyne relative to $z_b$	$\text{m}$
$k$	Turbulent kinetic energy	$\text{m}^2/\text{s}^2$
$k_s$	Nikuradse roughness height	$\text{m}$
$L$	Length scale	$\text{m}$
$L_c$	Length of the groyne crest in streamwise direction	$\text{m}$
$m_u$	Upstream groyne slope	-
$m_d$	Downstream groyne slope	-
$n$	Manning bed shear friction factor	$\text{m}^{1/3}/\text{s}$
$P$	Wet perimeter	$\text{m}$
$p$	Water pressure	$\text{N}/\text{m}^2$
$Q$	Total discharge	$\text{m}^3/\text{s}$
$q$	Specific discharge; $q = Q/B$	$\text{m}^2/\text{s}$
$R$	Hydraulic radius; $R = \frac{A}{P}$	$\text{m}$
$S$	Groyne spacing in streamwise direction	$\text{m}$
$t$	Time	$\text{s}$
$U$	Velocity scale	$\text{m}/\text{s}$
$u$	Flow velocity in streamwise direction	$\text{m}/\text{s}$

$u_*$	Bed shear velocity	m/s
$v$	Flow velocity in transverse direction	m/s
$w$	Flow velocity in vertical direction	m/s
$x$	Horizontal coordinate in streamwise direction	m
$y$	Horizontal coordinate in transverse direction	m
$z$	Vertical coordinate	m
$z_b$	Bed level	m
$\alpha$	Coefficient in equation (16); $\alpha = 0.1$	-
$\alpha_{1,2}$	Empirical factors in equation (31); $\alpha_1 = 76.4$ ; $\alpha_2 = 3.7$	-
$\beta$	Empirical factor in equation (17);	-
$\Gamma$	Constant of secondary circulations; $\Gamma = \frac{\partial}{\partial y} d(\rho UV)_d$	N/m <sup>2</sup>
$\delta$	Width of the mixing layer	m
$\epsilon$	Dissipation of turbulent kinetic energy	m <sup>2</sup> /s <sup>3</sup>
$\lambda$	Dimensionless skin friction coefficient	-
$\nu_t$	Turbulent eddy viscosity	m <sup>2</sup> /s
$\rho$	Density of the water	kg/m <sup>3</sup>
$\tau_{ij}$	Shear stress in the direction $i, j$	N/m <sup>2</sup>
$\tau_b$	Bed shear stress	N/m <sup>2</sup>

## List of abbreviations

$mc$	Main channel
$gf$	Groyne field
$fp$	Floodplain
$b$	Bypassing
$gc$	Groyne crest
$up$	0.5 m upstream of groyne crest
$ds$	1 m downstream of groyne crest

## List of figures

FIGURE 1; CONCEPTUAL VIEW OF FLOW OVER SUBMERGED GROUYNE .....	1
FIGURE 2; EXAMPLE OF EFFECT OF SECONDARY CIRCULATIONS OF THE MOMENTUM BALANCE. SOURCE: (SHIONO & KNIGHT, 1991) .....	6
FIGURE 3; HYDRAULIC PARAMETERS ASSOCIATED WITH TWO-STAGE CHANNEL FLOW. SOURCE: (SHIONO & KNIGHT, 1991) .....	7
FIGURE 4; SKETCH OF VORTEX MOVING ON AN UNEVEN BOTTOM. TRANSVERSE VELOCITY INCREASES AT THE FRONT AND DECREASES AT BACK OF THE VORTEX. SOURCE: (PROOIJEN, BATTJES, & UIJTTEWAAL, 2005) .....	7
FIGURE 5; PARAMETERS RELEVANT FOR A SUBMERGED WEIR. FLOW ACCELERATES BETWEEN AREAS 1 AND 2. ENERGY IS LOST IN A LARGE GYRE NEAR THE BOTTOM BETWEEN AREAS 2 AND 3. SOURCE: (SIEBEN, 2011).....	8
FIGURE 6; EXAMPLE OF FLOW DOWNSTREAM OF A BACKWARD FACING STEP. ON TOP ARE SHOWN THE VELOCITY AND REYNOLD STRESS PROFILE. BELOW ARE SHOWN THE TURBULENT ENERGY PROFILES. ALL VALUES WERE NORMALIZED BY THE VELOCITY ON THE STEP. SOURCE: (NAKAGAWA & NEZU, 1986) .....	10
FIGURE 7; HEAD LOSS IN THE GROUYNE FIELD AND MAIN CHANNEL. THE FIGURE VISUALIZES THE ASSUMPTION OF NO SLOPE IN THE GROUYNE FIELD, SUCH THAT THE TOTAL RESISTANCE IS DETERMINED BY THE WEIR LOSSES, WHICH EQUALS THE EFFECT OF BED SHEAR STRESS IN THE MAIN CHANNEL. SOURCE: (KRUIJT, 2013).....	11
FIGURE 8; COMPOUND WEIR MODEL, SCHEMATIZATION AS SEPARATE INDEPENDENT WEIRS. SOURCE: (JANSEN, 2020).....	11
FIGURE 9; CONTROL VOLUME WITH THE INCLUSION OF LATERAL ADVECTION IN THE BALANCE OF MOMENTUM. SOURCE: (JANSEN, 2020) .....	12
FIGURE 10; SCHEMATIZATION OF VON KARMAN VORTICES AROUND OBSTACLE. SOURCE: (PRANDTL & TIETJENS, 2003) .....	12
FIGURE 11; VISUALIZATION OF FLOW OVER CUBES, WITH A VERTICAL SPIRALING FLOW DOWNSTREAM OF THE CUBES. SOURCE (GAO, AGARWAL, & KATZ, 2021) .....	12
FIGURE 12; FLOW CIRCULATION DOWNSTREAM OF GROUYNE TIP IN A: $x - y$ (HORIZONTAL) PLANE; B: $y - z$ (VERTICAL) PLANE .....	12
FIGURE 13; VISUALIZATION OF PHYSICAL FLOW PROCESSES IN A CHANNEL WITH GROYNES. 1: FLOW CONTRACTION AND EXPANSION OVER GROUYNE CREST; 2: VERTICAL SEPARATION CELL DOWNSTREAM OF GROUYNE CREST; 3: LATERAL FLOW AT GROUYNE TIP AS A COMPOUND WEIR FLOW; 4: VERTICAL SPIRAL FLOW AROUND AN OBSTACLE; 5: VORTEX SHEDDING FROM GROUYNE TIP; 6: MOMENTUM EXCHANGE IN HORIZONTAL MIXING LAYER; 7: LOGARITHMIC FLOW PROFILE DETERMINED BY BED SHEAR STRESS; 8: SECONDARY FLOWS ASSOCIATED WITH COMPOUND CHANNEL FLOW .....	14
FIGURE 14; AUTOCORRELATION FUNCTIONS IN FLUME WITH SUBMERGED GROYNES. LARGE CONSISTENT FLUCTUATIONS IN THE TIME SIGNAL WERE OBSERVED. SOURCE: (YOSSEF, 2005) .....	15
FIGURE 15; CHARACTERISTICS OF PROTOTYPE GEOMETRY BASED ON THE WAAL RIVER.....	21
FIGURE 16; CROSS-SECTIONAL PROFILE OF THE BED LEVEL IN THE MODEL, WITH FROM LEFT TO RIGHT: FLOODPLAINS GROUYNE FIELD BED LEVEL, MAIN CHANNEL. GROUYNE CONTOUR IS IN YELLOW. SCALE IS 1:30 .....	21
FIGURE 17; SIDE VIEW GROUYNE .....	21
FIGURE 18; TOP VIEW GROUYNE .....	22
FIGURE 19; SKETCH OF EXPERIMENT. IN LIGHT GREY THE RECIRCULATING WATER PIPE. IN DARK GREY THE IN- AND OUTFLOW FROM THE RESERVOIR. A WAVE DAMPER IS INSTALLED AT THE INFLOW OF THE EXPERIMENT. ....	22
FIGURE 20; MEASURED WATER LEVEL ON STILL WATER OVER THE FLUME; DIFFERENT MEASUREMENT POINTS AT ONE LOCATION CORRESPOND TO DIFFERENT LOCATIONS IN THE TRANSVERSE. THE UPPER PLOT THE MEASURED WATER LEVEL; THE MIDDLE PLOT THE SAME MEASUREMENTS MINUS THE MEAN WATER LEVEL MEASURED IN EACH STREAMWISE COORDINATE; THE LOWER PLOT THE MEASURED WATER LEVEL MINUS THE MEAN WATER LEVEL IN EACH DEVICE.....	23
FIGURE 21; CROSS SECTION OF FLUME WITH THE CONSIDERED WATER DEPTHS.....	25
FIGURE 22; LOCATION THE MEASUREMENT POINTS OF THE CROSS SECTIONS FOR THE SIMULATIONS WITHOUT GROYNES WITH WATER DEPTHS OF 30, 35 AND 40 CM. THE AXES ARE IN [M].....	26

FIGURE 23; LOCATION THE MEASUREMENT POINTS OF THE CROSS SECTIONS FOR THE SIMULATIONS WITH GROYNES WITH WATER DEPTHS OF 30, 35 AND 40 CM. THE AXES ARE IN [M]. IN BLUE THE AREA MEASURED WITH THE PTV.....	26
FIGURE 24; SKETCH OF VORTEX SHEDDING FROM THE GROUYNE TIP.....	29
FIGURE 25; SKETCH OF SPREAD OF DYE IN THE WATER INJECTED JUST BEHIND THE GROUYNE CREST .....	29
FIGURE 26; MEASURED WATER LEVELS FOR THE CASES G01 – G03 .....	30
FIGURE 27; MEASURED HEAD LOSS OVER THE GROUYNE FROM 0.5 M UPSTREAM TO 1 M DOWNSTREAM OF GROUYNE CREST .....	30
FIGURE 28; SURFACE VELOCITY AND TURBULENCE MAP FOR CASES G01 – G03. THE AREA CAPTURED BY THE PTV IS FROM $x = 12$ TO $x = 25$ M. THE DASHED LINES INDICATE THE GROYNES AND THE DIFFERENT PARTS OF THE CHANNEL. ....	32
FIGURE 29; DEVELOPMENT OF FLOW VELOCITIES AND TURBULENT FLUCTUATIONS RELATIVE TO THE AVERAGE FLOW VELOCITY ( $Q/A$ ) FOR CASE G01 – G03. THE TRANSVERSE LOCATION IS FROM TOP TO BOTTOM THE MAIN CHANNEL TO THE FLOODPLAIN. ....	34
FIGURE 30; RATIO OF DISCHARGE ON TOP OF THE GROUYNE CREST TO A: THE UPSTREAM DISCHARGE; B: THE DOWNSTREAM DISCHARGE.....	34
FIGURE 31; DEPTH AVERAGE FLOW VELOCITY AT $x = 25$ M FOR CASES G01 – G03 AND E01 – E03.....	35
FIGURE 32; VARIATION OF MEAN FLOW VELOCITY AT $x = 25$ M FOR CASES G01 – G03.....	36
FIGURE 33; RELATIVE TURBULENCE AT $x = 25$ M FOR CASES G01 – G03 .....	36
FIGURE 34; AUTOCORRELATION OF TRANSVERSE VELOCITY SIGNALS AT $x = 23.5$ M FOR THE CASES G01 - G03 AT DIFFERENT PLACES OVER ONE TRANSECT .....	36
FIGURE 35; VISUALIZATION OF WEIR-LIKE EXPANSION OVER GROYNES. THE DASHED LINE IS MEANS A PERFECT AGREEMENT. A: THE MOMENTUM DOWNSTREAM OF THE GROYNES AGAINST THE MOMENTUM ON TOP OF THE GROYNES; B: THE MEASURED CARNOT LOSSES OVER THE GROYNES AGAINST THE MEASURED HEAD LOSS OVER THE GROUYNE; C: EMPIRICAL WEIR COEFFICIENTS OVER THE TRANSVERSE FOR THE DIFFERENT SIMULATIONS; D: EMPIRICAL WEIR COEFFICIENTS AGAINST THE SUBMERGENCE OF THE GROYNES .....	39
FIGURE 36; MEASURED HEAD LOSS FROM 0.5 M UPSTREAM OF GROUYNE TO 1 M DOWNSTREAM OF GROUYNE, COMPARED TO THE MEASURED CARNOT LOSSES AND THE PREDICTED HEAD LOSS USING VIL, YOS AND BRO .....	40
FIGURE 37; MEASURED HEAD LOSS FROM 0.5 M UPSTREAM OF GROUYNE TO 1 M DOWNSTREAM OF GROUYNE, COMPARED TO THE MEASURED CARNOT LOSSES AND THE PREDICTED HEAD LOSS USING VIL, YOS AND BRO INCLUDING THE HEAD LOSS DUE TO BEAD SHEAR STRESS.....	40
FIGURE 38; SENSITIVITY ANALYSIS OF LATERAL FLOW MODEL. THE TOP FIGURES SHOW THE SENSITIVITY OF THE MODEL TO CHANGES IN THE AMOUNT OF BYPASSING RELATIVE THE DISCHARGE IN THE GROUYNE FIELD. THE BOTTOM FIGURES SHOW THE SENSITIVITY OF THE MODEL TO THE WIDTH OF THE MAIN CHANNEL. THE BOUNDARY CONDITIONS ARE TAKEN FROM SIMULATION G03 AND ARE SHOWED AS THE DASHED LINES. THE SETUP OF THE COMPOUND CHANNEL MODEL AND CORRESPONDING BED SHEAR STRESS IS SHOWED IN APPENDIX G. THE GROUYNE HEAD LOSS ARE THE MEASURED CARNOT LOSSES.....	43
FIGURE 39; EFFECT OF INCLUDING BED SHEAR STRESS OVER A DISTANCE OF 1.5 M FROM 0.5 M UPSTREAM OF ONE GROUYNE TO 1 M DOWNSTREAM. A: WITHOUT BED SHEAR STRESS; B: WITH BED SHEAR STRESS .....	43
FIGURE 40; OVERVIEW OF ANALYTICAL COMPOUND CHANNEL MODEL, NOT TO SCALE. THE DEPTH OF THE GROUYNE FIELD IS THE AVERAGE DEPTH IN THE GROUYNE FIELD. THE GROUYNE CREST IS AT 0.2 M ABOVE REFERENCE, SO THAT $h_g = 0.062$ m. SIMPLIFICATION OF THE ANALYTICAL MODEL INCLUDES NEGLECTING THE BED SLOPE IN THE GROUYNE FIELD, NEGLECTING THE GRADUAL TRANSITION BETWEEN CHANNEL COMPOUNDS AND NEGLECTING THE GROUYNE TIP. ....	45
FIGURE 41; COMPARISON OF NUMERICALLY MODELLED WATER LEVELS AND PHYSICALLY OBSERVED WATER LEVELS. ALL WATER LEVELS AT THE DOWNSTREAM BOUNDARY EQUAL EACH OTHER FOR SAKE OF COMPARISON. ....	46
FIGURE 42; LOCATION OF CONTROL VOLUME FOR INCLUSION OF BYPASSING AS LATERAL ADVECTION.....	55
FIGURE 43; CONTROL VOLUME FROM THE GROUYNE CRESH TO DOWNSTREAM SHOWING A FLUX INTO THE BALANCE AREA OF SIZE $\Delta y, \Delta x$ .....	55
FIGURE 44; MEASUREMENT POINT IN ONE CROSS SECTION FOR THE SIMULATIONS WITH WATER DEPTH $D = 40$ CM. THE AXES ARE IN [M] .....	59

FIGURE 45; MEASUREMENT POINT IN ONE CROSS SECTION FOR THE SIMULATIONS WITH WATER DEPTH $D = 35$ CM. THE AXES ARE IN [M] .....	59
FIGURE 46; MEASUREMENT POINT IN ONE CROSS SECTION FOR THE SIMULATIONS WITH WATER DEPTH $D = 30$ CM. THE AXES ARE IN [M] .....	59
FIGURE 47; MEASUREMENT POINT IN ONE CROSS SECTION FOR THE SIMULATIONS WITH WATER DEPTH $D = 24$ CM. THE AXES ARE IN [M] .....	60
FIGURE 48; MEASUREMENT POINT IN ONE CROSS SECTION FOR THE SIMULATIONS WITH WATER DEPTH $D = 18$ CM. THE AXES ARE IN [M] .....	60
FIGURE 49; MEASUREMENT POINT ON TOP OF ONE GROUYNE FOR THE SIMULATIONS WITH A WATER DEPTH OF $D = 40$ CM. THE AXES ARE IN [M] .....	60
FIGURE 50; LOCATION THE MEASUREMENT POINTS OF THE CROSS SECTIONS FOR THE SIMULATIONS WITHOUT GROYNES WITH WATER DEPTHS OF 30, 35 AND 40 CM. THE AXES ARE IN [M]. IN BLUE THE AREA MEASURED WITH THE PTV .....	61
FIGURE 51; LOCATION THE MEASUREMENT POINTS OF THE CROSS SECTIONS FOR THE SIMULATIONS WITHOUT GROYNES WITH A WATER DEPTH OF 24 CM. THE AXES ARE IN [M]. IN BLUE THE AREA MEASURED WITH THE PTV .....	61
FIGURE 52; LOCATION THE MEASUREMENT POINTS OF THE CROSS SECTIONS FOR THE SIMULATIONS WITHOUT GROYNES WITH A WATER DEPTH OF 18 CM. THE AXES ARE IN [M]. IN BLUE THE AREA MEASURED WITH THE PTV .....	61
FIGURE 53; LOCATION THE MEASUREMENT POINTS OF THE CROSS SECTIONS FOR THE SIMULATIONS WITH GROYNES WITH WATER DEPTHS OF 30, 35 AND 40 CM. THE AXES ARE IN [M]. IN BLUE THE AREA MEASURED WITH THE PTV .....	62
FIGURE 54; VERTICAL VELOCITY PROFILES FROM $x = 20.5$ M TO $x = 25$ M. FROM JUST UPSTREAM OF THE FOURTH GROUYNE TO FAR DOWNSTREAM. THE BED LEVEL IS SHOWN IN AS A BLACK LINE. THE GROUYNE HEIGHT IS SHOWN AS A BLACK DOTTED LINE. ....	65
FIGURE 55; RELATIVE FLUCTUATION FROM $x = 20.5$ M TO $x = 25$ M. FROM JUST UPSTREAM OF THE FOURTH GROUYNE TO FAR DOWNSTREAM. THE BED LEVEL IS SHOWN IN AS A BLACK LINE. THE GROUYNE HEIGHT IS SHOWN AS A BLACK DOTTED LINE. THE FLUCTUATIONS ARE NORMALIZED ON THE DEPTH AVERAGE FLOW VELOCITY AT $x = 21$ M, THE LOCATION OF THE GROUYNE. ....	68
FIGURE 56; DISCHARGE REGULATION BY BLOCKADING PART OF THE INFLOW .....	69
FIGURE 57; DEVELOPMENT OF THE MEAN FLOW VELOCITY IN THE MAIN CHANNEL, GROUYNE FIELD AND FLOODPLAIN FOR ALL CASES. CASES E01 – E03 IN FIGURE A; E04 – E06 IN FIGURE B; E07 – E09 IN FIGURE C; E10 – E12 IN FIGURE D; E13 IN FIGURE E; G01 – G03 IN FIGURE F .....	70
FIGURE 58; MEASURED WATER LEVEL SLOPES FOR CASES E01-E13 WITHOUT GROYNES .....	75
FIGURE 59; DEPTH AVERAGE VELOCITY FOR THE CASES E01 – E09. COLORS CORRESPOND TO SIMILAR FROUDE NUMBERS IN THE SIMULATION. LINE STYLES CORRESPOND TO DIFFERENT WATER LEVELS. ....	76
FIGURE 60; DEPTH AVERAGE VELOCITY FOR THE CASES E10 – E13 .....	76
FIGURE 61; RELATIVE TURBULENCE FOR THE CASES E01 – E13 .....	76
FIGURE 62; AUTOCORRELATION FUNCTION OF TRANSVERSE VELOCITY COMPONENT AT $x = 21$ M FOR DIFFERENT PLACES IN THE TRANSVERSE FOR CASE E01 – E03 .....	76
FIGURE 63; OVERVIEW OF ANALYTICAL COMPOUND CHANNEL MODEL, NOT TO SCALE. THE DEPTH OF THE GROUYNE FIELD IS THE AVERAGE DEPTH IN THE GROUYNE FIELD. THE GROUYNE CREST IS AT 0.2 M ABOVE REFERENCE, SO THAT $h_g = 0.062$ m. SIMPLIFICATION OF THE ANALYTICAL MODEL INCLUDES NEGLECTING THE BED SLOPE IN THE GROUYNE FIELD, NEGLECTING THE GRADUAL TRANSITION BETWEEN CHANNEL COMPOUNDS AND NEGLECTING THE GROUYNE TIP. ....	77
FIGURE 64; MODELLED WATER LEVEL SLOPES USING $k_s = 0.068 \pm 0.031$ m. ....	79
FIGURE 65; MODELLED WATER LEVEL USING $k_s = 0.032 \pm 0.015$ m. ....	79
FIGURE 66; MODELLED DISCHARGE DISTRIBUTION IN THE COMPOUND CHANNEL USING $k_s = 0.032 \pm 0.015$ m. ....	80
FIGURE 67; MODELLED WATER LEVEL SLOPES IN THE COMPOUND CHANNEL USING $k_s = 0.042 \pm 0.002$ m IN THE MAIN CHANNEL AND FLOODPLAIN AND $k_s = 0.012 \pm 0.002$ m IN THE GROUYNE FIELD. ....	80
FIGURE 68 MODELLED DISCHARGE DISTRIBUTIONS IN THE COMPOUND CHANNEL USING $k_s = 0.042 \pm 0.002$ m IN THE MAIN CHANNEL AND FLOODPLAIN AND $k_s = 0.012 \pm 0.002$ m IN THE GROUYNE FIELD. ....	81
FIGURE 69; RESULTS OF FITTING THE LAW OF THE WALL TO EACH VERTICAL STREAMWISE FLOW PROFILE .....	83

FIGURE 70; PLOTS OF OBTAINED BED FRICTION FACTORS OVER THE WATER DEPTH AND MEAN FLOW VELOCITY. FROM TOP TO BOTTOM: SHEAR VELOCITY $u^*$ , Nikuradse roughness height $k_s$ , CHEZY SMOOTHNESS COEFFICIENT $C$ AND MANNING'S ROUGHNESS COEFFICIENT $n$ . DIFFERENT COLORS AND MARKER STYLE INDICATE DIFFERENT EXPERIMENTS. THE MEAN VALUE AND BOUNDS OF ONE STANDARD DEVIATION ARE SHOWN ALSO FOR THE $k_s$ , $C$ AND $n$ .	84
FIGURE 71; COMPARISON OF CALCULATED BED SHEAR STRESS USING EMPIRICAL FORMULATIONS OVER THE BED SHEAR STRESS AS DEFINED BY THE SHEAR VELOCITY OBTAINED FROM FITTING THE LAW OF THE WALL. THE LIMITS OF THE UNCERTAINTY BOUNDS ARE THE CALCULATED BED SHEAR STRESS USING THE ONE STANDARD DEVIATION OF THE DERIVED VARIABLES $C$ , $n$ AND $k_s$ .	85
FIGURE 72; PICTURE OF PHYSICAL MODEL TAKEN FROM THE DOWNSTREAM END.	87
FIGURE 73; INFLOW REGION WITH THE BLUE FLOW STRAIGHTENERS, AND WHITE WAVE DAMPERS	87
FIGURE 74; INFLOW REGION TAKEN FROM THE FLOW STRAIGHTENERS. ON THE RIGHT THE INFLOW FROM THE PUMP. THE INFLOW IS DIVIDED INTO TWO PARTS: BEHIND A TURBULENT REGION WHERE THE WATER FLOWS IN, WHICH OVERFLOWS INTO THE REGION HERE THE FLOW ENTERS THE PHYSICAL MODEL.	88
FIGURE 75; DOWNSTREAM BOUNDARY, DIVIDED FROM THE PHYSICAL MODEL BY NETTING TO PREVENT PTV TRACKING PARTICLES FROM ENTERING THE RESERVOIR OR THE PUMP.	88
FIGURE 76; BEHIND THE NETTING IS THE OUTFLOW. ON THE LEFT THE PUMP WHICH IS THE MAIN OUTFLOW AND DETERMINED THE AMOUNT OF DISCHARGE THROUGH THE FLUME. RIGHT OF IT IS THE INFLOW FROM THE WATER RESERVOIR, WHICH IS USED TO FILL THE PHYSICAL MODEL AND IS USED TO COMPENSATE WATER LEAKAGE IN THE EXPERIMENT. LEFT IS THE OVERFLOW WEIR TO THE RESERVOIR, WHICH KEEPS THE WATER LEVEL COSTANT.	89
FIGURE 77; THE SIDE WALL AT THE MAIN CHANNEL SIDE IS CONCRETE FOR THE LARGEST PART AND A PART GLASS	89
FIGURE 78; THE SIDE WALL AT THE FLOODPLAIN SIDE ARE WOODEN PLANKS.	90
FIGURE 79; THE MEASUREMENTS CARRIAGE, WITH 6 EMS INSTALLED AND 3 LASER ALTIMETERS INSTALLED.	90
FIGURE 80; THE EMS ON THE RIGHT, THE LASER ALTIMETER ON THE LEFT. THE ALTIMETER MEASURES A THE DISTANCE BETWEEN A SET REFERENCE TO A PAPER FLOATING OF THE SURFACE OF THE WATER.	91
FIGURE 81; GRAVEL BED OF THE EXPERIMENT WITH APPROXIMATELY 5500 STONES PER SQUARE METER	91
FIGURE 82; PICTURE OF GROUYNE IN THE MODEL	91

## List of tables

TABLE 1; DISCHARGES CONSIDERED FOR EACH WATER LEVEL	25
TABLE 2; SUMMARY OF EVERY SIMULATION	27
TABLE 3; INTEGRATION OF DISCHARGE FROM $y = 2.3\text{ m}$ TO $y = 3.9\text{ m}$ UPSTREAM (UP) OF THE GROUYNE, ON THE GROUYNE CREST (G) AND DOWNSTREAM (DS) OF THE GROUYNE	35
TABLE 4; MAGNITUDE OF DIFFERENT PHYSICAL PROCESSES DIVIDED BY THE PRESSURE GRADIENT OF THE FLOW	45

# 1 Introduction

Groynes are a common sight in Dutch rivers. Groynes are structures that stretch from the bank perpendicular into the channel, as shown in Figure 1. Under normal flow conditions these groynes emerge. In these conditions the groynes push the flow away from the bank into the main channel. This decreases the conveyance flow area of the total channel and therefore increases the flow velocity in the main channel.

One effect is that there is almost no flow at the bank, reducing bank erosion, such that no other revetment has to be designed for the protection of the bank. Furthermore, the increased flow velocity in the main channel inhibits the formation of ice jams, which was a common problem in the past, and might still be a problem in rare extreme winters. The increased flow velocity in the main channel goes together with an increased water depth in the main channel, which is beneficial for the navigability of the rivers, even under low-flow conditions. Groynes also fixate the river course, stopping the meandering behaviour of rivers, at the locations where the groynes are constructed. For these reasons groynes have been constructed along long stretches of the Dutch rivers.

The behaviour of flow over groynes changes however when the groynes become submerged. This happens for high water conditions. Now the groyne regions start contributing to the conveyance capacity of the channel. The groynes become submerged obstacles, and increase the flow resistance compared to the situation without groynes. A quantification of 'how much' the groynes add to the river resistance for different submergence levels, has not properly been established to this day.

Over the last couple of decades the Dutch river system was updated to withstand higher peak flows without breaching of the dikes. Based on the idea of *Room for Rivers* the rivers gained more space to convey excess water, in for example side channels and wider floodplains. This in contrast with simply increasing the crest levels of the dikes. Over this period *Rijkswaterstaat* has considered the lowering or streamlining (reduction of the downstream groyne slope) of groynes, to reduce the groyne resistance under submerged conditions. A number of pilot projects have even been realized (e.g. in the Waal between the cities of Beuningen and Gorinchem), to investigate the (long-term) effect on the flow and morphodynamics in the river.

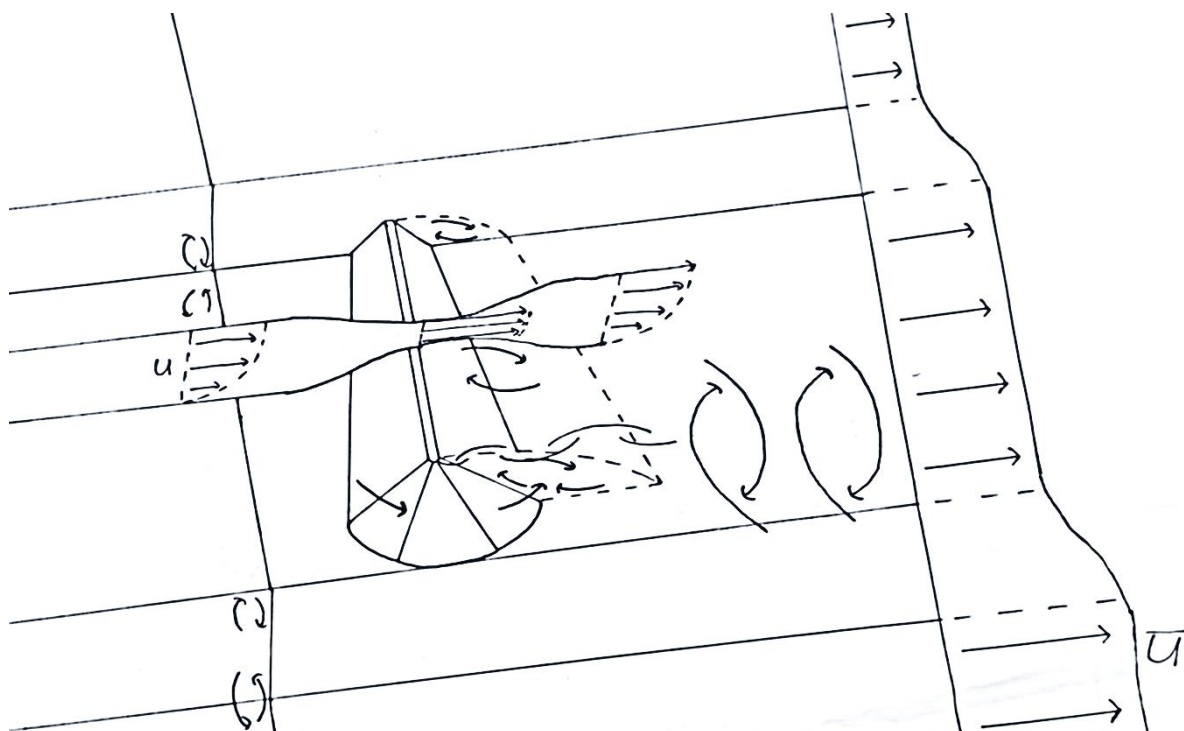


Figure 1; Conceptual view of flow over submerged groyne

A special case is the planned lowering of groynes in the Pannerdensch Kanaal. The groyne lowering, together with the lowering of some banks, should contribute to 5 cm of reduced water levels under high water conditions. Construction work on the project will start soon, and the project should be finished in 2023.

It is interesting to note that this groyne lowering is modelled in WAQUA, as prescribed by Dutch laws. Here the groynes are modelled as weirs. The flow resistance of weirs can either be determined by the *Tabellenboek* method, which quantifies weir resistance based on the hydraulic conditions of the flow and the dimensions of the weir, or the *Villemonte* weir formula. The first method is based on laboratory experiments, on the basis of which weir resistance was quantified in tables so that all existent cases of weir flow in the Dutch rivers could be examined (Blumenthal & Ubels, 1961). The weir flow was used for the overflowing of the summer dikes and the inundation of the floodplains in the winter. This method is therefore calibrated on the Dutch rivers. Lately weirs can also be modelled using an empirical expression of head loss over a weir, the *Villemonte* approach (Sieben, 2011). The calibration factors in this formula are such that it complies with the *Tabellenboek* method. Both methods determine weir head losses as a subgrid process, as weirs (and groynes) are generally small compared to the grid size of the numerical models, so that only the head loss based on the theoretical groyne can be included in a model, and not the bed topography of the weir itself.

Groynes do not equal weirs however. For weir flow the head loss is determined by the flow contraction upstream of the weir and flow expansion downstream of the weir. Water contracts and expands over groynes, but is also influenced by lateral shear. In the groyne field there is generally a gradient in transverse bed slope from the deeper main channel to the bank. This leads to a gradient in the streamwise velocities from the bank to the main channel, with large flow velocities in the main channel. The effect is that the flow over groynes is convected by the lateral velocity gradients. Ambagts (2019) observed that for a higher submergence level more water would flow over the tip of the groyne, with a large effect of lateral advection and diffusion at the groyne tip. Yossef (2005) furthermore observed lower water level slopes than expected from weir modelling. To accommodate the difference between groynes and weirs WAQUA has used-defined reduction factors. For the modelling of this groyne lowering Zagonjoli (2017) assessed the effect of the different reduction coefficients. The modelled difference in water levels varied between -1 and +10 cm of water level due to the groyne lowering and the authors suggested recalibration of the numerical models on data from physical modelling.

To assess their shortcomings the 2D subgrid methods were compared to 3D (non-hydrostatic) simulations (Zagonjoli, Platzek, & Kester, 2017) (Yossef, 2017). This comparison showed a disagreement between 2D and 3D modelling, and indicated an overestimation of the effect of groyne lowering or streamlining. The used 3D model was not validated however for the flow over weir-like structures, and currently there is not enough experimental data to do such validation (Omer & Yossef, 2017).

To fill the knowledge gap, *Rijkswaterstaat* and the *Delft University of Technology* have decided to set up a physical laboratory experiment at *Delft University of Technology*, for studying the flow over submerged groynes. Based on preliminary 3D numerical simulation executed by *Deltares* (Chavarrías, Platzek, & Yossef, 2019) and based on scaling concerns addressed by Uijttewaai (2019) a scale model based on prototype conditions in the Waal river (Figure 15) has been constructed. The project started with the desire to model groyne lowering. To obtain this goal however first the background has to be known without groynes and with the standard groynes. This is where this thesis focusses on as one of the first to study with a physical model.

In this state the questions to answer are what the flow resistance is of submerged groynes compared to a situation without groynes, what physical processes are responsible for the head loss, and whether these processes can be incorporated in a weir head loss formula. This leads to the research objectives formulated in the next section.



## 1.1 Research objectives

- To quantify the resistance that highly submerged groynes add to a flow section.
- To describe the comparability between flow over highly submerged groynes and flow over weirs.
- To test the applicability of weir head loss formulas to describe head loss over highly submerged groynes.
- To obtain quantitative data on the mean velocity and water levels that enables the subgrid modelling of highly submerged groynes.

To reach our objectives the following questions are formulated:

- To what extent does a groyne behave like a weir?
  - o What are the dominant physical flow processes in a flow cross section with a series of groynes?
  - o Where does the energy dissipate in a flow section with a series of groynes?
- What is the total effect that groynes have on the resistance of a flow cross section?
  - o Can this resistance be predicted by weir expansion losses?

## 1.2 Methodology

To gain insight in the current state of knowledge first literature is studied which focusses on the physical processes associated to groyne and weir flow, which includes flow in a compound channel. Lastly the literature study focusses on current efforts to model groynes and whether any adaptations to these models would improve groyne modelling.

The next step is to do the physical modelling without groynes and with submerged groynes. From the results from physical modelling it is possible to describe the flow processes associated with submerged groyne flow and obtain quantitative data on the mean velocity and water levels that enables the subgrid modelling of highly submerged groynes.

Lastly it is attempted to recreate the flow in a one-dimensional model as a compound channel to gain insight in where the resistance comes from. With the comparison of the analytical model to the physical model it is possible to assess whether the groyne resistance can be predicted as a weir loss.

## 1.3 Outline of report

The report is constructed in line with a more American style of reporting, with strictly defined chapters of methodology, results, discussion and conclusions. The results are short and show only insights directly based on the experiments as described in the methodology. Only in the discussion the results are more extensively interpreted and compared with other researches.

The literature study is in Chapter 2, and explores the physical processes that can be expected in the flume in general, and how to incorporate those in a schematized way in the momentum balance. The last part explores the physical processes related to groyne flow and how to incorporate those in the momentum balance.

Chapter 3 explains the setup of the physical model, starting with a description of the model and elaborating on the measurement techniques. Then an explanation follows on the choice of measured hydraulic conditions and measurement points. Lastly the way of processing the measurement data to time and special average values is explained.

Chapter 4 shows the results from physical modelling. The chapter starts with a description of elements that could not be measured but did have an impact on the physical modelling. It then elaborates on the measured water elevations. The last part shows the observed flow in the simulations with groynes.

Chapter 5 discusses the results. First the comparability of flow expansion over groynes and weirs is discussed. Then the three-dimensional character of the flow is discussed. Next the influence of lateral exchange is discussed. Lastly the overall resistance groynes add to a channel is discussed.

Chapter 6 concludes on the findings in chapters 4 and 5 and answers the research questions. Chapter 7 gives recommendations for follow-up studies based on the work in this research.

## 2 Literature study on groyne modelling

The starting point for the analysis done in this thesis are the steady state 2DH Reynolds averaged Navies-Stokes equations.

$$\frac{\partial dU}{\partial x} + \frac{\partial dV}{\partial y} = 0 \quad (1)$$

$$\rho dU \frac{\partial U}{\partial x} + \rho dV \frac{\partial U}{\partial y} + \rho dg \frac{\partial h}{\partial x} + \tau_b - \frac{\partial dT_{xy}}{\partial y} = 0 \quad (2)$$

$$\rho dV \frac{\partial V}{\partial y} + \rho dU \frac{\partial V}{\partial x} + \rho dg \frac{\partial h}{\partial y} + \tau_b - \frac{\partial dT_{yx}}{\partial x} = 0 \quad (3)$$

With equation (1) the continuity equation and equations (2) and (3) the momentum balance for the streamwise and transverse flow direction. With the capitals indicating depth averaged values, and with:  $h$  the surface elevation in [m], measured relative to the groyne crest height;  $d$  the water depth in [m];  $u$  and  $v$  the streamwise and transverse ( $x, y$ ) flow velocity in [m/s];  $\tau_b$  the bottom shear stress in [N/m<sup>2</sup>] and  $\tau_{xy}$  the remaining stresses in their respective direction in [N/m<sup>2</sup>]. The normal stresses have been neglected.

The terms in equation (1), the continuity equation, are, from left to right: the change of specific discharge in streamwise and transverse direction.

The terms in equation (2) and (3) are, from left to right: the advective acceleration in normal and tangential direction; the water pressure gradient, the bottom boundary roughness and the remaining shear stresses. The transverse shear stresses then consist of the Reynolds shear stresses and the differential advection when neglecting viscosity:

$$\frac{T_{xy}}{\rho} = -\overline{u'v'} - UV \quad (4)$$

The remainder of the literature study will focus on the different specific aspects of river flow and will link different phenomena to different parts of the depth averaged, Reynolds averaged Navies-Stokes equations.

### 2.1 Shear stress modelling

Generally the velocities and elevations are measured in the flume. That leaves the need to find closures for the bed shear stress, the Reynolds stresses and the differential advection. Assumptions for these closures are presented now.

#### 2.1.1 Bed shear

At the bed of the flume there is a friction between the water and the wall. The bed friction is included in the momentum balance, where it appeared as the boundary condition required for the depth integration of shear stress.

To start defining the bed shear stress one can see from dimensional analysis that bed friction has to scale with the mean velocity squared and the density (Strurn, 2001). In general the bed friction  $\tau_b$  is then defined as:

$$\tau_b = \rho U_*^2 \quad (5)$$

The  $U_*$  is the so called shear velocity at a certain reference frame above the bed. The friction velocity is related to the depth averaged velocity. Therefore a friction factor is included:

$$\lambda = \left(\frac{U_*}{U}\right)^2 \quad (6)$$

The friction factor is experimentally determined, based on the determination of the so called friction velocity  $U_*$ , the velocity one would obtain when extrapolating the velocity profile to the bed.

Attempts to determine the friction factor commonly assumed a simplified 1D momentum balance, a simple balance between bed slope and water level slope. Good examples that are still used are respectively Manning and Chezy:

$$U = \frac{1}{n} R^{2/3} \sqrt{S} \quad (7)$$

$$U = C \sqrt{RS} \quad (8)$$

With  $R$  the hydraulic radius and  $S$  the surface slope. The bed shear stress then becomes respectively:

$$\tau_{b,Manning} = \frac{n^2 g}{\sqrt[3]{d}} \rho U^2 \quad (9)$$

$$\tau_{b,Chezy} = \frac{g}{C^2} \rho U^2 \quad (10)$$

For a water level of 40 cm Besseling (2021) determined the Manning's  $n$  to be 0.0245 in the main channel. Based on the Prandtl mixing length theory Von Karman obtained that the flow profile is logarithmic near the wall (Karman, 1930). Clauser (1954) found that boundary flow close to the wall can be described by a universal Law of the Wall:

$$\frac{u}{u_*} = \frac{1}{\kappa} \ln \frac{z}{z_0} \quad (11)$$

Based on this logarithmic property Colebrook and White (1937) developed an engineering formula using the roughness height of the bed  $k_s$  as determined by Nikuradse (1950):

$$C = 18 \log \frac{12 R}{k_s} \quad (12)$$

Finding the magnitude of the bed shear stress now becomes finding a property of the bed rather than the flow. The roughness height should be comparable with the size of the gravel which is glued to the bed of the experiment, which is well sorted gravel with a  $D_{50} = 8$  mm.

### 2.1.2 Reynolds stress

In general it is expensive and laborious to measure the velocity fluctuations in a river one wants to model. Therefore to model the Reynolds stresses one can adopt the eddy viscosity concept or Boussinesq approach:

$$-\overline{u'_i u'_j} = \nu_t \left( \frac{\partial U_i}{\partial x_j} + \frac{\partial U_j}{\partial x_i} \right) \quad (13)$$

With  $\nu_t$  the eddy viscosity, characterized as a length scale times a velocity scale (LU). The most basic source of turbulence is the bottom friction. But there might be more sources of turbulence, such as free shear between two layers of different flow velocities. As those sources of turbulence have different origins, there are different associated length scales and velocity scales for the calculation of the eddy viscosity. With that there are different models for the parameterization of the turbulent eddy viscosity.

### 2.1.3 Differential advection

The differential advection is due to secondary circulations. When there are secondary circulations  $UV \neq 0$  while  $V = 0$ , such as shown in Figure 2.

There are secondary circulations in any flow with lateral bottom elevation changes, a compound channel (Shiono & Knight, 1991). Shiono and Knight were not able to measure the magnitude of the differential advection but were able to deduce it calculating the remaining terms in the momentum balance. They found that:

$$\frac{\partial}{\partial y} d(\rho UV)_a = \Gamma \quad (14)$$

This constant  $\Gamma$  has to be determined for each specific geometry, which poses a major challenge. For our study the available equipment is not suited for the determination of all terms in the momentum equation to determine  $\Gamma$ . The factors of  $\Gamma$  can however be fitted on for each channel compound when a proper value of the bed roughness is chosen, in case secondary circulations are deemed important. This could very well be the case after having measured the flow in the flume. A sign that secondary circulations impact the flow is a deviating pattern than expected from the balance of the water level slope and the bed friction. This balance says that the flow velocity solely depends on the water depth, given the bed roughness and the discharge.

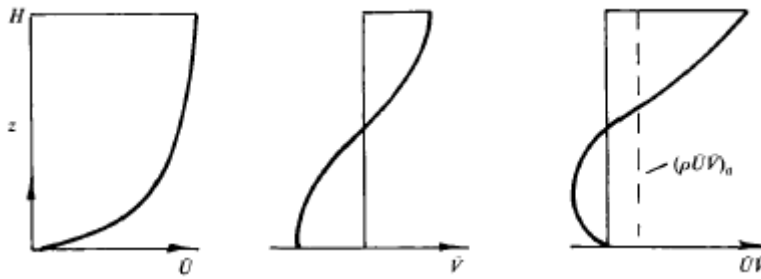


Figure 2; example of effect of secondary circulations of the momentum balance. Source: (Shiono & Knight, 1991)

## 2.2 Compound channel flow

The hydraulic processes playing a part in flow in compound channel are shown in Figure 3. In general the flow in the floodplain can be characterized by a low flow region with a logarithmic flow profile (Yang, Cao, & Knight, 2007). This also holds true for our case with a main channel, groyne field and floodplain. Where the depth average velocity decreases from the main channel to the floodplain.

A free shear layer exists between the areas of different flow velocities. The presence of this mixing layer imposes a reduction of the discharge capacity compared to the situation in which the channel and the floodplain are considered as separate channels without mixing layer (Rice, 1974). This is called the 'kinematic effect' (Zheleznyakov, 1950). In the mixing layer there is mass and momentum exchange (Proust, Bousmar, Paquier, & Zech, 2010). The momentum exchange in the mixing layer is caused by vortical structures with their axes in the streamwise direction, measured as large eddies and are proportional to the velocity deficit (Prooijen, Battjes, & Uijttewaal, 2005), as shown in Figure 4. Another source of momentum exchange is the variation of velocity in the vertical due to the logarithmic flow profile. The mass exchange in the mixing layer is due to secondary circulation induced by the interaction of the lateral and transverse velocity fluctuations (Shiono & Knight, 1991). The effect of the secondary circulations have been neglected this thesis.

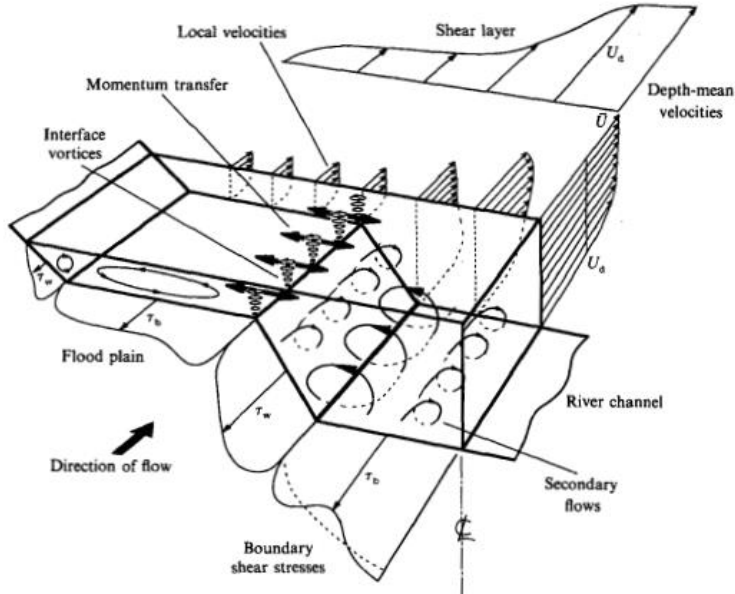


Figure 3; Hydraulic parameters associated with two-stage channel flow. Source: (Shiono & Knight, 1991)

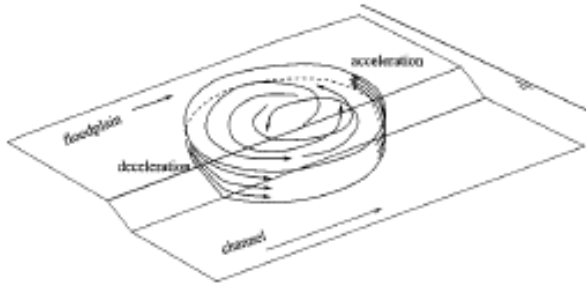


Figure 4; Sketch of vortex moving on an uneven bottom. Transverse velocity increases at the front and decreases at back of the vortex. Source: (Prooijen, Battjes, & Uijttewaai, 2005)

For the exchange of momentum in the mixing layer the relevant length and velocity scale are respectively the width of the mixing layer and the velocity gradient

Van Prooijen et al. used different length and velocity scales for the lateral shear due to bed friction (the flow depth and the depth average velocity) and the lateral shear due to the large eddies (the width of the mixing layer and the velocity difference). So that the turbulent viscosity consists of two parts:

$$\nu_t = \nu'_t + \nu''_t \quad (15)$$

$$\nu'_t = \alpha d \sqrt{\frac{g}{C^2}} U \quad (16)$$

$$\nu''_t(y) = \frac{d_m}{d(y)} \beta^2 \delta^2 \left| \frac{\partial U}{\partial y} \right| \quad (17)$$

With  $\alpha$  a constant, which should be of the order  $10^{-1}$  (Fischer, Imberger, List, Koh, & Brooks, 1979);  $d_m$  the average depth between the considered step in the water depth;  $\beta$  a constant, for which Van Prooijen et al. found a value of 0.07; And the width of the mixing layer  $\delta$  (Prooijen, 2004):

$$\delta = \frac{\Delta U}{\frac{\delta U}{\delta y}_{max}} \quad (18)$$

Using this representation of the shear stress it is possible to analytically solve the streamwise momentum balance over the transverse, resulting in a 2DH model of the compound channel. Using (18) Van Broekhoven (2007) constructed a 1D compound channel model in which exchange of momentum in the mixing layer can be modelled as:

$$\frac{1}{B} \int \frac{\partial d\tau_{xy}}{\partial y} dy = \rho \frac{d_m}{B} \beta^2 \Delta U^2 \quad (19)$$

Equation (19) rewrites a two-dimensional equation to a one-dimensional exchange process at the boundary of a channel compound. This allows the evaluation of the lateral exchange in a compound channel model, such as done by Van Broekhoven (2007)

### 2.3 Emerged groynes

For different stages of submergence of groynes different flow phenomena are observed. Firstly for emergent groynes Uijtewaal, Lehmann and Mazijk (2001) found a double gyre flow pattern in the groynes field for an equivalent (but downscaled) experiment geometry. The double gyre consisted of one major gyre with a smaller counterrotating gyre. The main gyre is induced by the momentum exchange via the mixing layer that starts at the groyne tip. The second gyre is fed by the main gyre. Also a mixing layer forms starting from the groyne tip. The width of the mixing layer increases downstream of the groyne tip till the following groynes. Also at the dynamic eddy sheds from the tip of the groynes and merges with the primary flow gyre, making place for another dynamic eddy. This flow pattern is later confirmed by Yossef (2005), while for a smaller aspect ratio between groyne length and spacing a single gyre is observed in the groynes field (Hüsener, Faulhaber, & Baron, 2012).

### 2.4 Submerged groynes

When the groynes become submerged the groyne field starts contributing to the conveyance capacity of the river as a region of accelerating and decelerating flow (Uijtewaal, 2005), (Hüsener, Faulhaber, & Baron, 2012), (Yossef, 2005) (Ambagts, 2019). This flow suppresses the gyre pattern observed for emerged groynes for high enough submergence levels (Uijtewaal, 2005).

The flow over and around groynes is a complex one. The flow over groynes consist of flow contraction followed by expansion downstream with a backward facing step. This is comparable to flow over a weir, but also to flow over obstacles, such a sand dunes or submerged breakwaters.

For that reason first flow over weirs is investigated and then flow around submerged obstacles. These will then be included in a summary of processes at submerged groynes. Lastly the numerical modelling of these processes is discussed.

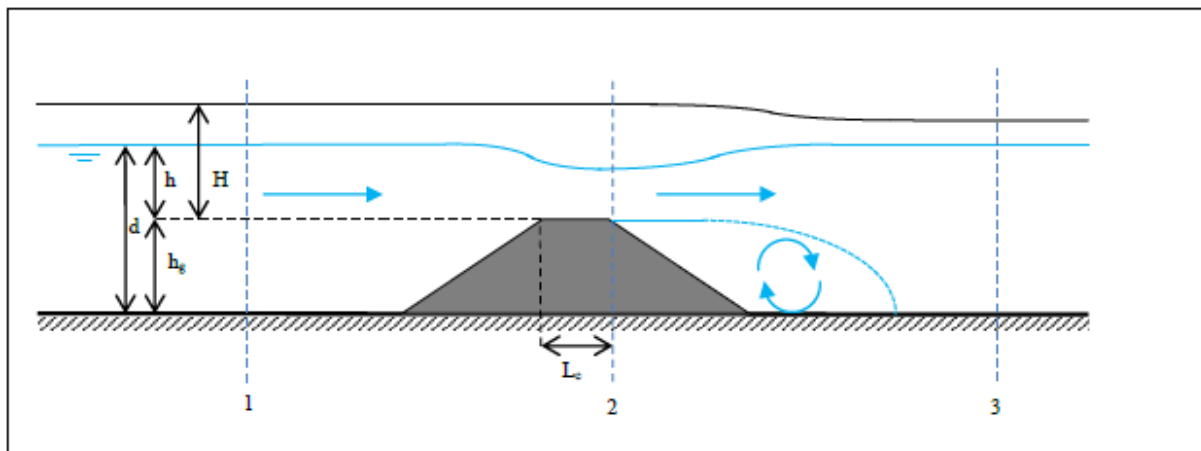


Figure 5; Parameters relevant for a submerged weir. Flow accelerates between areas 1 and 2. Energy is lost in a large gyre near the bottom between areas 2 and 3. Source: (Sieben, 2011)

### 2.4.1 Weir flow

The head loss over a weir is determined by the conservation of energy in contracting flow and conservation of momentum in expanding flow, such as visualized in Figure 5.

The capital  $H$  in Figure 5 stands for the energy head; the small  $h$  for the water level (relative to the groyne crest);  $h_g$  is the weir crest height;  $L_c$  the weir crest length. There are different flow regimes for flow over weirs, depending on the ratio of the upstream energy head to the groyne crest length. Jain (2001) made the following distinction:

$\frac{H_1}{L_c} < 0.1$	Long crested weir
$0.07 < \frac{H_1}{L_c} < 0.35$	Broad crested weir
$0.35 < \frac{H_1}{L_c} < 1.5$	Narrow crested weir
$1.5 < \frac{H_1}{L_c}$	Sharp crested weir

For a long and broad crested weirs the flow has time to adapt to the new depth with little curvature and can be assumed hydrostatic. The distinction between long and broad crested weirs is that for long weirs the energy loss over the crest (due to friction) cannot be neglected. For short and broad crested weirs there are still significant vertical velocities in the flow over the weir, resulting in non-hydrostatic flow, where for sharp crested weirs the flow does not reattach at all to the crest. Therefore for narrow and short crested weirs the vertical velocities and curvature of streamlines cannot be neglected. When using such a weir representation for groyne modelling a groyne will be short crested, as the crest length is only 3 cm, which classifies as a short crested weir for submergence levels of more than 4.5 cm. The effect of the vertical curvature of streamlines was observed by Ambagts (2019), and resulted in a separation zone behind the groyne that was higher than the groyne crest, indicating that a contraction parameter  $\mu$  is required when schematizing the flow over the weir.

#### Flow expansion at a backwards facing step

The flow dynamics of a backward facing step are shown in Figure 6, as investigated by Nakagawa and Nezu (1986). Directly downstream of the step the flow consists of the boundary flow that has become a decelerating free flow and recirculating zone. Between those a mixing layer develops. Between 5-6 steps in the streamwise direction the mixing layer reattaches to the bed, where a new boundary flow will gradually develop. The mixing layer is well described by a Gaussian distribution with high turbulent intensities in the mixing layer, related to the velocity gradient. In the recirculation cell there is a noticeable under pressure. Nakagawa and Nezu (1986) suggest this under pressure plays an important role in the formation of flow recirculation.

Flow over weirs is characterized by contraction upstream of the weir and expansion downstream of the weir. At contraction there is a loss of momentum, the flow acts on the weir. Locally the water level can be estimated by the conservation of energy upon flow contraction:

$$h_1 + \alpha \frac{U_1^2}{2g} = h_2 + \alpha \frac{U_2^2}{2g} \quad (20)$$

The loss of energy downstream is estimated from the conservation of momentum in an expanding flow:

$$\frac{1}{2} g (d_2 + h_g)^2 + q_2 u_2 = \frac{1}{2} g d_3^2 + q_3 u_3 \quad (21)$$

The equations (20) and (21) originate from the 1D shallow water equations, and only take into account the streamwise flow. The parameter  $\alpha$  is the part of the flow where the energy is concentrated. The subscripts 1-3 refer to the sections in Figure 5.



Based on the conservation of momentum Carnot determined the head ( $\Delta H$ ) loss downstream of a backwards facing step:

$$\Delta H = \frac{\Delta U^2}{2g} \quad (22)$$

Weir-like losses can be quite large and dominate the effect of bed friction. In that case the surface is flat, the water level slope is flat, except at the weir where there is a jump in the water level. Such as assumed by Kruijt (2013). The drop in the water level is then equal to the water level slope of the main channel over the length of the groyne field, such as visualized in Figure 7. If this is the case the modelling of groyne resistance can be simplified by only assuming weir like losses in the groyne field, neglecting the bed friction. This was suggested by Kruijt (2013) and Ambagts (2019). The analysis done in those reports were with models with a hydraulically smooth bed. Before oversimplifying our model it has to be verified whether the bed shear stress is important to model in the groyne field.

There are now multiple things to investigate between the compatibility between groyne and weir flow. The question is whether a groyne behaves like a weir. This can be split into two questions. Does the head loss over a groyne come from flow expansion that can be predicted by the conservation properties upon flow contraction and expansion? And can this expansion loss be predicted by empirical weir formula? If the answer of the first question is positive, that means that friction formula representing expansion losses are a good way to model groyne resistance. Then the second question becomes relevant to see how this groyne resistance can be modelled, preferably as close to existing weir formula as possible.

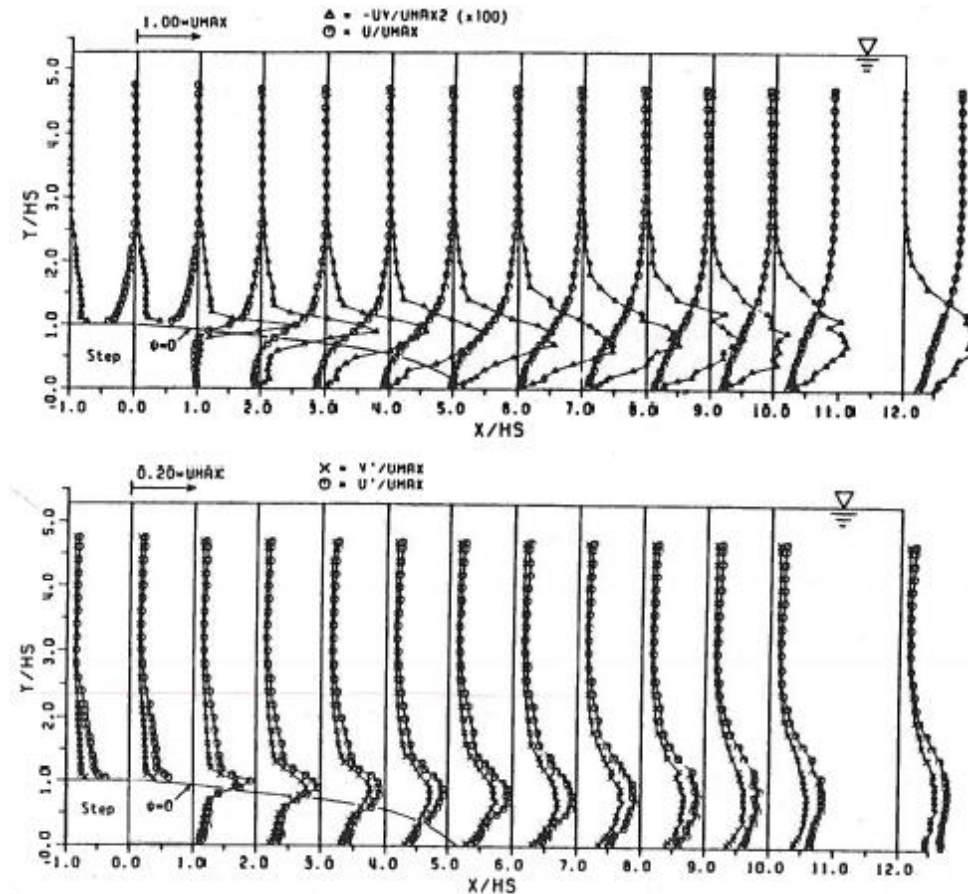
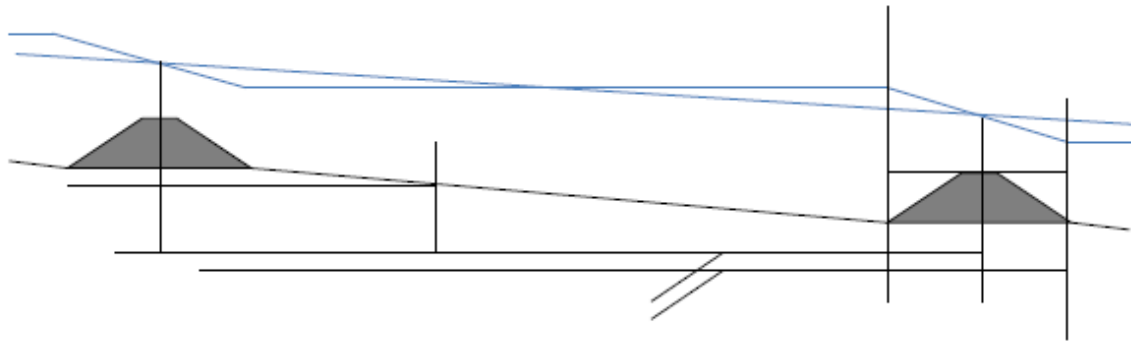


Figure 6; Example of flow downstream of a backward facing step. On top are shown the velocity and Reynold stress profile. Below are shown the turbulent energy profiles. All values were normalized by the velocity on the step. Source: (Nakagawa & Nezu, 1986)





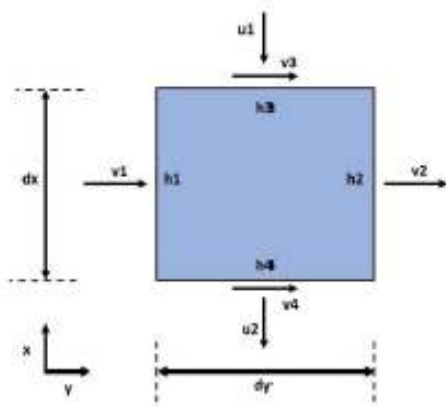


Figure 9; Control volume with the inclusion of lateral advection in the balance of momentum. Source: (Jansen, 2020)

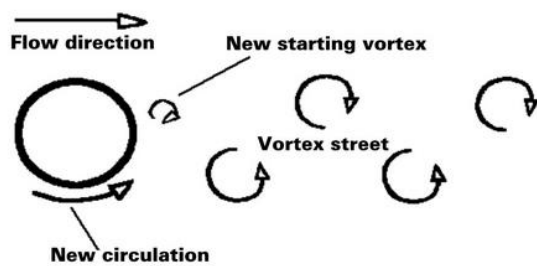


Figure 10; schematization of Von Karman vortices around obstacle. Source: (Prandtl & Tietjens, 2003)

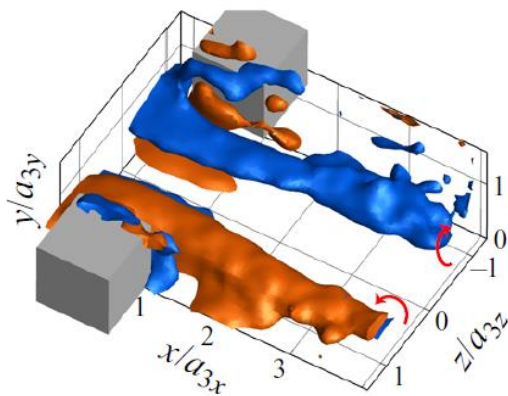


Figure 11; Visualization of flow over cubes, with a vertical spiraling flow downstream of the cubes. Source (Gao, Agarwal, & Katz, 2021)

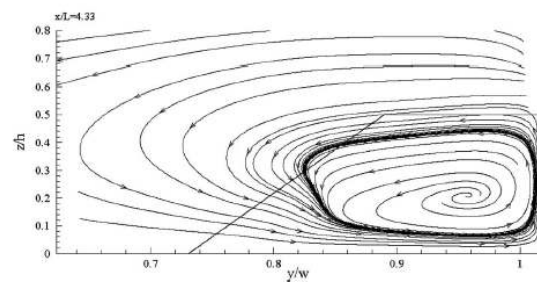
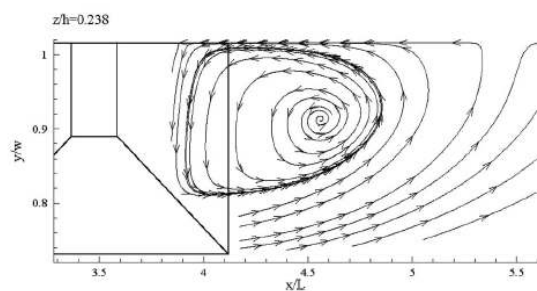


Figure 12; Flow circulation downstream of groyne tip in a:  $x - y$  (horizontal) plane; b:  $y - z$  (vertical) plane

### 2.4.2 Flow around obstacles

Flow around obstacles is often three-dimensional and governed by the complex interaction of different pressures in the horizontal and vertical direction in a flow. The overall effect of these flows is commonly quantified in empirical formula valid for certain shapes of obstacles. A good example of this is the horse shoe vortex around piles in a flow. (Schiereck, 2016)

Beside empirical quantification one can investigate the patterns of turbulent flows around an obstacle. The zone of comparability between groynes and obstacles is the groyne tip. At this region there is a large shear around the groyne tip. This should lead to vortex shedding. These would be Von Karman vortices originating from the groyne tip, such as shown in Figure 10. Another flow patterns that could develop around obstacles is spiraling flow. These spirals can originate from flow in river bends, with the size of the whole river section, to the flow over sand dunes, with the size of only a few centimeters (Tanner, 1963). Detailed investigation of flow over a pair of cubes in a flume allowed the visualization of the existence of spiraling flow downstream of the obstacles (Gao, Agarwal, & Katz, 2021), such as shown in Figure 11. Detailed numerical modelling of submerged groynes revealed that at the groyne tip there is a circulation pattern in the  $x - z$  plane, that is coupled to the flow separation downstream of the groyne, but that there are also circulation patterns downstream of the groyne tip in the  $x - y$  plane and  $y - z$  plane (Kuhnle, Jia, & Alonso, 2008), as shown in Figure 12. Measurements and simulations done by Kuhnle et al. (2008) show that flow around the groyne tip is truly fully three-dimensional.

### 2.4.3 Interaction with mean flow

#### **Redistribution of discharge**

Being an obstacle in the flow a groyne imposes a resistance on the flow section. Due to this resistance the velocity distribution between the main channel, groyne field and floodplain alternates compared to a situation without groynes. With more resistance in the groyne field a larger portion of the flow goes through the main channel and floodplain. The resistance of the groyne increases the resistance of the total flow section, but this is partly levelled by a redistribution of the discharge. This affects multiple terms in the streamwise momentum balance (2): the streamwise advection, the bed shear stress and the shear stress in the mixing layer.

#### **Increased exchange of momentum in horizontal mixing layer**

In the main channel and floodplain the velocity increases, which increases the bed shear stress and the advection. In the groyne field the velocity decreases, which decreases the bed friction and the advection. The exchange of momentum increases between the main channel and the groyne field, and decreases between the groyne field and mixing layer.

It is important to quantify the redistribution of discharge. This is a benchmark for analysing the groyne resistance. The question is not only whether a groyne resistance model can predict the water level slope, but also whether it can predict the discharge distribution between the different channel compounds as a sign of modelling the correct friction at the correct locations.

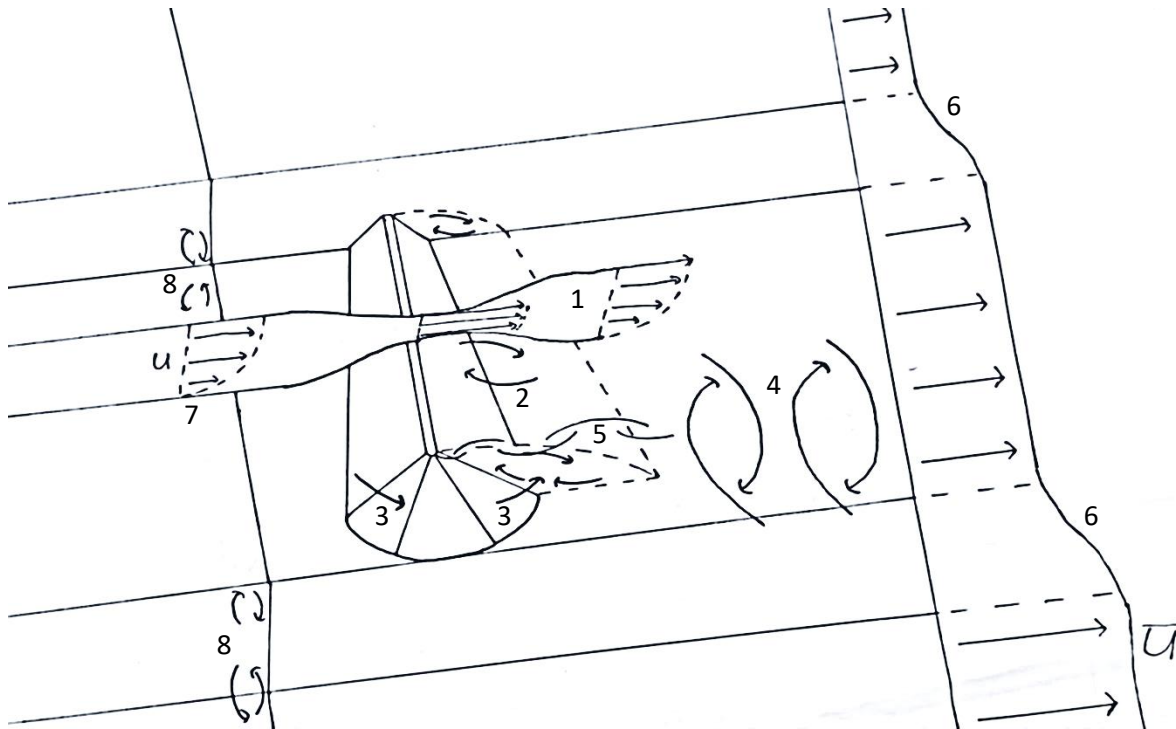


Figure 13; visualization of physical flow processes in a channel with groynes. 1: Flow contraction and expansion over groyne crest; 2: Vertical separation cell downstream of groyne crest; 3: Lateral flow at groyne tip as a compound weir flow; 4: Vertical spiral flow around an obstacle; 5: vortex shedding from groyne tip; 6: Momentum exchange in horizontal mixing layer; 7: Logarithmic flow profile determined by bed shear stress; 8: secondary flows associated with compound channel flow

#### 2.4.4 Synthesis of flow processes associated with submerged groynes

Figure 13 visualizes the flow processes associated with groynes. The different processes all have different effects on the flow and may interact. Our biggest interest is however how to observe them in the physical model. The relevant physical processes described include:

1. Flow contraction and expansion;
2. Vertical separation of flow;
3. Lateral flow at groyne tip;
4. Spiral flow;
5. Eddy formation at groyne tip;
6. Momentum exchange in horizontal mixing layer

##### Flow contraction and expansion

The weir like behaviour of submerged groynes is related to the contraction and expansion of flow over the groyne. This can be seen in an increase of flow velocities and decrease of water level toward the groyne, and vice versa downstream of the groyne. Expansion losses at a backwards facing step should be predictable as a Carnot head loss. To determine the Carnot head loss it is necessary to measure the flow and water levels on the groyne crest and downstream of the groyne, where the flow is expanded. Flow contraction can be examined by measurement of the flow and water level upstream of the groyne and on the groyne crest.

##### Vertical separation of flow

Vertical flow separation downstream of the groyne pairs with flow expansion, as long as the flow cannot stay attached. This is the when the downstream slope is steep and the flow cannot follow the topography. The flow separation induces a distinct flow pattern of negative flow velocities, a mixing layer and a free layer downstream of the groyne and can be measured by measuring multiple transect downstream of the groyne. The separation zone can be visualized by injecting dye just downstream behind the groyne. Observing the separation zone confirm firstly the importance of head loss due to flow expansion and secondly that a large part of the energy loss comes from the highly turbulent reattachment of the flow.

Yossef observed a very small influence of the groyne on the water level, which could not be explained by weir head loss formula (2005). Jongeling et al. (Jongeling, Goede, & Keser, 2012) suggested that the low groyne resistance was due to lateral levelling of the under pressure in the vertical separation zone downstream of the groyne. With the flow expanding into the groyne field downstream of the groyne the flow adds a positive streamwise flow velocity to the recirculation cell. This way it dampens the recirculation of flow in the vertical separation cell. Making the negative flow velocities less negative. This would reduce the force with which the separated flow is pulled back to the bed and once it does reattach it would lead to a reduced turbulent bottom attack, where less dissipation of energy head takes place. This is a speculation only, but is to this day an important part of the discussion concerning the correct approach of groyne modelling. Characteristic for this explanation are a large lateral inflow into the recirculation cell, a larger reattachment length and a lower under pressure in the recirculation cell. Measurements that suffice to verify this idea include the measurement of water pressure and require three-dimensional flow observations. These measurements fall outside the scope of possibilities for this research. One can get an idea of the validity however by comparing the length of the vertical separation zone by those of a normal backwards facing step.

### Lateral flow at groyne tip

The expected lateral flow at the groyne tip is the least documented from the mentioned flow processes. Yossef (2005) did mention a alternating pattern of flow over and around a groyne as explanation for very large scale turbulent flows, with periods of 30 – 60 seconds. The observation originated from the autocorrelation of the transverse velocity signal as shown in Figure 14. The suggestion of sideways levelling also builds on the lateral flow around a groyne. To verify the compound weir flow it is necessary to measure the lateral flow velocities upstream and downstream of the groyne. Lateral flow can be challenging to measure. For that reason it is relevant to measure the discharge at the groyne and upstream and downstream of the groyne. Differences between the discharge on top of the groyne and upstream and downstream of the groyne indicate lateral flow at those locations.

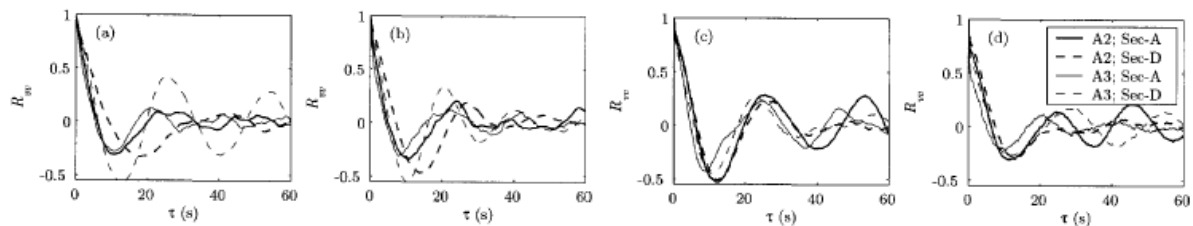


Figure 14; Autocorrelation functions in flume with submerged groynes. Large consistent fluctuations in the time signal were observed. Source: (Yossef, 2005)

### Spiral flow and eddy formation at groyne tip

Spiral flow and vortex shedding are three dimensional processes that can be difficult to measure in a physical model and are difficult to quantify in a two dimensional numerical model. Vortex shedding should be visible by visual observations as whirls in the flow originating from the flow tip. Spiral flow is more difficult to measure without extensive three-dimensional measurements. Particle tracking at the surface might show lateral surface flows, which indicate a counteracting lateral flow at the bottom. If those patterns are observed two-dimensional numerical models should be tuned accordingly.

### Momentum exchange in a horizontal mixing layer

In the shear layer there is a momentum transfer, influencing the channel resistance. The lateral exchange is a source of extra resistance groynes add to a flow due to the forced redistribution of discharge compared to the situation without groynes. A shear layer can be observed as a gradual variation of the streamwise flow velocity. When the shear layer have a small width and the velocity gradients are large, large eddies will be visible in the shear layer. These should be visible as periodic signals in the autocorrelation function of the transverse velocity in the mixing layer. It should also be possible to see those large eddies with visual observations, as whirls in the water. From the width and shape of the mixing layer it is possible to estimate the empirical parameters in exchange formula's, such as equation (17).

### 2.4.5 Modelling of submerged groyne resistance

Modelling of groyne resistance can be done on many different levels. Different levels of detail arise from different needs. For design and decision making time and money limits the possibilities of numerical modelling, for which two dimensional (subgrid) models are the standard. Theoretical investigations include the three-dimensional (non hydrostatic) modelling. And for analytical comparisons one can use simple one-dimensional compound channel models

#### Analytical expressions for groyne resistance

Modelling of this contraction and expansion in the Dutch river system is done using an interpolation between a perfect weir formula and an empirical formula for submerged short crested weirs (Sieben, 2011):

$$q = q_p \sqrt{1 - \left(\frac{H_3}{H_1}\right)^p} \quad (24)$$

$$q_p = C_Q \left(\frac{2}{3}\right)^{\frac{3}{2}} \sqrt{g} H_1^{\frac{3}{2}} \quad (25)$$

$$C_Q = C_1 \left( e^{-\frac{0.5H_1}{L_c}} (1 - 0.25 e^{-0.5m_u}) + \left(1 - e^{-\frac{0.5H_1}{L_c}}\right) (0.8 + 0.65 e^{-0.1m_d}) \right) \quad (26)$$

$$p = \frac{6.75}{C_Q^2} \left( \left(1 + \frac{h_g}{H_1} \left(1 - e^{-\frac{m_d}{C_2}}\right)\right)^{-2} - \left(1 + \frac{h_g}{H_1}\right)^{-2} \right)^{-1} \quad (27)$$

With  $q_p$  the flow over a perfect weir;  $C_Q$  a reduction coefficient of perfect weir flow related to the geometry of the weir;  $p$  a representation of the expansion losses based on the Carnot head loss;  $H_1$  the energy head upstream of the weir relative to the weir crest;  $H_3$  the energy head downstream of the weir relative to the weir crest;  $L_c$  the length of the slope crest in streamwise direction;  $m_u$  the upstream slope of the groyne; and  $m_d$  the downstream slope of the groyne and  $C_1$ ,  $C_2$  calibration coefficients, for which  $C_1 = 1$  and  $C_2 = 10$  to match the Tabellenboek measurements (Sieben, 2011) and  $C_1 = 0.8$  to match the Bloemberg measurements. For hydraulically rough weirs a  $C_2 = 30$  is required (Rijkswaterstaat, 2016). These values are not representative for groyne lowering. It will overestimate the head loss reduction due to modelling all groyne flow as 1D weir expansion losses (Zagonjoli, 2017). A sensitivity analysis conducted by Yossef and Visser (2018) furthermore showed that the formula becomes very sensitive under high submergence, when  $H_3$  is almost as large as  $H_1$ , and that the formula is too sensitive to changes in the downstream slope  $m_d$ .

The formula is not used calculating discharge over a structure however, but is used to determine head losses over a groyne or weir, with the discharge derived from local conditions, so that an extra head loss is added to the momentum equation to represent the effect of the weir:

$$\frac{\Delta H}{H_1} = 1 - \left( 1 - \frac{q^2}{C_Q^2 \left(\frac{2}{3}\right)^3 g H_1^3} \right)^{1/p} \quad (28)$$

For highly submerged groynes the formula approaches the empirical formula used by Villemonte (1947):

$$q \approx q_p \sqrt{p \frac{\Delta H}{H_1}} \quad (29)$$

From (29) it becomes visible that the upstream contraction is no longer relevant and that  $C_Q$  is out of the equation, the weir head losses are completely determined by the expansion losses. In this formula the expression for  $p$  is derived from the Carnot head loss upon flow expansion. But because of how  $p$  is

constructed the formula has multiple asymptotes where  $p \rightarrow \infty$ . This happens when  $h_g \rightarrow 0$ ,  $H_1 \rightarrow \infty$  and  $e^{-\frac{m_d}{C_2}} \rightarrow 0$ . The first asymptote means that the groyne no longer exists. The second asymptote means that the submergence is that large that the groyne is negligible. The last asymptote means that the flow can expand very gradually without expansion losses. This means that modelling of groyne lowering happens in a very sensitive range of the formula, where  $p$  can quickly go to infinity, especially for high submergence levels.

Yossef investigated the possibility to model the groyne as a resistance element as a method to explain the minor impact of weirs observed in the flow. In such a schematization the groyne head loss is a resistance, and is solved in the same way as bed friction (Yossef, 2005):

$$\frac{g}{C_{effective}^2} = \frac{g}{C_{base}^2} + \frac{1}{2} C_D \left( \frac{h_g}{S} \right) \quad (30)$$

In this formulation the ratio of groyne height to spacing is already included. According to Kruijt (2013) two formulations for the representation of groyne resistance could be usable for numerical modelling. The first was proposed by Yossef (2005):

$$\frac{C_D}{Fr^2} = \alpha_1 \left( \frac{h_g}{d_{gf}} \right)^{\alpha_2} \quad (31)$$

In the formulation the Froude number and the blockage ration are included, with  $\alpha_1 = 76.4$  and  $\alpha_2 = 3.7$ , with a larger Froude number indicating higher flow velocities and larger velocity differences. The values of  $\alpha_1$  and  $\alpha_2$  were obtained fitting an 1D single channel momentum balance equation on measured data. The formula was fitted on the observed Froude number in the main channel. The parameters  $\alpha_1$  and  $\alpha_2$  might need recalibration for that reason when using the Froude number in the groyne field as predictor of the groyne resistance. The experiments were performed for blockage ratios  $h_g/d_{gf} = 0.59 - 0.97$  in the range of  $Fr = 0.08 - 0.25$ .

The second formulation was suggested by Broekhoven (2007) assuming a quadratic influence of the blockage ratio, and only including the blockage ratio:

$$C_D \left( \frac{h_g}{h_{g;0}} \right) = 1.79 \left( \frac{h_g}{d_{gf}} \right)^2 - 0.08 \left( \frac{h_g}{d_{gf}} \right) + 0.07 \quad (32)$$

The formulation by Van Broekhoven was developed for the determination of the effect of changing the blockage ratio compared to the existing situation. The friction coefficient was determined by the integration of the momentum equation over the groyne modelled in a numerical two-dimensional vertical flow model over (lowered) weirs. It was assumed that the force acting on the groyne was a drag force. The determined values of  $C_D$  were then fitted on the blockage ratio. The experiments were performed for blockage ratios  $h_g/d_{gf} = 0.1 - 0.4$ .

Kruijt (2013) observed a large difference between the modelled head loss using weir head loss formula or friction loss formula. This is an expected result, as Yossef developed the formula because the weir head loss formula could not explain the groyne head loss in his experiment. But the friction formula by Van Broekhoven is based on a numerical two-dimensional vertical model of flow over a weir. This numerical model does solely model flow expansion over a weir and fits an expression based on the blockage ration on the integrated full momentum balance. Both Van Broekhoven and Villemonte are therefore closely related to the theoretical flow over weirs. The observed difference in their effect by Kruijt is for that reason unexpected. Kruijt (2013) suggested that the inclusion of the blockage ratio in the power  $p$  in Villemonte might be the problem, which is very sensitive to small changes for certain cases, as already explained.



### One-dimensional compound channel modelling

One-dimensional models can give crude estimates of processes. Furthermore, deriving expressions for flow resistance in a one dimensional sense can help two-dimensional modelling when the flow resistance can be derived from the momentum equations in the flow. One dimensional models can't model lateral flows within the channel compounds, but can include integrated effects of it as an effect of secondary circulations. Furthermore shear between channels can be modelled as an interface effect. The effect of lowering the groyne tip in an analytical model to better represent the real groyne tip can be investigated however by finding an analytical expression which closes equation (23). The existence of lateral flow then gives an extra contribution to the streamwise momentum balance.

The basis of a compound channel model are equations (1) and (2). The momentum balance in the transverse direction is neglected as  $V = 0$ . Applying this to equation (1) results in:

$$\frac{\partial dU}{\partial x} = 0 \rightarrow -U \frac{\partial d}{\partial x} = d \frac{\partial U}{\partial x} \quad (33)$$

Implementing this into equation (2), and implementing all other contributions listed in chapter 2 results in a momentum balance for each channel compound:

$$-\rho U^2 \frac{\partial h}{\partial x} + \rho d g \frac{\partial h}{\partial x} + \rho \frac{g}{C^2} U^2 + \Gamma + \rho \sum \frac{d_m}{B} \beta^2 \Delta U |\Delta U| = F_{external} \quad (34)$$

Which read from left to right: the advection, which can't be neglected in our model with no bed slope; the pressure gradient; the bed shear stress; the secondary circulations; the exchange of momentum in the (multiple) mixing layers; and external forcing or head losses. These external losses can be the groyne head losses. All terms are in  $[N/m^2]$ .

For each channel compound there is a balance of momentum, and the discharge is conserved over all channels. When assuming an equal water level slope in each channel this results in four equations from which one can solve the flow velocity in each compound and the water level slope  $(U_{mc}, U_{gf}, U_{fp}, \frac{\partial h}{\partial x})$  based on the boundary conditions  $(Q, h)$ . The analytical models can in this form be used to assess the influence of different physical processes and give an estimate of the magnitude of those relevant for numerical modelling.

To compare the analytical models with each other they can be rewritten to all represent the head loss. This is done by getting the drag resistance predicted by Yossef and Van Broekhoven out of bed shear coefficients, and by separating the head loss  $\Delta H$  from the Villemonte formula, in which  $\frac{F_{external}}{\rho d_{gf} g} = -\frac{\Delta H g}{S}$ :

$$Yossef (YOS): \frac{\Delta H_g}{S} = 38.2 \left( \frac{h_g}{d_{gf}} \right)^{3.7} \left( \frac{h_g}{S} \right) Fr^2 \quad (35)$$

$$Van Broekhoven (BRO): \frac{\Delta H_g}{S} = \left( 0.358 \left( \frac{h_g}{d_{gf}} \right) - 0.01 + 0.014 \left( \frac{h_g}{d_{gf}} \right)^{-1} \right) \left( \frac{h_g}{S} \right) Fr^2 \quad (36)$$

$$Villemonte (VIL): \frac{\Delta H_g}{S} = \frac{4}{27} \left( \left( 1 + \frac{h_g}{H} \left( 1 - e^{-\frac{m_d}{C_2}} \right) \right)^{-2} - \left( 1 + \frac{h_g}{H} \right)^{-2} \right) \left( \frac{d_{gf}}{H} \right)^3 \frac{H}{S} Fr^2 \quad (37)$$

In this formulation it is possible to compare all formula with the observed head loss over groynes, and see how each of the formula compare to the observed Carnot head loss. In the equation we distinguish:  $\Delta H$ : the head loss over the groyne;  $S$ : the groyne spacing in the streamwise direction;  $h_g$  the height of the groyne crest relative to the bed of the groyne field;  $d_{gf}$ : the water depth in the groyne field;  $Fr$ : The Froude number in the groyne field;  $H$ : the energy head upstream of the groyne relative to the groyne crest;  $m_d$ : the downstream slope of the groyne;  $C_2$ : a calibration factor ( $= 30$ ).

### Two-dimensional subgrid modelling

Simplified numerical models use a large grid size in which the groynes cannot be included in the topography. Head losses associated with groynes can in such model only be predicted by engineering formula. Two-dimensional models do model lateral flow and compound weir flow, but are limited to the



weir or groyne head loss formulation used to predict the head loss. For this reason subgrid models are calibrated on experimental data. There is a profound lack of data to calibrate subgrid models on concerning flow over submerged groynes, and especially flow over the groyne tip (Omer & Yossef, 2017). The calibration of weir formula on measurement data can be done by fitting the empirical parameters in weir formula to the observed flow, where:

$$q = C_d q_p \quad (38)$$

Here  $C_d$  is the residual from the difference between the actual observed discharge  $q$ , and the discharge that would flow over a perfect weir  $q_p$ . With sufficient data of empirical values of  $C_d$ , that represent all cases relevant for the Dutch river system for flow over groynes, one can always make a formula that can represent flow over groynes.

### **Two-dimensional modelling including groynes in topography**

A more detailed modelling of groynes would include them in the topography. In such a model the head loss over groynes is directly solved by the change in topography. Not all numerical models will model the correct head loss over obstacles however. The standard cyclic scheme in Delft3D for example is based on a non-conservative form of the momentum balance. But there are also numerical schemes with strong or weak conservative properties, which apply the conservation of energy or conservation of momentum on the correct places, such as the Delft3D flooding scheme (Zijlema, 2011). These two-dimensional models do not model three-dimensional flows however. Flows not described by the conservation of mass, momentum or energy over the horizontal, such as spiralling flow, or vortex shedding, cannot be resolved in a two-dimensional model with groynes in the topography without tuning of the model. The required tuning therefore reduces the economic value of such a model, as the increased time required to model groynes in a dense grid still requires experimental data to fit the parameters that represent the three-dimensional processes.

### **Three-dimensional non-hydrostatic modelling**

The most advanced model is a three-dimensional non-hydrostatic model. The accuracy of a three-dimensional model is determined by the density of the grid. The denser the grid, the more processes and turbulent processes can directly be solved in a Large Eddy Simulation. Setting up a three-dimensional model is expensive however and therefore constrained to research purposes mainly. There are few attempts undertaken on the three-dimensional modelling of flow over submerged groynes. One of those is the modelling done by Ambagts (2019). He was able to reproduce the flow in a physical model in a three-dimensional non-hydrostatic model. The main energy sink to correctly model the discharge distribution between the groyne field and main channel was the exchange of momentum in the horizontal mixing layer. The correct head loss over the groyne could only be obtained by fitting certain overshoot factors to accept near-bed overshoot. This allowed the correct modelling of flow separation and attachment. This was only possible in Finel however and required manual tuning. Furthermore the Finel model was only investigated little. It is also possible to do three-dimensional non-hydrostatic modelling in Delft3D, such as done by Chavarrias (2019) (2020). There is a large difference between the results of two- and three-dimensional modelling (Ambagts, 2019) (Zagonjoli, 2017). The non-hydrostatic z-layer model in Delft3D is not verified however for flow over weirs or groynes. Therefore two-dimensional models cannot be fitted on three-dimensional models as long as sufficient data from physical modelling lacks on which submerged groyne modelling can be calibrated.

## **2.5 Summary**

A pressing issue is the lack of data on which numerical models can be based for the modelling of submerged groynes. For simulations in a physical model it is therefore more relevant to have many measurement points, than to have very detailed measurements. From these measurements values discharge coefficient follow on which numerical models can be fitted. For the comparability between groynes and weirs it is important to assess the expansion of flow over the groynes and see whether expansion over a groyne is comparable to that of a normal backwards facing step, and see whether the groyne head loss can be predicted by the Carnot expansion losses. Furthermore it is important to assess the influence of lateral advection at the groyne tip and assess whether at the groyne tip flow expands at all.

## 3 Methodology

The mayor constraint in determining the groyne resistance is the lack of data from physical models or from flow measurements in the rivers under high water. For this reason a physical model is set up which allows the determination of the groyne resistance in a controlled environment.

### 3.1 Model description

Pictures of the physical model are shown in Appendix I

#### Dimensions

The model itself consists of a 5 m wide and 36 m long flume in which a geometry, representing a section of the Waal with groynes (Figure 15), is constructed out of concrete. On the concrete gravel with a diameter of 4-8 mm is glued with a density of approximately 5500 stones/m<sup>2</sup>, representing rough bottom conditions. The bed roughness is shown in Figure 81. The geometric scaling is 1:30, based on scaling concerns, as demonstrated by Uijtewaal (2019). The resulting physical model is schematized in Figure 16. The groyne model neglects the tip of the groyne protruding into the main channel.

#### Groyne field and groynes

The groynes are spaced 6 meters apart, as shown in Figure 19. With that 6 groynes can be constructed in the model, resulting in 5 groyne fields. The groynes and groyne fields are numbered from upstream to downstream as shown in Figure 19. The used groyne geometry is shown in Figure 17 and Figure 18. The main elements are a crest width of 3 cm, a crest height of 10 cm with respect to the lowest point of the groyne field, or 20 cm to the bed level of the main channel, and a slope of 1:3 on all sides, with a rounded tip. The groyne field is 10 cm above the main bed sloping upwards with a slope of 1:25.

#### Boundary conditions

The wall closing of the main channel consists of a smooth concrete and a glass part. The wall closing of the floodplain consists of smooth wooden panels. At the inflow boundary the water flows through a flow straightener followed by a floating wave damper to ensure smooth unidirectional flow in the flume. At the outflow area the water enters a small basin in which an adjustable overflow weir is constructed as well as a pump. In the small basin the flow isn't unidirectional, but towards the specific points of the pump and overflow weir.

#### Adaptation length

The inflow is uniformly distributed at the inflow boundary, as all the water levels are still the same over the cross-section. This gives a different equilibrium flow profile over the cross section at the inflow than in groyne field and floodplain downstream. Furthermore the boundary layers between the floodplain and groyne field and main channel need space to develop as well as the bottom boundary layer. Given the small number of groyne fields the adaptation length of these processes is expected to have a large influence on the model, as pointed out in preliminary numerical simulation of the experiment (Chavarrias, Platzek, & Yossef, 2019). Furthermore the first groyne is expected to give a large backwater due to the uniform distributed inflow boundary (Zagonjoli, Platzek, & Kester, 2017). Based on previous research (Uijtewaal, Lehmann, & Mazijk, 2001) it is expected that the inflow boundary influences the discharge distribution in the first two groyne fields, so the third and fourth groyne field can be used for gathering knowledge on the processes around groynes. In the fifth and last groyne field an influence of the outflow boundary is expected (Yossef, 2017). But ultimately the influence of the boundaries have to be measured to determine where useful information can be gathered to obtain insight in the flow around groynes, and where the boundary conditions are being measured.

#### Water level and discharge regulation

The flume has two mechanisms for regulating the water level and the discharge. Firstly there is a pump pumping water around the flume. Secondly the flume is fed from the water reservoir, with the excess water leaving the flume through an adjustable overflow weir into the reservoir. In the flume the weir mainly controls the water level in the flume, as water levels higher than the weir will overflow into the basin. The discharge in the flume is fully determined by the pump. The inflow from the basin just compensates for the overflow and leakage through the overflow weir. It can be understood in such a way that in an equilibrium situation the discharge is determined by the power of the pump. The inflow from the basin just assures a constant water level as water is leaving the flume through the overflow

The graph illustrates the elevation profile of the Krib and Kribyak channels. The y-axis represents the height in meters (0 to 14), and the x-axis represents the distance in meters (0 to 150). The red line indicates the maximum water level at 12 meters. The yellow line shows the original dike profile, which drops from 7.5 meters to 6 meters at 90 meters. The blue line shows the ditch profile, which drops from 7.5 meters to 0 meters at 95 meters. The light blue line shows the profile of the lowered dike, which drops from 7.5 meters to 4.5 meters at 90 meters. The inset diagram shows a plan view of the channel layout with dimensions: 60 m, 32 m, 7 m, 25 m, and 2.5 m.

The graph illustrates the longitudinal profile of the river bed. The y-axis represents the elevation  $z$  in meters, ranging from 0.000 to 0.300. The x-axis represents the distance  $y$  in meters, ranging from 0.000 to 5.000. The profile is divided into three sections: floodplain (0 to 1.0 m), groyne area (1.0 to 3.0 m), and main channel (3.0 to 5.0 m). The blue line represents the original bed, and the yellow line represents the bed after groyne placement. The groyne area shows a significant reduction in bed elevation, from 0.250 m to 0.100 m.

Section	Distance $y$ (m)	Original Bed $z$ (m)	Bed after Groyne $z$ (m)
floodplain	0.000	0.250	0.250
	1.000	0.250	0.250
groyne area	1.000	0.175	0.200
	3.000	0.100	0.100
main channel	3.000	0.100	0.100
	5.000	0.000	0.000

Side view groyne

Transverse coordinate in flume in [m]	Elevation in flume in [m] (Blue Line)	Elevation in flume in [m] (Orange Line)
2.0	0.2	0.1
2.1	0.2	0.1
2.2	0.2	0.1
2.3	0.2	0.2
2.4	0.2	0.2
2.5	0.2	0.2
2.6	0.2	0.2
2.7	0.2	0.2
2.8	0.2	0.2
2.9	0.2	0.2
3.0	0.2	0.2
3.1	0.2	0.2
3.2	0.2	0.2
3.3	0.2	0.2
3.4	0.2	0.2
3.5	0.2	0.2
3.6	0.2	0.2
3.7	0.2	0.2
3.8	0.2	0.2
3.9	0.2	0.2
4.0	0.2	0.2

21

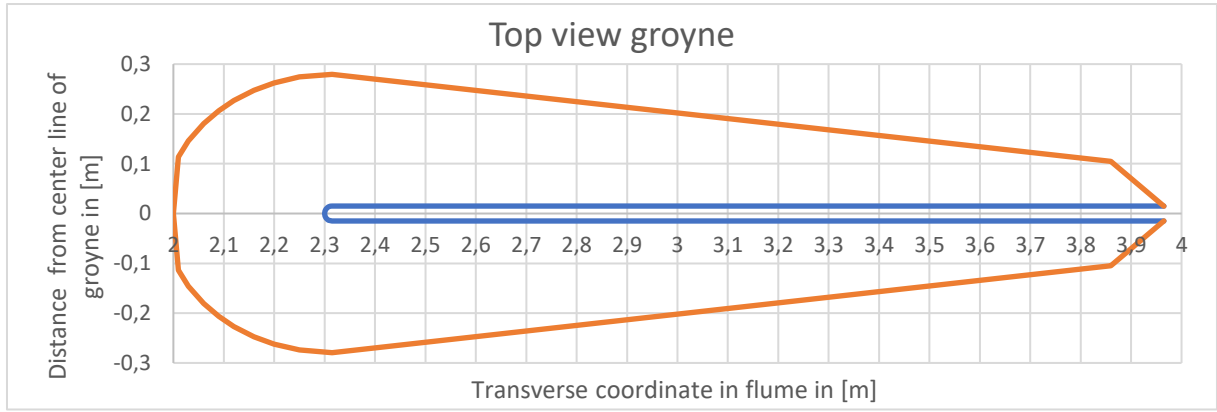


Figure 18; Top view groyne

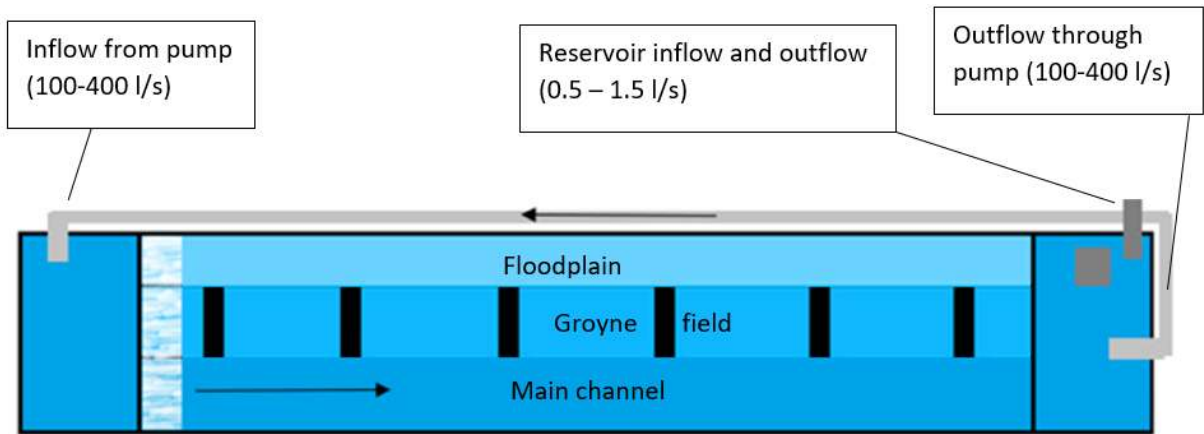


Figure 19; Sketch of experiment. In light grey the recirculating water pipe. In dark grey the in- and outflow from the reservoir. A wave damper is installed at the inflow of the experiment.

### 3.2 Measurement techniques

In the experiments 6 Electromagnetic Flowmeters (EMS's) owned by the TU Hydraulic Laboratory are used for all experiments. These are used together with laser altimeters for the measurement of the water level. This is used in combination with PTV surface velocity measurements in the third and second groyne field.

#### 3.2.1 EMS

An EMS is a point measuring device, measuring the velocity of water in the horizontal plane. An EMS has a probing volume of a few cubic cm, which suffices to measure large scale turbulent structures. The sampling frequency is 25 Hz, which gives the smallest observable timescale for turbulence. Each measurement is done for 5 minutes to capture the large scale turbulent motions in the mixing layers. The signal in volts  $V$  is converted to velocities  $U$  by the formula:

$$U = -0.000188 \cdot V^2 + 0.1023 \cdot V + 0.002 \quad (39)$$

#### Uncertainty in EMS measurements

There are different uncertainties associated with the measurements. First of all there is an uncertainty in the location of the EMS. The horizontal measurement locations are set relative to a grid constructed on the experiment and has an precision on 2 mm in the transverse direction and 5 cm in the streamwise direction. In the vertical the position of the measurement locations has a precision of 0.3 mm.

The accuracy of the EMS is  $\pm 0.01$  m/s  $\pm 1\%$  of the measured value as provided by the manufacturer (Deltares, 2020). The observed accuracy of repeated measurements is  $\pm 0.003$  m/s, which confirms the accuracy as provided by the manufacturer. The devices measures the velocity relative to manually

determined zero, the background reading. This background measurement depends on the geographical location of the EMS. The background measurement is sensitive to the water level and the proximity of walls. Therefore for each EMS the background has to be measured for each different location in the transverse direction. Furthermore there is a drift of the measured signal, which by manufacturing standards is 0.1 V over 24 h at most (Deltares, 2020). The observed daily drift is up to 0.2 V however.

Generally the EMS were off their calibration, such that a calibration factor needs to be applied before applying equation (39). Due to timing of the experiments calibration of the devices was done after all experiments were finished. All devices measured larger voltages than the standard calibration. The difference between the used state and calibrated state is only of a multiplication factor. This difference is accounted for in this thesis. The effect of the calibration is positive regarding errors, as all velocities are reduced compared to the measured velocities. The total formula to determine the velocities from the readings including the calibration and the offset are:

$$U = -0.000188 \cdot (C_c(V - V_0))^2 + 0.1023 \cdot (C_c(V - V_0)) + 0.002 \quad (40)$$

With  $U$  the measured flow velocity in [m/s];  $V$  the reading in [V];  $V_0$  the zero measurement at the start of one day in [V];  $C_c$  the calibration factor for each device differently due to calibration to the factory standards in hindsight of the measurements [-].

### 3.2.2 PTV

Particle Tracking Velocimetry (PTV) follows individual particles over an surface, in this experiment the free surface. A camera is hung above the experiment and is able to see from  $x = 11.8$  to  $x = 25.4$  m, which includes the third and fourth groyne, the third groyne field, and 3 m upstream of the third groyne and 4 m downstream of the fourth groyne. In the flume floating particles will be distributed of  $2 \times 2$  cm. The camera has a shooting speed of 24 Hz. With the large particle size only mean velocities can be observed.

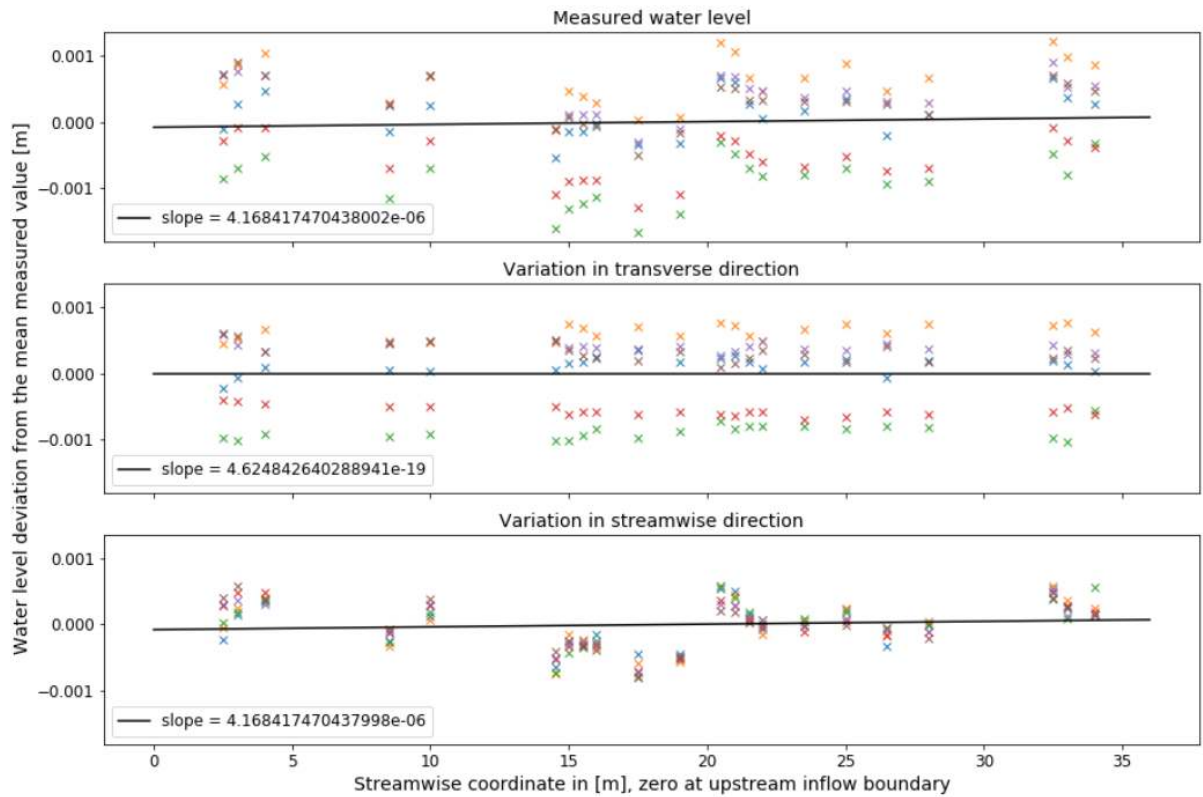


Figure 20; Measured water level on still water over the flume; different measurement points at one location correspond to different locations in the transverse. The upper plot the measured water level; the middle plot the same measurements minus the mean water level measured in each streamwise coordinate; the lower plot the measured water level minus the mean water level in each device.

### 3.2.3 Laser altimeters

A laser is a measurement device for measuring elevations. The laser measures in a range of 6 – 26 cm below the device with a frequency of 750 Hz. For the laser to measure a distance it has to reflect on a surface. A piece of paper is placed below every device, floating on the water, so the laser measures the distance between the laser and the water surface. The laser is mounted on a height adjustable standard. The lasers are calibrated on in the bottom of the roughness 33 m downstream in the experiment.

#### Uncertainty in laser measurements

The resolution of the laser is 40  $\mu\text{m}$ , or  $4.0 \cdot 10^{-5}$  m (Micro-Epsilon, 2008). Sources of uncertainty are the light from other sources, colour differences of the measured surface, temperature differences, mechanical vibrations, movement blurs, surface roughness and measured surface angles (Micro-Epsilon, 2008). Different uncertainty sources play a role when determining a uncertainty of a measurement. Each point is measured 3-5 x 5 minutes due to the way the experiment is setup. The observed standard deviation of such consecutive measurement is  $3.2 \cdot 10^{-5}$  m. Therefore 95% confidence bound of a measured value is  $\pm 6.4 \cdot 10^{-5}$  m.

Manually adjusting the height of the lasers induces an error of approximately 0.1 mm. This error only applies when determining the total water depth as each device is fixed over the duration of a simulation.

Another source of errors is the deformation of the measurement carriage and the rail the carriage is on, with the magnitude of deformations in the same range as the measurements themselves. Figure 20 shows the variation in elevation of the carriage in transverse direction and of the variation in measured elevation in streamwise direction, with a mean deviation over the transverse direction of  $5.5 \cdot 10^{-4}$  m and a mean deviation in the streamwise direction of  $3.4 \cdot 10^{-4}$  m. The uncertainty in the transverse direction gives an extra uncertainty of the absolute water levels. The deviation in streamwise direction were consistent and predictable and have been corrected for in the determination of the water levels.

### 3.3 Boundary conditions and measurement locations

The main part of the research consists of physical modelling. The geometry is described in section 3.1. The research questions determine what data is required and determine the location of the measurement points. In this chapter the measurement strategy is explained. First the different hydraulic conditions to be considered will be determined. After that the different measurements for the situation without groynes and with groynes will be explained. An overview of each simulations is given in chapter 0.

#### 3.3.1 Hydraulic conditions

The water depth at which all measurements will be done are: 0.18 m, 0.24 m, 0.3 m, 0.35 m, 0.4 m as shown in Figure 21. The selection of water levels include one situation with emerged groynes as a benchmark for the numerical groyne simulation, one with submerged groynes and an inactive floodplain and three with an active floodplain, in accordance with preliminary numerical testing (Chavarrías, Platzek, & Yossef, 2019). The different submergence levels allows to investigate the influence of the submergence level on the groyne resistance.

The discharges that are considered for each experiment are summarized in Table 1. For each experiment one discharge is considered which gives a Froude number in the main channel of approximately 0.12, which represents the conditions in the Waal river according to the *Rijntakken* model (Chavarrías, Busnelli, & Sloff, 2020). Furthermore one discharge higher and one discharge lower will be considered for each water level with submerged groynes. The different discharges allows to investigate the influence of the hydraulic conditions on the groyne resistance, which in turn allows the separation of the influence of hydraulic conditions (flow velocity) and the submergence level.



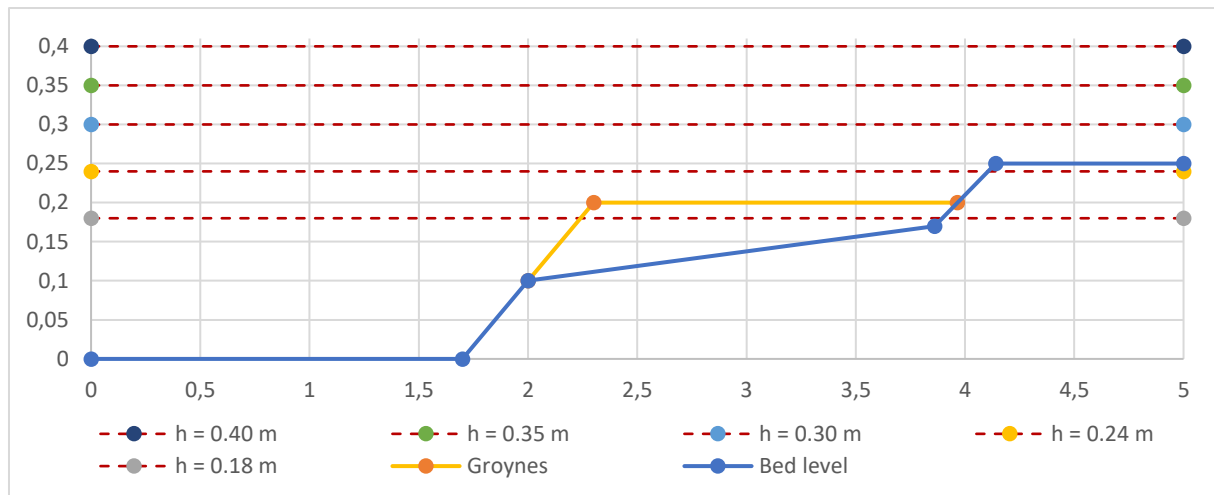


Figure 21; Cross section of flume with the considered water depths

Table 1; Discharges considered for each water level

Water depth main channel $d$ [m]	Total discharge $Q$ [ $m^3/s$ ]		
<b>0.40</b>	0.174	0.232	0.284
<b>0.35</b>	0.174	0.224	0.255
<b>0.30</b>	0.097	0.174	0.224
<b>0.24</b>	0.056	0.078	0.111
<b>0.18</b>	0.056	—	—

### 3.3.2 Measurement points in a cross section

In general the flow only varies slowly in the direction of the flow, with a large variation of flow characteristic in the transverse direction going from main channel to a mixing layer to a groyne field, to a mixing layer to a floodplain. Therefore the measurement points are close together in one cross section, while more spaced out in the direction of the flow. This also suits the setup well with the possibility to measure 5 velocity points and 3 elevation point at the same time in one cross section. The position of velocity points measured is chosen such that a good spread over the vertical is measured, while also ensuring time efficient measurement. In the main channel there will be a largely developed logarithmic flow profile. Therefore the velocity points in the main channel at least measure at 20%, 40% and 80% from the bottom to have an extra estimation method for determining the mean flow velocity in the vertical. Furthermore the velocity points are at least 3 cm below the water surface as the measuring probe needs to be fully submerged by a margin to keep the background noise on the signal constant. Next the velocity points are always at least 3 cm above the bed level, as otherwise the flow get squeezed between the probe and the bed to the point where the measurement device influences the flow too much to consider measurements reliable. The water level measurements are spread out such that the different areas in the flume are all measured. With that in mind the measurement point over one cross section are shown in Figure 44 to Figure 48 in for the different water levels.

### 3.3.3 Measurement series without groynes

Experiments with an without groynes are done. The experiments without groynes allow estimation of bed shear stress parameters and possibly parameters to represent the effect of lateral shear and secondary circulations. With the measured flow profiles the analysis of the bed roughness as executed by Besseling (2021) can be expanded to different water levels. For the measurements without groynes only few cross sections need to be considered. One cross section at the up- and downstream boundary condition is required, as well as some cross sections in the middle, where the flow is more uniform, for the comparison with the situation with groynes. The spacing of the measurement points is shown in Figure 50 to Figure 52 in Appendix B for the different water levels.

### 3.3.4 Measurement series with groynes

For the simulations with groynes more flow sections are considered of interest. Firstly up- and downstream of every groyne a cross section is measured, as it includes the measurement of the boundary conditions and their influence on the model, where a large effect of the first two groynes on the flow is expected in the region where the flow is not adapted to the groynes (Yossef, 2017). The cross section at each groyne are taken 0.5 m upstream and 1 m downstream of each groyne, at the locations of respectively largest setup and flow expansion (Ambagts, 2019). At the third and fourth groyne extra measurements are done for the simulations with submerged groynes, as the flow is expected to be adapted at those locations. Here extra cross section are measured for the determination of the discharge distributions on and flow velocities on top of the groynes, the flow over groynes, and the momentum exchange in the mixing layer. For the determination of the bypassing discharge one cross section at the third and fourth groyne is measured, with the measurement point in the cross sections as shown in Figure 49 in Appendix B for the water levels of 40 cm. For the determination of energy loss over the groynes an additional cross section 0.5 m downstream of the third and fourth groyne is measured. For the determination of the momentum exchange in the mixing layer over the groyne field length two extra section in the third and fourth groyne field are measured. The resulting spacing of the measurement points is shown in Figure 23. For every simulation also one PTV measurement is done for the determination of the surface velocities.

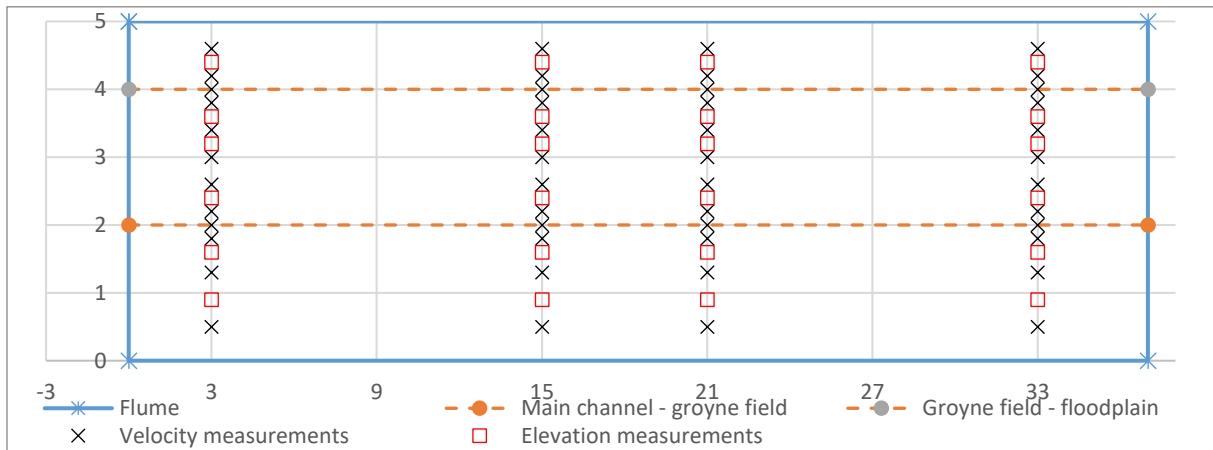


Figure 22; Location the measurement points of the cross sections for the simulations without groynes with water depths of 30, 35 and 40 cm. The axes are in [m].

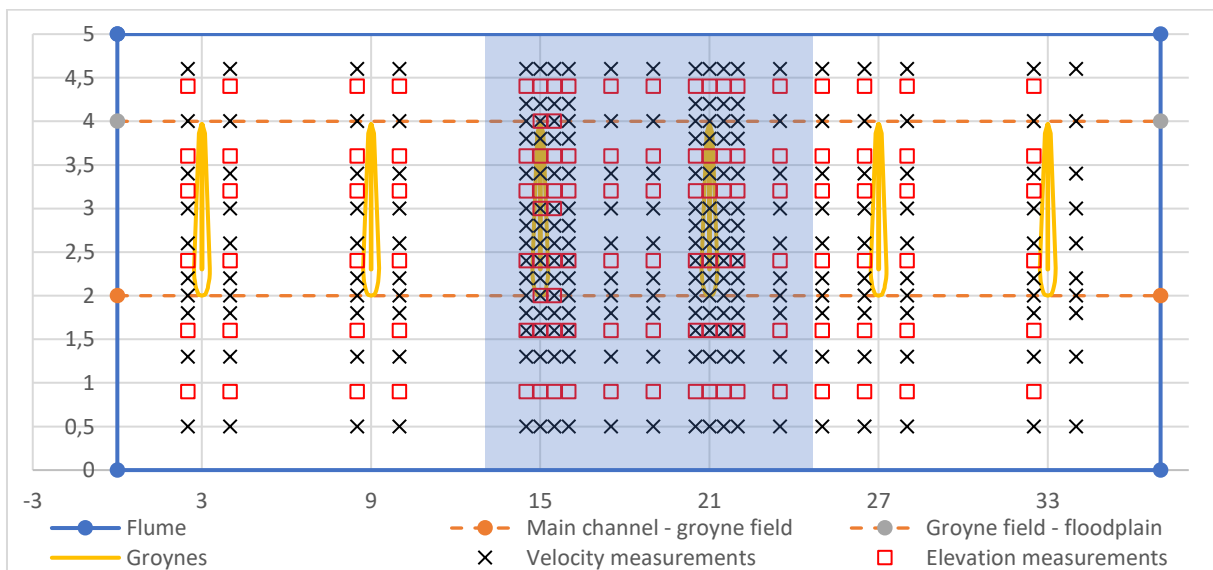


Figure 23; Location the measurement points of the cross sections for the simulations with groynes with water depths of 30, 35 and 40 cm. The axes are in [m]. In blue the area measured with the PTV.



### 3.3.5 Summary simulations

Table 2 shows every simulation done. The simulations are numbered as well for convenience of referencing later this thesis. For each simulation the water level, the discharge, the Froude number in the main channel and whether it is with groynes installed is shown.

*Table 2; Summary of every simulation*

SIMULATION	WATER LEVEL [m]	DISCHARGE [m <sup>3</sup> /s]	FROUDE NUMBER IN MAIN CHANNEL [-]	WATER LEVEL SLOPE [-]	GROYNES
E01	0.39	0.174 ± 0.004	0.07	3.6 · 10 <sup>-5</sup>	
E02	0.39	0.232 ± 0.005	0.10	7.0 · 10 <sup>-5</sup>	
E03	0.39	0.284 ± 0.009	0.11	1.01 · 10 <sup>-4</sup>	
E04	0.35	0.174 ± 0.004	0.09	6.9 · 10 <sup>-5</sup>	
E05	0.35	0.224 ± 0.009	0.11	9.6 · 10 <sup>-5</sup>	
E06	0.35	0.255 ± 0.012	0.15	1.26 · 10 <sup>-4</sup>	
E07	0.30	0.097 ± 0.001	0.07	4.6 · 10 <sup>-5</sup>	
E08	0.31	0.174 ± 0.004	0.13	1.26 · 10 <sup>-4</sup>	
E09	0.31	0.224 ± 0.009	0.16	1.86 · 10 <sup>-4</sup>	
E10	0.25	0.056 ± 0.002	0.07	4.2 · 10 <sup>-5</sup>	
E11	0.25	0.078 ± 0.001	0.09	6.9 · 10 <sup>-5</sup>	
E12	0.25	0.111 ± 0.002	0.13	1.17 · 10 <sup>-4</sup>	
E13	0.21	0.056 ± 0.002	0.10	1.00 · 10 <sup>-4</sup>	
G01	0.38	0.174 ± 0.004	0.07	5.2 · 10 <sup>-5</sup>	Yes
G02	0.38	0.255 ± 0.012	0.11	8.8 · 10 <sup>-5</sup>	Yes
G03	0.38	0.284 ± 0.009	0.12	1.28 · 10 <sup>-4</sup>	Yes

### 3.4 Data processing

Velocities are measured for 5 minutes for each point. As our interest lies in the mean quantities and their statistical properties these quantities are converted. This chapter gives an overview on the methods used for that.

Mean flow velocities in each point are determined as:

$$\bar{u} = \frac{1}{N} \sum_{i=1}^N u_i \quad (41)$$

The different moments of the flow velocity are determined as:

$$\overline{(u'_i)^n} = \frac{1}{N} \sum_{i=1}^N (u'_i)^n \quad (42)$$

For the EMS the  $u_i$  is the measured time-signal, converted to velocities, at one specific point. For the PTV  $u_i$  are the velocity of the particles that fall within cell of  $0.2 \times 0.2$  m, the chosen mapping resolution.

The depth average velocity is determined as the trapezoidal mean velocity of the measured flow velocities, extrapolating the lowest and highest measured velocity points to the bed respectively surface:

$$U = \frac{1}{d} \sum_{i=0}^d \Delta d \cdot \frac{1}{2} (\bar{u}_i + \bar{u}_{i+1}) \quad (43)$$

The discharge for each experiment is controlled by a pump that can be adjusted in power. The measurement of the discharge through the inflow pipe prove unreliable. The discharge through the domain is determined by the integration over the width of the depth average velocity doing a midpoint integration on the velocity points:

$$Q = \sum_{i=0}^B U_i \cdot d_i \cdot \left( y_{i+\frac{1}{2}} - y_{i-\frac{1}{2}} \right) \quad (44)$$

There is an uncertainty in the obtained discharges, related to the lateral slope of the bed and the limited number of measurement points in a transect. This uncertainty is showed in chapter 3.3.5.

For some of the signals the auto-correlation signal is determined as:

$$R_{vv}(\tau) = \frac{\langle v(t_0) \cdot v(t_0 + \tau) \rangle}{\sqrt{\langle v^2(t_0) \rangle \cdot \langle v^2(t_0 + \tau) \rangle}} \quad (45)$$

The auto-correlation is only determined for lateral velocities, which represent periodic flow only without an effect of advection of flow. The brackets denote averaging in time.

## 4 Results

### 4.1 Visual observation

The discharge distribution at the inflow does not match that of the downstream discharge distribution. This effect is more pronounced for the higher water levels. The development of a stable discharge distribution between the channels is analysed in Appendix D. There are some other boundary effects in the flume. First of all the inflow is quite wild, which introduces waves at the inflow. Not all of these wave are damped by the wave damper between  $x = 1$  and  $x = 2$  m. At the downstream end of the flume there is a transition to the different flow area with the pump and the overflow weir. This region extends for some cases up to one meter into the modelling area.

Flow processes that could be verified by visual observation are eddies shedding from the groyne tip and the vertical separation of the flow downstream of the groyne.

#### Mixing layer

No large eddies are observed in the mixing layers by eye, nor by injecting dye in the mixing layer. This indicated that either the lateral shear is low so that few eddies are formed, which is the case for low velocity differences, and/or that the large eddies effectively dissipate into smaller eddies, which indicates that the eddies are not bounded by the shallowness of the flume.

#### Eddies from the groyne tip

Eddies shedding from the groyne are observed by eye. This process was fairly regular every few seconds. This indicated a large shear at the groyne tip and corresponds to observations from Yossef (2005). A sketch of the observation is shown in Figure 24.

#### Separation zone downstream of groyne

An attempt was made to inject dye at the bed just downstream of the groyne. This prove very difficult with the available equipment at the lab, and it was only possible to get dye just below the groyne crest. For that case the dye stayed in place. Clearly the separation zone was a stagnant one, with parts of the dye remaining in place for a few minutes before it was no longer distinguishable. Some of the dye re-entered the flow and was advected downstream, most of the dye dispersed in the wake of the groyne.

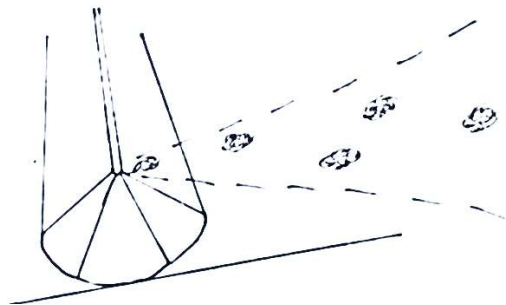


Figure 24; Sketch of vortex shedding from the groyne tip

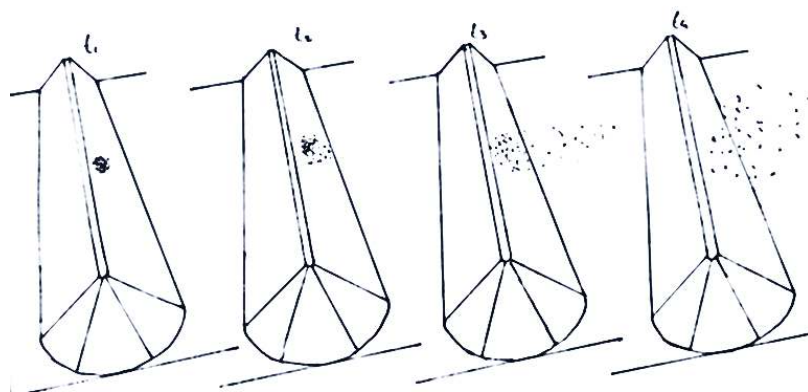


Figure 25; Sketch of spread of dye in the water injected just behind the groyne crest

## 4.2 Water level slopes and groyne head loss

This paragraph elaborates on the observed water levels and head losses over the groynes, shown in Figure 26 and Figure 27. For the plots in Figure 26 the measured water levels are normalized per streamwise section to match each other either at  $x = 32.5$  m. The water level slopes from the measurements without groynes are included as a comparison.

The water level measurements from the cases with groynes confirm a pattern of flow contraction and expansion over the groyne, visible at the water levels measured at  $y = 2$  m at  $x = 15$  m and  $x = 21$  m. The contraction is an order of magnitude larger than the water level change over one groyne. The water level change over one groyne is only a few times larger than the resolution of the measurement equipment and only just measurable. The groynes add  $5.8 \cdot 10^{-4}$  m,  $6.5 \cdot 10^{-4}$  m and  $9.7 \cdot 10^{-4}$  m of set up for respectively case G01, G02 and G03, compared to the same simulation without groynes, case E01, E02 and E03 and give an increased water level slope of approximately 25%.

Figure 27 shows the head loss over each groyne in each case from the groyne tip a  $y = 2$  m to the end of the groyne at  $y = 4$  m. At the groyne tip there is not much of a head loss, with an increase of water head from upstream to downstream of the groyne at many observed points at the groyne tip. This indicates a difference in flow processes at the groyne tip and groyne main body. At the main body of the groyne there is a larger head loss for larger submergence levels, as the channel is shallower near the floodplains. Here the groyne is less of an obstacle, which seems to be reflected in the low head loss at  $y = 3.8$  m.

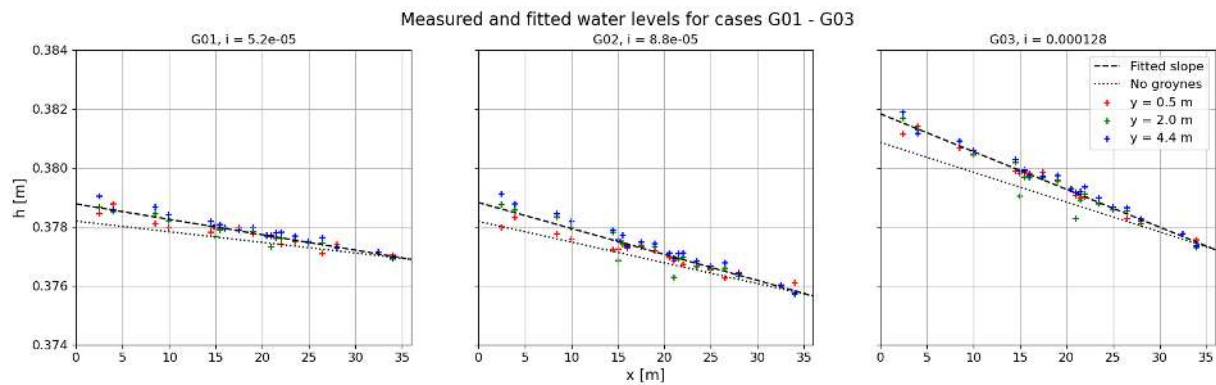


Figure 26; Measured water levels for the cases G01 – G03

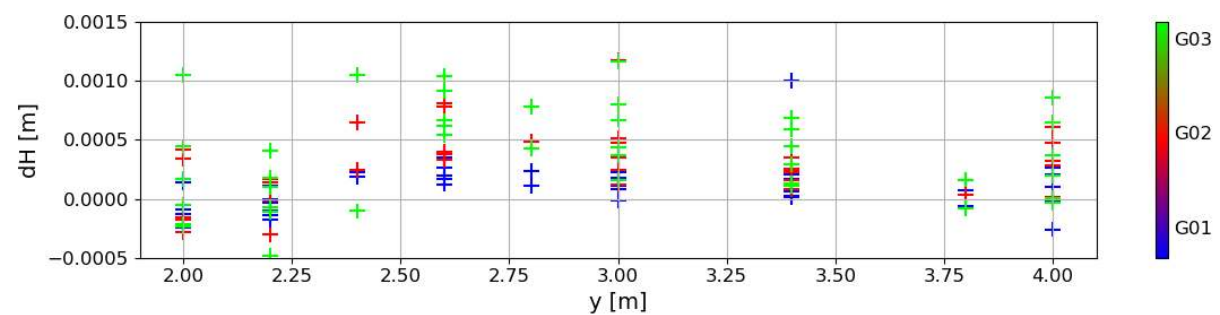


Figure 27; Measured head loss over the groyne from 0.5 m upstream to 1 m downstream of groyne crest

### 4.3 Water surface flow

Figure 28 shows the surface velocity maps. The velocity map with the streamwise velocities also include the velocity vectors. Note that the velocity scales for each heatmap is different for the streamwise velocity, to visualize the difference in flow velocity within a case. There is a gradual change of streamwise velocities in the streamwise direction. The discharge distribution between the channels is not stable in the chosen area of surface measurements. The adaptation of the flow is discussed in Appendix D. Figure 57 in Appendix D shows that the discharge distribution is stable from the fourth groyne onward. The observed global changes of streamwise velocity are explained therefor be the adaptation of the flow to the flume.

#### Mean flow

For each case there is a region of low flow between  $y = 2.0$  m and  $y = 3.0$  m, deviating from standard expected patterns for the flow velocity. This region of low flow does not equal that one observed for the case without groynes, but could have the same origin in the secondary circulations. The region of low flow is expected to be due to the groyne. There are two main explanations for this flow pattern. The first explanation is that the low flow is an effect of the interaction of multiple flow patterns, which create some three dimensional flow patterns that could not be observed surface profiles and EMS. The second explanation is that the water is driven out of the groyne field by the flow around the groyne, and that the missing volume is compensated for by flow out a region of low flow near the bed. This seems the case as at the surface the transverse velocities are larger outwards in to the main channel upstream of the groyne, than inward downstream of the groyne into the groyne field. This would lead to a spiralling flow pattern as commonly observed downstream over obstacles (Gao, Agarwal, & Katz, 2021).

#### Flow over and around groyne

The flow accelerates over the groyne, indicating flow contraction. Largest flow velocities are observed approximately 0.2 m downstream of the groyne crest. This implies that there is an additional contraction of flow downstream of the groyne crest. The flow resembles flow over a short crested weir, with the point of maximum contraction, with largest flow velocities, downstream of the weir.

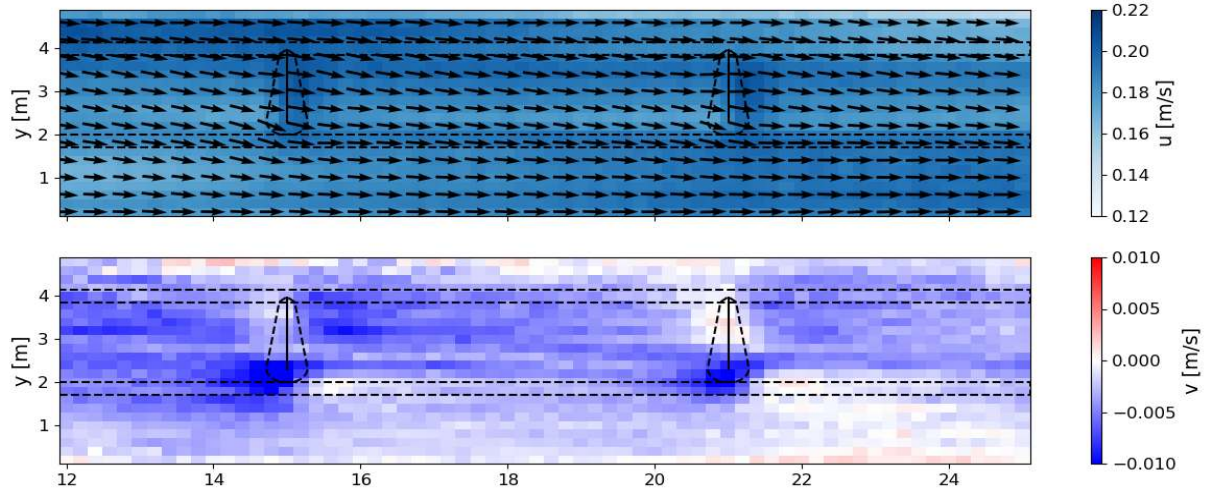
The flow decelerated downstream of this point, indicating flow expansion and weir like expansion losses. The deceleration region as visible from the surface velocities is from 0.3 – 0.7 m downstream of the groyne. The acceleration and deceleration together indicate a weir-like head loss due to contraction and expansion. This corresponds to the observed change of water level over the groyne.

There is a flow around the groyne. There is a split at  $y \approx 3$  m in where the transverse velocities upstream of the groyne go from negative to positive. This indicates that upstream of the groyne water is directed out of the groyne field. The water is pushed into the floodplain from  $y = 3$  m to  $y = 4$  m and water is pushed into the main channel at the groyne tip. At the groyne tip the largest transverse velocities are found. These transverse velocities are not (fully) countered by surface flow into the groyne field downstream of the groyne. The transverse velocity indicates flow attraction by the groyne tip, such as comparable to flow over a compound weir. From continuity we expect that there is flow into the groyne field however deeper in the vertical, which would together form a flow spiral. There is a surface flow back into the groyne field downstream of the groynes from the floodplain.

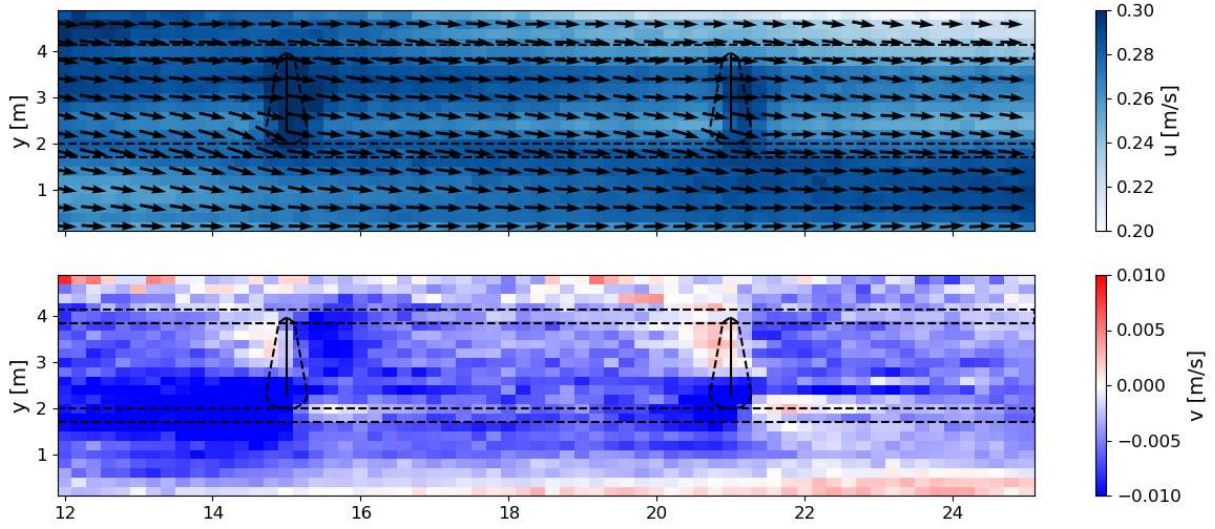
The transverse velocities are not limited to the groyne tip however and indicate something unexpected, based on the literature available of flow over groynes. That is that not all of the water in the groyne field flows over the groyne, but rather through the floodplain and main channel. This flow then reverts back into the groyne field downstream of the groyne. This flow is a comparable to flow around a vertical obstruction, with horizontal contraction and expansion around the obstacle. The observation of this lateral flow indicates that there is vertical and horizontal contraction and expansion of flow over and around the groynes, and that this lateral flow is not restricted to the groyne tip.



Surface velocity maps between  $x = 12$  and  $x = 25$  m, case G01



Surface velocity maps between  $x = 12$  and  $x = 25$  m, case G02



Surface velocity maps between  $x = 12$  and  $x = 25$  m, case G03

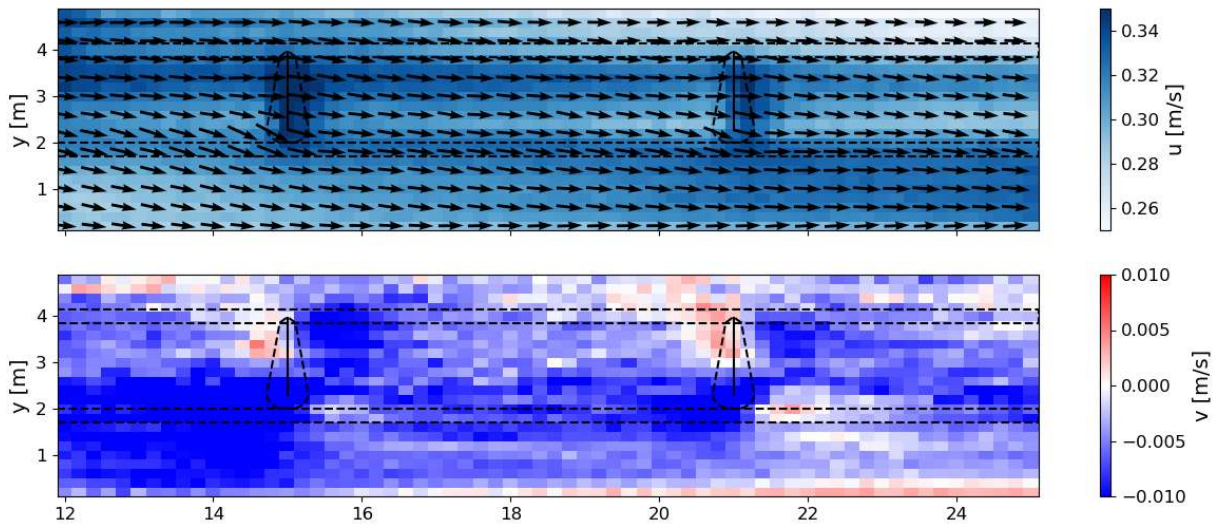


Figure 28; Surface velocity and turbulence map for cases G01 – G03. The area captured by the PTV is from  $x = 12$  to  $x = 25$  m. The dashed lines indicate the groynes and the different parts of the channel.

#### 4.4 Flow observations around groyne

Appendix C shows the vertical flow profiles and turbulent fluctuations from just upstream of the fourth groyne to far downstream ( $x = 20.5 - 25$  m). From these vertical flow profiles and their relative turbulent fluctuations we can learn multiple things. A visualization of the flow profiles and turbulent fluctuations is shown in Figure 29. The flow velocities in Figure 29 are normalized on the average flow velocity in each experiment ( $Q/A$ ) so that the results from the three simulation are comparable. Figure 30 shows the ratio of discharge at the groyne crest compared to the discharge upstream and downstream of the groyne.

##### Flow expansion

All vertical velocity signals at  $x = 21.5$  m, at the groyne, show a large vertical gradient of the streamwise velocity, indicating a mixing layer. All vertical velocity signals at  $x = 22$  m, at the groyne, do not show a mixing layer, and do not correspond to the upstream and downstream fully developed boundary flow profiles. This corresponds to the gradual formation of a new boundary layer downstream of a backward facing step. The gradient of the streamwise velocity component near the bottom at  $x = 21.5$  m, which indicate a mixing layer between free flow and a vertical separation zone decreases for smaller groyne blockage ratios, where the groyne height is smaller. This indicates that there is a less pronounced mixing layer deeper into the groyne field, for higher values of  $y$ . As for smaller blockage ratios the length of the vertical separation is smaller, this effect is expected. The turbulent fluctuation 0.5 m downstream of the groyne show a large peak which corresponds to a large shear in a vertical profile with a mixing layer between a free flow and a recirculation cell before flow reattachment. The relative turbulence 1 m downstream of the groyne no longer has such a peak at the bottom, indicating much less of a mixing layer at all transact at the groyne main body. The turbulent profile does not represent that of a fully developed boundary flow, as the flow profile upstream and far downstream of the groyne. At 1 m downstream of the groyne the flow is either reattached, or close to reattachment therefor. The new boundary flow is fully developed 2.5 m downstream of the groyne at  $x = 23.5$  at all locations. Comparing the vertical flow profiles with those measure by Nakagawa and Nezu (1986) for a backward facing step one can see remarkable similarities. The reattachment length is approximately 5 step height downstream of the point of maximum contraction, which lies approximately 0.2 m downstream of the groyne crest. The comparability of the observed backwards facing step to the measurement of Nakagawa and Nezu (1986) counter the notion of Jongeling et al. (Jongeling, Goede, & Keser, 2012) that the perceived reduced head loss over groynes compared to weirs is due to a reduced under pressure in the mixing layer, as that would result in a longer mixing layer. This is no falsification of the notion, but does give an argument against it.

##### Flow at the groyne tip

At the groyne tip there is a dip in the flow velocity at the surface and an increased flow velocity lower in the water. The vertical flow profile is possibly the result of how water flows laterally around the groyne, and indicates a three dimensional flow at the groyne tip. At the groyne tip at  $y = 2.2$  m there is no sign of vertical separation combined with flow expansion in the turbulent fluctuations. There is a slight increased gradient in the streamwise flow velocities near the bed at  $y = 2.2$  m. This indicates that at the groyne tip there is no or barely any flow expansion that would lead to energy losses as a weir head loss.

##### Flow in the main channel and floodplain

Turbulent fluctuations show boundary layer flow in the main channel and the mixing layer, including at the groyne tip at  $y = 2.2$  m and in the floodplain from  $y = 4$  m onward. The flow expansion is therefor limited to the main body of the groyne. In the floodplain and main channel little changes in the vertical flow profiles. The flow remains a well defined boundary layer flow.

##### Lateral flow

Figure 30 shows that not all of the discharge upstream of the groyne passes over the groyne, and that equivalently there is more discharge downstream of the groyne than on top of the groyne. From this figure we can conclude that a part of the flow does indeed does not flow over, but around the groyne. This means that part of the upstream discharge in the groyne field flows around the groyne in the floodplain and in the main channel and flows back into the groyne field downstream of the groyne. This horizontal contraction and expansion of flow does not seem to flow over the groyne tip, but rather flow concentrate in the main channel. The groyne is a horizontal constriction in this regards. At the floodplain side the bypassing discharge is concentrated in the mixing layer between the groyne field and the main

channel at  $y = 4$  m. At this location there is a consistent increase in discharge at the groyne crest. At the groyne tip at  $y = 2.2$  m there is no increased discharge on top of the groyne, which contradicts the idea that there is more flow at the groyne tip as a compound weir. The bypassing discharge is mainly concentrated at  $y = 2$  m, at the feet of the groyne tip and can also be found deeper into the main channel at  $y = 1.6$  m and  $y = 1.8$  m. Integrating the discharges over the width of the main body of the groyne, summarized in Table 3, shows that between 3-6% of the flow in the groyne field horizontally contracts and expands over the groyne. The bypassing is larger when only comparing the discharge on top of the groyne to the upstream discharge in the groyne field at approximately 5% for each case and each groyne, compared to only a difference of 3% between the discharge on top of the groyne and downstream of the groyne. This can be explained as an effect of the ongoing redistribution of discharge which stabilizes only at the fourth groyne and is therefore an effect of the flow not being fully adapted to the geometry of the flume at the considered groynes.

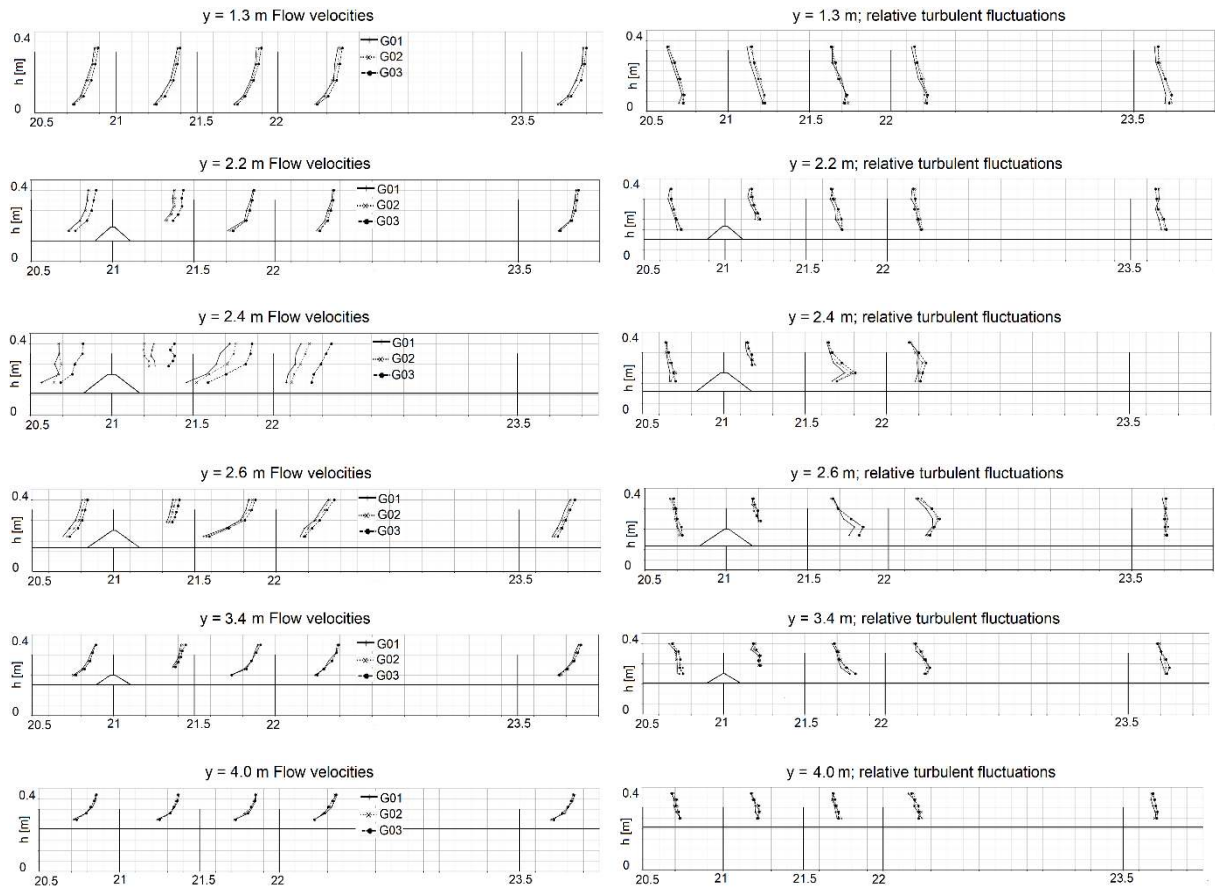


Figure 29; Development of flow velocities and turbulent fluctuations relative to the average flow velocity ( $Q/A$ ) for case G01 – G03. The transverse location is from top to bottom the main channel to the floodplain.

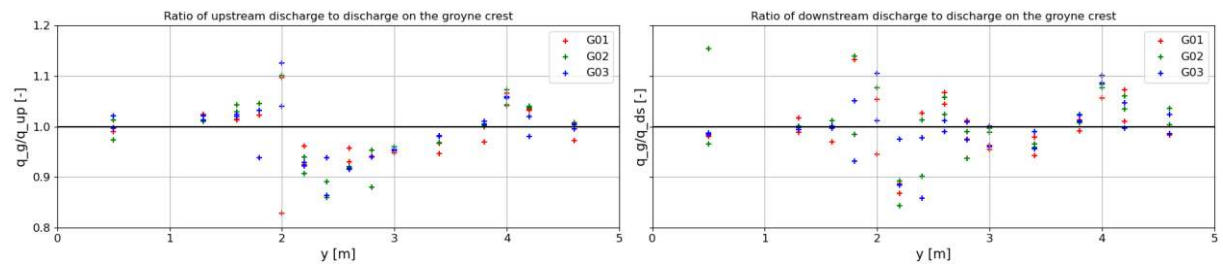


Figure 30; Ratio of discharge on top of the groyne crest to a: the upstream discharge; b: the downstream discharge



Table 3; integration of discharge from  $y = 2.3$  m to  $y = 3.9$  m upstream (up) of the groyne, on the groyne crest (g) and downstream (ds) of the groyne

Simulation	Groyne	$Q_{up} \left[ \frac{m^3}{s} \right]$	$Q_g \left[ \frac{m^3}{s} \right]$	$Q_{ds} \left[ \frac{m^3}{s} \right]$	$\frac{(Q_{up} - Q_g)}{Q_{up}} [-]$	$\frac{(Q_{ds} - Q_g)}{Q_{ds}} [-]$
G01	3	0.0534	0.0511	0.0528	0.044	0.032
G01	4	0.0546	0.0519	0.0534	0.048	0.028
G02	3	0.0793	0.0755	0.0778	0.048	0.029
G02	4	0.0752	0.0710	0.0732	0.056	0.030
G03	3	0.0938	0.0889	0.0915	0.052	0.028
G03	4	0.0917	0.0879	0.0901	0.042	0.025

#### 4.5 Flow dynamics away from the groyne

Far away from the groyne flow the boundary flow will be established again, so that it the flow can be assessed in a depth averaged sense. The depth average velocity profile in Figure 31 correspond well to the observed surface velocity profiles. The general pattern of high flow velocities in the main channel, followed by a dip in the depth average velocity at the groyne tip and a relatively high mean velocity deeper into the groyne field is confirmed. Compared to the situation without groynes there is no large difference between the discharge distributions over the channels. The flow velocity in the case with groynes is a few percentages larger compared to the case without groynes. This is as groynes add a friction to the groyne field, which results in a redistribution of discharge from the groyne field to the main channel, such that in all channels the momentum balance holds.

It can also be seen in Figure 32 and Figure 33 that the turbulent fluctuations partly increase as a function of shallowness, related to bed shear, and partly increase at the groyne tip. Together with the dip in the depth average velocity at the groyne tip there is a peak in the relative turbulence from  $y = 2.2$  m to  $y = 3.0$  m. This however indicates more the effect of low flow velocities, instead of indicating lateral shear.

Figure 34 shows the autocorrelation signal in the flume at  $x = 23.5$  m, halfway between groynes. We expect to observe large turbulent fluctuations with timescales of tens of seconds, as observed by Yossef (2005), at every location in the vertical. No large scale fluctuations were observed. The graphed time in the figure is therefore only 4 seconds, in order to see the variations in the autocorrelation function. Comparable with the cases E01 – E03 in Figure 62 there are no large differences in the autocorrelation functions over the transverse that indicate large eddies in the shear layers. We expect larger eddies in the groyne field than in the main channel due to lateral shear. This seems not the case and remains an unexplained feature. The observation does correspond however to visual observations by eye and with dye, where no large eddies were observed in the flow.

The lack of lateral shear and the generally low differences in flow velocities indicate there is few dissipation in the horizontal mixing layers between the channels and that dissipation of energy due to exchange processes between the channels is dominated by the flow bypassing around the groyne where there is an exchange of mass back and forth between the channels at the groynes.

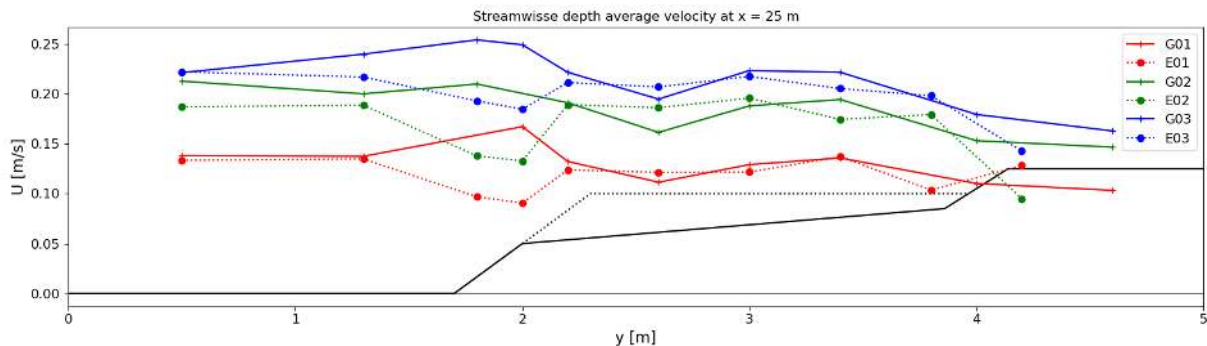


Figure 31; Depth average flow velocity at  $x = 25$  m for cases G01 – G03 and E01 – E03

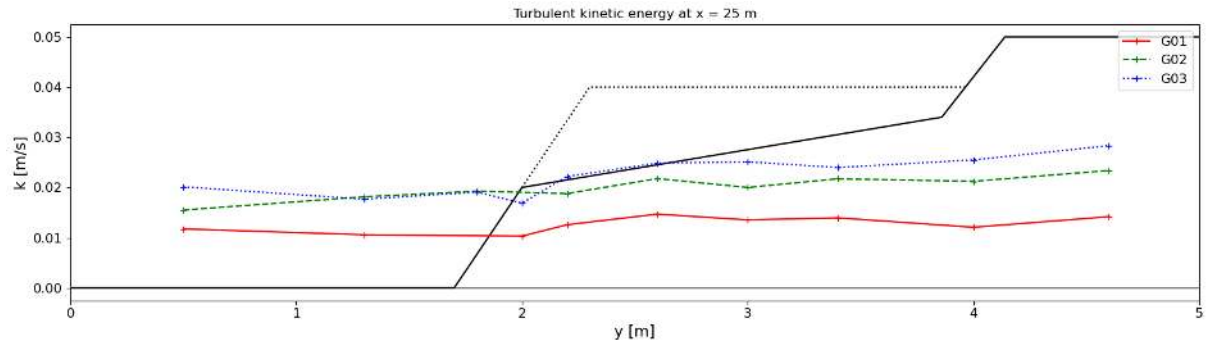


Figure 32; Variation of mean flow velocity at  $x = 25$  m for cases G01 – G03

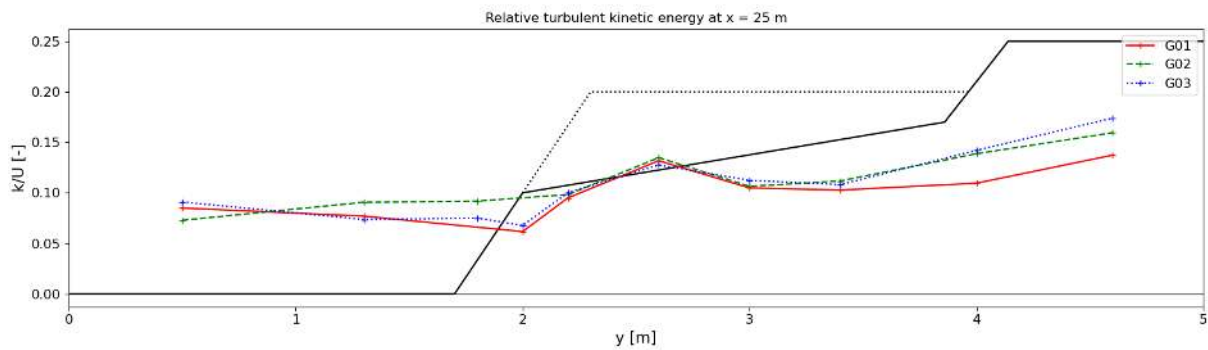


Figure 33; Relative turbulence at  $x = 25$  m for cases G01 – G03

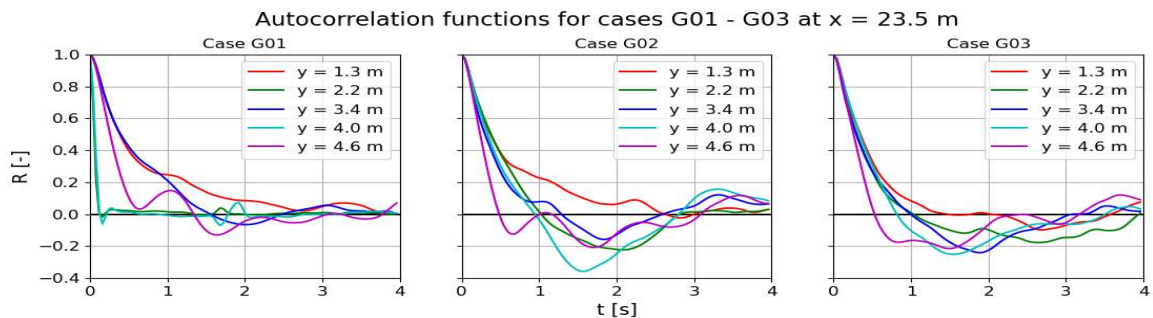


Figure 34; Autocorrelation of transverse velocity signals at  $x = 23.5$  m for the cases G01 - G03 at different places over one transect

## 4.6 Summary

The addition of groyne to the flume resulted in water level slopes that were on average 25% higher than without groynes.

From the observation of flow in the physical model expansion of flow downstream of the groyne was observed. The expanded flow seemed to have the same characteristics as flow over a backwards facing step. Expansion of flow is not observed at the groyne tip. At the groyne tip there is no observed head loss also measured from 0.5 m upstream of the groyne to 1 m downstream of the groyne.

There is a region of low flow from  $y = 2$  m to  $y = 3$  m, which indicate large scale three-dimensional flow. For the correct reproduction of this flow it might be important to measure the flow with a dense measurement grid so that the effect of this region of low flow can be quantified.

Vortex shedding is observed from the groyne tip. Large turbulent fluctuations could not be measured however. The small gradients of streamwise velocity over the transverse indicate a small influence of lateral shear on the flow.

Not all of the flow in the groyne field flows over the groynes. A part of the flow flows around the groyne into the main channel and floodplain, upstream of the groyne. Downstream of the groyne this motion is reverted, and flow flows back into the groyne field from the main channel and floodplain. A part of the water therefor horizontally contracts and expands around the groyne, which makes the groyne a horizontal constriction as well as a vertical constriction. In our simulations 3-5% of the flow bypassed the groyne independent for all simulations, with no visible dependency on the flow velocity. This process seemed dominant over any possible flow attraction of the groyne tip. The bypassing flow was concentrated in the sides of the groyne at  $y = 1.8 - 2$  m at the main channel and  $y = 4$  m at the floodplain. At those locations there is an exchange of mass between the channels.

## 5 Discussion

The simulations showed the increased channel resistance due to groynes. An Important observation includes the head loss over a groyne, which indicate some weir like loss. It still has to be determined how much the expansion over groynes represent weir like losses. There are also indications of three-dimensional flow at the groyne tip, which need further investigation. A last point of attention is the horizontal flow around the groyne, as quantifying the effect of it might be difficult.

### 5.1 Weir-like expansion over groyne

With the measured water level slopes in Figure 26 and the measured head loss over each groyne in Figure 27 it is possible to assess the weir like behaviour of groynes. Downstream of the groyne there is a distinct pattern of flow separation and expansion, which indicate head losses. These head losses should be predictable as Carnot losses (equation (22)). With the Carnot losses derived from the conservation of momentum on flow expansion Figure 35a show that indeed the momentum is conserved from the groyne crests to downstream of the groynes. The measured head losses over the groyne measured from 0.5 m upstream of the groyne to 1 m downstream of the groyne can only partly be explained as a Carnot loss, as shown in Figure 35b. There is a clear trend in the measured Carnot losses for  $y = 2.4$  m to  $y = 3.4$  m, but the Carnot losses only predict between 30% and 40% of the observed head loss. Clearly other processes such as the bed shear stress can't be neglected even over a relatively small distance. This raises a question why the observed water level slope is much larger than can be measured as a Carnot loss, when the flow over the groyne clearly shows vertical flow separation and expansion, which should give large Carnot head losses.

Figure 35c,d show the empirical weir friction factor (equation (38)) which can be used to calibrate weir formula on for the modelling of flow over groynes. The data on which the values of  $C_d$  are determined are stored in Appendix E. The values of  $C_d$  show a large dependance on the discharge actually flowing over the groynes, which is a scaling behaviour of head loss formula (equations (35)-(37)). There is a dip in the values of  $C_d$  at  $y = 2.4$  m. This coincides with the observed region of low flow and is therefore correlates to the amount of discharge flowing over the groyne. At the groyne tip at  $y = 2.2$  m the submergence level goes to one, or is even bigger than one. The water level downstream of the groyne is larger than upstream of the groyne. This behaviour can't be modelled by Villemonte, and indicates that the groyne tip really does not behave as a weir. Which was also concluded from the lack of flow expansion at the groyne tip.

#### Weir head loss prediction

With the measured head losses and weir friction coefficients known it is interesting to see what weir and obstacle friction formula predict as a head loss over the groynes. Kruijt (2013) observed a large difference between the predicted head loss of weir formula and friction formula, with weir formula predicting very large head losses compared to friction formula. We are interested whether weir formula can predict the groyne head loss correctly, and specifically whether the Villemonte (VIL) formula can predict the head losses well. Two friction formula (Kruijt, 2013) deemed useful for groyne modelling are the formulations by Yossef (YOS) and Van Broekhoven (BRO) (equations (35) and (36)).

Figure 36 shows the predicted head losses using equations (35) - (37) compared to the observed head loss over the groyne. Figure 37 shows the predicted weir head loss over the measured Carnot loss.

The predicted head loss using friction formula is much lower than the predicted head loss using VIL, which was also observed by Kruijt (2013). The friction formula YOS predicts very little head losses. The predicted head loss is two orders of magnitudes lower than the observed Carnot loss. This is very unexpected. YOS does however have dependencies with high powers, as in YOS  $\Delta H \propto Fr^4$  and  $\Delta H \propto (h_g/d_{gf})^{3.7}$ . The here performed simulations have Froude numbers that were on the low side of those simulated by Yossef (2004), but fall within the validity range of Froude numbers. Also the groyne crest in our simulations is 5 cm lower and the water depth 5 cm higher than those modelled by Yossef. This makes that these simulations fall outside the validity range of the simulations performed by Yossef. The small blockage ratios in our simulations might be problematic for the application of YOS, where the blockage ratio contributes to the power 3.7 to the predicted head loss.

The friction formula BRO predicts a head loss equal to the observed Carnot losses for  $y = 3.4 - 3.8$  m, but underestimates the groyne expansion near the groyne tip, in the region of lower flow velocities. VIL predicts a larger head loss than the observed Carnot loss. There is however a clear correlation between VIL and the measured Carnot losses, with VIL predicting approximately twice the head loss. VIL is based on the Carnot equation. There is a large difference between the measured Carnot losses and the modelled Villemonte losses however. This can indicate that fundamentally the expansion over groynes differs from flow expansion over weirs. However, the head loss predicted by BRO is based on numerical vertical two-dimensional simulations of flow over weirs, and should therefore also give the same results as the Carnot head loss over weirs. In our model BRO gave a slight underestimation of the measured Carnot losses.

The here performed simulations fall within the validity range of BRO, while for VIL Yossef and Visser (2018) already concluded that the formula is very sensitive at high submergence levels, where for small blockage ratios the value of  $1/p$  goes to infinity very quickly.

Based on these observations it seems more likely that the implementation of blockage ratio in  $p$  in the Villemonte formula does not represent the Carnot losses well, and that another interpolation between Carnot losses and perfect weir flow might be required. This seems more likely than that there is a fundamental difference between vertical expansion of flow over groynes compared to vertical expansion over weirs. At this moment only simulations with high water levels have been done. Simulations with lower water levels could give a definite answer on whether there is a fundamental difference between vertical expansion over groynes and vertical expansion over weirs.

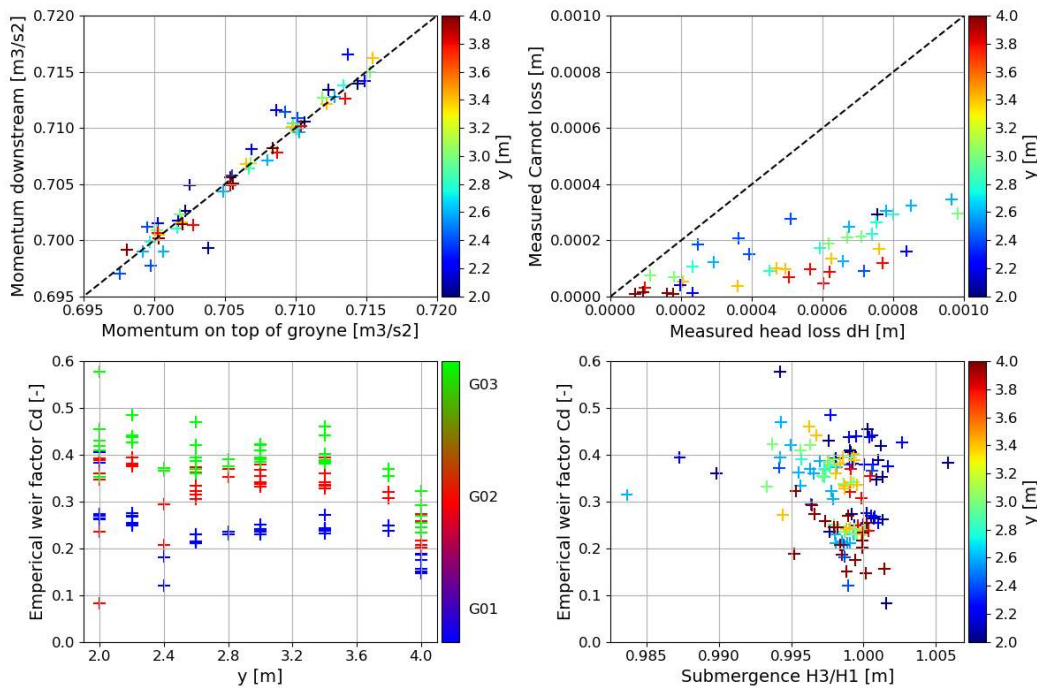


Figure 35; visualization of weir-like expansion over groynes. The dashed line is means a perfect agreement. a: the momentum downstream of the groynes against the momentum on top of the groynes; b: the measured Carnot losses over the groynes against the measured head loss over the groyne; c: empirical weir coefficients over the transverse for the different simulations; d: empirical weir coefficients against the submergence of the groynes



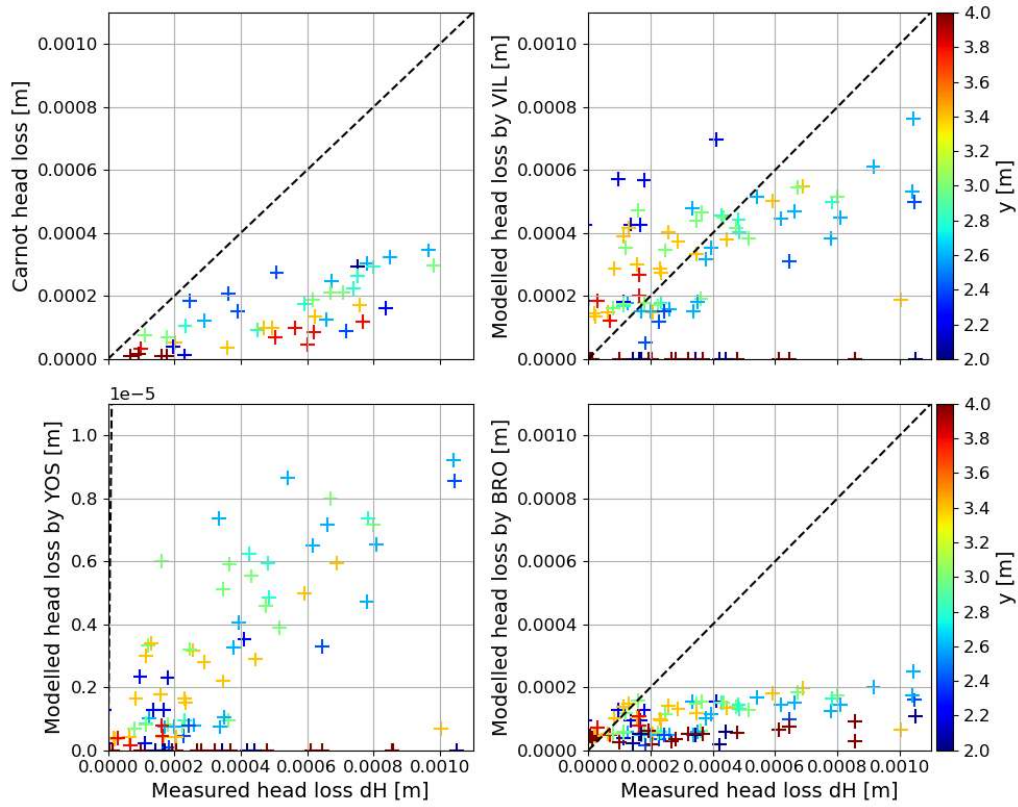


Figure 36; Measured head loss from 0.5 m upstream of groyne to 1 m downstream of groyne, compared to the measured Carnot losses and the predicted head loss using VIL, YOS and BRO

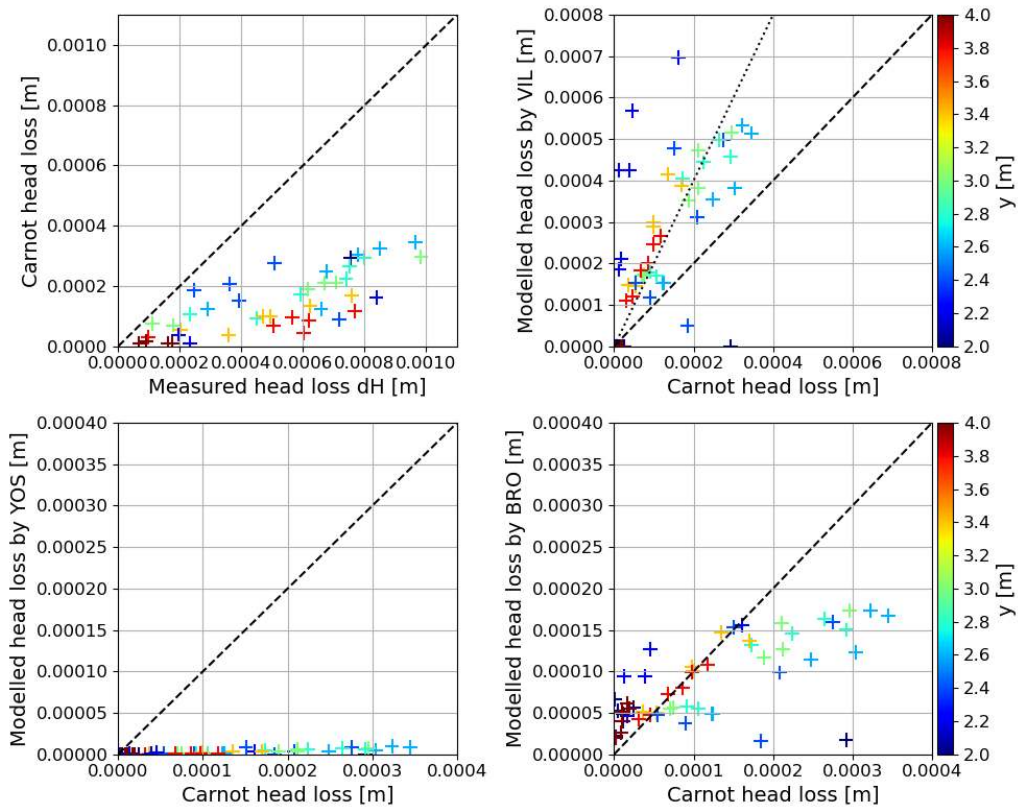


Figure 37; Measured head loss from 0.5 m upstream of groyne to 1 m downstream of groyne, compared to the measured Carnot losses and the predicted head loss using VIL, YOS and BRO including the head loss due to bed shear stress

## 5.2 Three-dimensional flow

From  $y = 2 - 3$  m there is a region of lower flow velocities, as visible in Figure 31. The region is from the groyne tip to halfway the groyne field. The lower flow velocities cannot be explained by a balance of the water level slope and the bed shear stress, and indicate a three-dimensional flow. The lower flow velocities at the groyne tip are also visible in the measurements of Yossef (2004), although they were not explicitly mentioned there as an interesting feature of the flow. Yossef (2004) measured among other things with higher flow velocities, for which the region of lower flow velocities was less visible. This could indicate that the flow process responsible for the low flow velocities does not scale with the flow velocities as bed shear stress does. This would correspond to the findings of Shiono and Knight (1991), who defined the effect of secondary circulation independent of the flow velocity. Figure 28 furthermore shows that the largest lateral surface velocities not related to the adaptation of the flow to the geometry are found in the region from  $y = 2 - 3$  m. At this point there is a lateral flow from the groyne field into the main channel. This flow pattern was also observed by Ambagts (2019), who argued that the lateral flow into the main channel requires a flow back into the groyne field deeper in the water column. This would mean that there would be a recirculation cell in the  $y - z$  plane from  $y = 2 - 3$  m. This would correspond to the detailed measurement and modelling of flow around one submerged groyne by Kuhnle et al. (2008). They distinguished a fully three dimensional flow pattern with flow circulations in the  $x - z$ ,  $x - y$  and  $y - z$  plane. The first (in the  $x - z$  plane) would be the standard recirculation downstream of a weir in the vertical separation zone. The second (in the  $x - y$  plane) would be comparable to the gyre downstream of an emerged groyne, but much smaller. This eddy is due to either lateral shear between the flow in the main channel and groyne field, or due to inflow of mass from the main channel into the groyne field downstream of the groyne tip.

In the here performed simulations it was not possible to assess the lateral nor vertical velocities. The first because the lateral flow velocities have magnitudes that are smaller than the zero error of the devices and it could not be guaranteed that the devices were mounted perfectly straight, so that there might be an angle between the true  $x, y$  of the flume, and the  $x, y$  in which the EMS measured. Even a small rotational error of  $3^\circ$  would mean that the measured velocities in  $x$  would be projected on the velocities measured in  $y$ , with the same order of magnitude as the expected velocities in the transverse. The vertical velocities are not measured as those cannot be measured by the used EMS.

The only transverse velocities obtained are from the PTV measurements of the surface flow, shown in Figure 28. This makes it impossible to verify any three-dimensional flow patterns in the flume. Based on observations by others, such as already discussed, it seems very likely however that there is a complex three-dimensional flow induced by the groyne tip. This would explain the transverse velocities at the surface and explain the low depth average velocities from  $y = 2 - 3$  m. The effect of this three-dimensional flow seems quite large, as it also seems to increase the depth averaged velocity at the transition between the main channel and the groyne field at  $y = 1.6 - 1.8$  m, where the largest flow velocities in the transverse are found, and seems to increase the depth averaged velocity in the groyne field from  $y = 3 - 4$  m, where the depth averaged velocities are almost equal to those in the main channel. Furthermore the low depth average velocities from  $y = 2 - 3$  m have flow velocities equal to those found in the floodplain, which either emphasize how low these velocities are, or how high the velocities are in the floodplain.

From the current measurements there is a presumption that for these experiments there is three-dimensional flow pattern induced by the groyne tip, that this flow pattern has a noticeable impact on the distribution of discharge over the transverse, and that this flow pattern has a noticeable impact on the energy dissipation induced by the groyne. For the determination of the total resistance of groynes it seems important to quantify the effect of the three dimensional flow. This could either be done by extensive measurements around one groyne, or by detailed numerical modelling. Based on the complexity of the flow the latter might prove more easy to execute.

### 5.3 Lateral flow

There is a lateral flow around the groyne, deduced from the difference in the discharge on top of the groyne and up- and downstream of the groyne, where 3-5% of the discharge flows around the groyne. The groyne behaves in that sense as a horizontal constriction. It can be expected that the bypassing of water influences the balance of momentum in the whole flume, as there is an exchange of mass back and forth between the channels. Two-dimensional models should capture this flow around an obstacle. It is for these simulations interesting however to make an estimate of the effect of the flow around groynes, and see how its contribution compares to the vertical expansion losses.

To do so we can work out equation (23) for a compound weir on the assumption that the bypassing flows around the groyne tip and not the floodplain and that the discharge enters strictly at the interface between the groyne field and main channel. This way the bypassing discharge enters the streamwise momentum balance in the lateral advection as an exchange process between the main channel and the groyne field, which influences the water level slope of the main channel and the groyne field as:

$$\frac{F_{external}}{\rho d_{gf} g} = - \left( \frac{\Delta H}{S} \right)_{gf} = \frac{U_{mc}}{U_{gf}} \frac{Q_b}{Q_{gf}} \frac{d_{gf}}{S} Fr_{gf}^2 \quad (46)$$

$$\frac{F_{external}}{\rho d_{mc} g} = - \left( \frac{\Delta H}{S} \right)_{mc} = \frac{U_{gf}}{U_{mc}} \frac{Q_{gf}}{Q_{mc}} \frac{Q_b}{Q_{gf}} \frac{d_{mc}}{S} Fr_{mc}^2 \quad (47)$$

The derivation of (46) and (47) is given in Appendix A. The resistance is written in terms of the main flow ( $Fr^2$ ,  $U_{mc}$ ,  $U_{gf}$ ,  $Q_{mc}$  and  $Q_{gf}$ ) and the amount of discharge flowing around the groyne, compared to the amount of discharge flowing in the groyne field  $Q_b/Q_{gf}$ , which is measured. This allows the estimation of the effect of the lateral flow around the groyne on the water level slope.

The applicability of equations (46) and (47) is very limited, as for the derivation only the balance of momentum was considered, while the process is a transfer of mass around the groyne. Furthermore only the influence of the inflow terms are derived, and not those of the outflow terms. So the inflow into the groyne field from the main channel downstream of the groyne is included, while the effect of outflow out of the main channel is not derived. The derived effect of the lateral exchange is an upper boundary for that reason. The derivation gives a start for others to build on, and gives some insight in which terms actually matter in determining the effect of flow around the groyne.

The first term that matters is how much exchange of mass there is ( $Q_b/Q_{gf}$ ). The term is an interpolation between the situation when there is no obstacle, with no discharge flowing around it, and an emerged obstacle. If there is an average flow in the groyne field  $U_{gf} \neq 0$  while the obstacle emerges from the flow all of the discharge has to flow around it. The ratio between the flow velocities  $U_{mc}/U_{gf}$  and  $U_{gf}/U_{mc}$  shows the effect of advection of mass by the region in which the inflowing discharge flows into. The term  $Q_{gf}/Q_{mc}$  shows the influence of the width of the main channel. In the topography only 2 m of main channel and 2 m of groyne field are included, while for real rivers the main channel is much larger than the groyne field. This means that any process at the interface of the groyne field and main channel has a larger effect on the main channel resistance in the experiment than in reality. This holds true for lateral exchange in a horizontal shear layer as well as for the exchange of mass considered here.

The effect of changing the bypassing ration and the width of the main channel in the bypassing model is showed in Figure 38. The boundary conditions for the analysis are taken from simulation G03. The setup of the compound channel model and corresponding bed shear stress is showed in Appendix G. The groyne head loss are the measured Carnot losses. Figure 39 shows that the lateral exchange has a pronounced effect on the water level slope, and less of an effect on the distribution of discharge. The effect that lateral exchange has on the water level slope diminishes when modelling a wider main channel that is more representative of the real river conditions. There is still an effect of the lateral exchange around the groyne, but the effect is more concentrated to the groyne field.



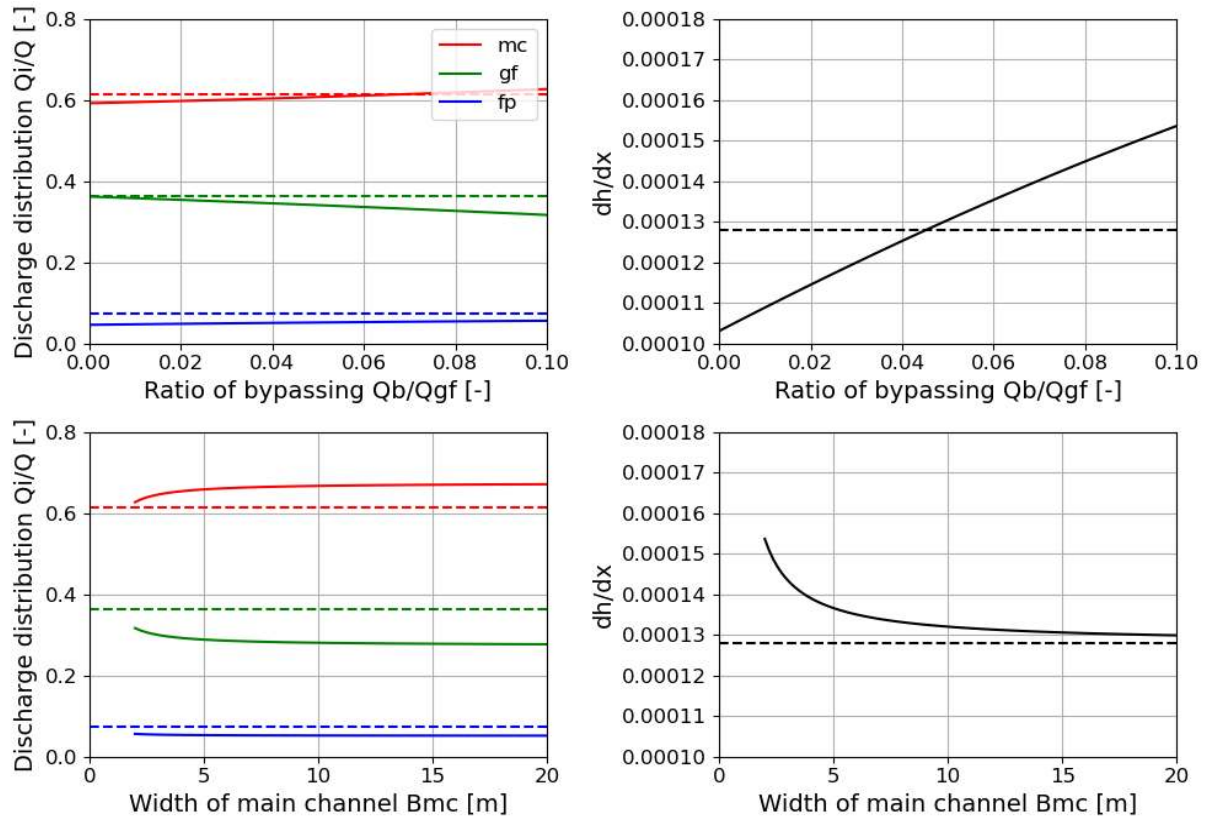


Figure 38; Sensitivity analysis of lateral flow model. The top figures show the sensitivity of the model to changes in the amount of bypassing relative the discharge in the groyne field. The bottom figures show the sensitivity of the model to the width of the main channel. The boundary conditions are taken from simulation G03 and are showed as the dashed lines. The setup of the compound channel model and corresponding bed shear stress is showed in Appendix G. The groyne head loss are the measured Carnot losses.

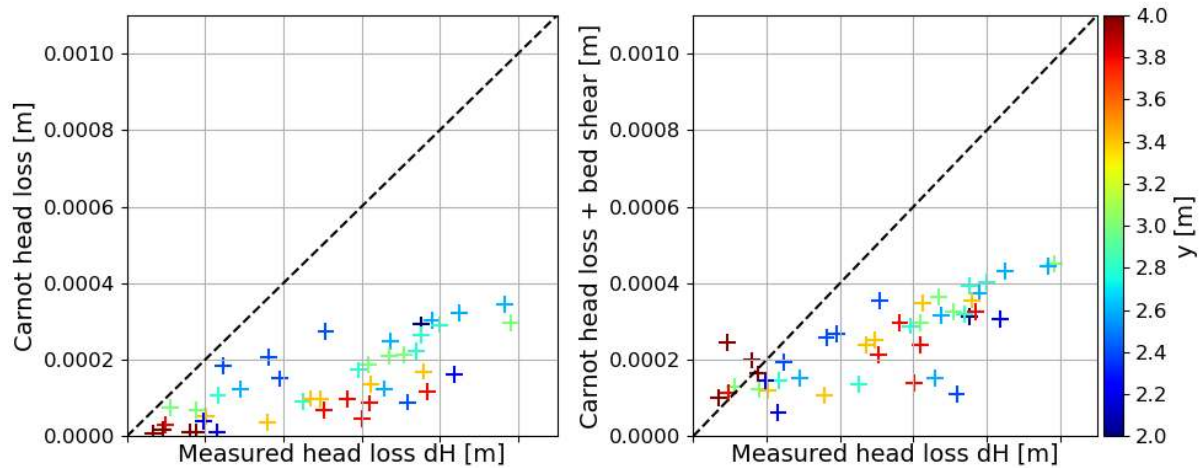


Figure 39; effect of including bed shear stress over a distance of 1.5 m from 0.5 m upstream of one groyne to 1 m downstream. a: without bed shear stress; b: with bed shear stress

## 5.4 Total groyne resistance

Figure 35b shows the Carnot expansion losses over the measured head loss over groynes. The Carnot losses could only explain a part of the head loss over groynes. The bed of the flume has a large hydraulic roughness. It can therefore be expected that the bed shear stress is still visible in the head loss over groynes measured from 0.5 m upstream of the groyne to 1 m downstream of the groyne. The effect of adding the bed shear stress over a distance of 1.5 m is shown in Figure 39. From Figure 39 it becomes clear that the addition of the bed shear stress to the measured Carnot losses does not fully explain the groyne head loss. The remaining unexplained part of the head loss over groynes is possibly due to the three-dimensional flow at the groyne tip, and the lateral exchange of mass around the groyne tip. To assess the influence of those effects models are required as these processes could not be quantified directly from the measurements of flow. To assess the effect of including the lateral exchange of mass an expression was developed that gives an upper bound on the effect of lateral flow around the groyne tip on the streamwise momentum balance.

### Order of magnitude of effect of physical processes

From the measured flow it is possible to make estimates of the influence of different parts of the momentum balance. The question is what the dominant physical processes are in a flow section with groynes. In the literature study we distinguished the bed shear stress, the expansion losses over the groyne crest, the lateral exchange of momentum in the mixing layer and the secondary circulations. In the measurement there was an observed flow around the groyne, which we call the bypassing.

From the results from physical modelling it was described that the effect of bed shear stress and the expansion loss are both dominant, that the lateral exchange can possibly be neglected and that there is a large expected influence of the secondary circulation and an effect of the bypassing around the groyne. To quantify the importance of each effect they are compared as a ration of the pressure gradient. The lateral exchange in the mixing layer is a process that happens at the interface of the groyne field and the main channel. Its effect is spread out over the channel by dividing it with the width of the channel.

$$\text{Pressure gradient: } \frac{\partial h}{\partial x} \quad (48)$$

$$\text{Bed shear: } \frac{g}{C^2} Fr^2 \quad (49)$$

$$\text{Expansion losses: } \frac{1}{S} \frac{\Delta U_g^2}{2g} \quad (50)$$

$$\text{Bypassing: } \frac{U_{mc}}{U_{gf}} \frac{Q_b}{Q_{gf}} \frac{h}{S} Fr^2 \quad (51)$$

$$\text{Lateral exchange: } \frac{1}{B} \sum \frac{d_m}{d} \beta^2 \frac{\Delta U |\Delta U|}{g} \quad (52)$$

This analysis is done at  $x = 25$  m,  $y = 3.0$  m, the middle of the floodplain, assuming  $k_s = 0.016$  m ( $= 2D_{90}$ ) and  $\beta = 0.1$ , and using the groyne measured Carnot losses. The results are shown in Table 4. From this estimation one can easily see that indeed the exchange of momentum in the mixing layer can be neglected when trying to replicate the physical model. This was already suspected from the observed flow velocities with small differences in the flow velocities between the channels. There is a large expected influence of the secondary circulations due to three-dimensional flow around the groyne tip. This term can only be determined as a residual of all other terms however with the current measurements. The analysis furthermore points out the large influence of the bed shear stress due to the large roughness of the bed. With only a few percentages of bypassing discharge around the groyne the empirical derivation most likely overestimated the affect of lateral flow around the groyne.

Table 4; magnitude of different physical processes divided by the pressure gradient of the flow

	G01	G02	G03
$\frac{\text{bed shear}}{\text{pressure gradient}}$	0.7614	0.9448	0.8886
$\frac{\text{expansion losses}}{\text{pressure gradient}}$	0.239	0.357	0.275
$\frac{\text{bypassing}}{\text{pressure gradient}}$	0.169	0.216	0.1957
$\frac{\text{lateral exchange}}{\text{pressure gradient}}$	0.0054	0.0098	0.0087

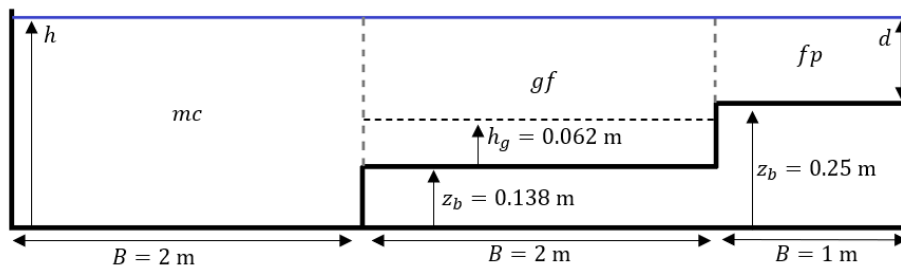


Figure 40; Overview of analytical compound channel model, not to scale. The depth of the groyne field is the average depth in the groyne field. The groyne crest is at 0.2 m above reference, so that  $h_g = 0.062$  m. Simplification of the analytical model includes neglecting the bed slope in the groyne field, neglecting the gradual transition between channel compounds and neglecting the groyne tip.

### Comparison with numerical modelling

Case E01 and G03 have comparable boundary conditions as modelled by Chavarrias (2020) in a numerical model made to represent the physical model. The comparison of numerically modelled water levels and observed water levels is shown in Figure 41. The modelled water levels in the case without groynes are lower than measured, which can be attributed to slight differences in the geometry modelled and the chosen hydraulic roughness in the numerical model. In the numerical model  $k_s = 2D_{90} = 16$  mm, but with the gravel very spaced out the roughness height is probably higher as each particle is more of a stand alone obstacle. For the case with groynes it becomes clear that the two-dimensional numerical model at this state underestimates the groyne resistance while applying the Villemonte weir equation. There seemed to be a large influence of three-dimensional flow at the groyne tip. Including those in the numerical model might improve the numerical modelling of the groyne head loss.

The three-dimensional model predicts a much larger groyne resistance than the two-dimensional model, which indicates a large effect of complex three-dimensional flows. Part of the difference between the numerical simulations and the physical modelling can be explained by a different bed shear stress. It seems however that the numerical model underestimates the effect of secondary circulations. The flow velocities in the physical model do not correspond to those modelled in the three-dimensional model. The numerical model at this stage did not reproduce the region of low flow in Figure 31 and the regions of high flow around the region of low flow. As already discussed these flow patterns seem to originate from secondary circulations. Adaptation of the turbulence models might allow the three-dimensional model to reproduce the observed flow patterns.

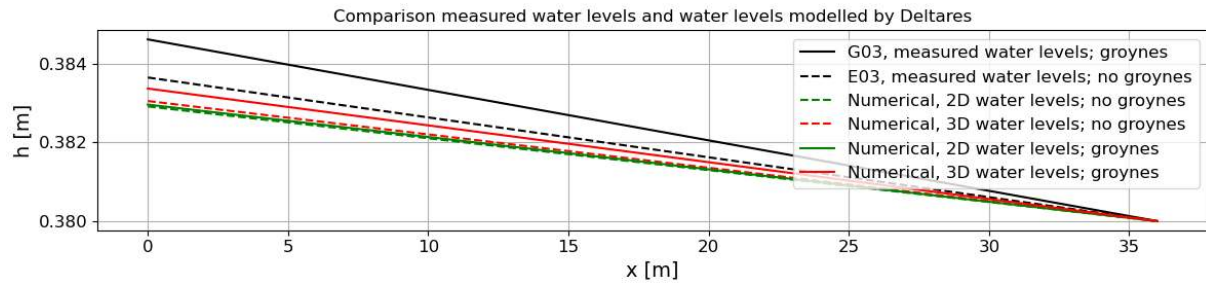


Figure 41; Comparison of numerically modelled water levels and physically observed water levels. All water levels at the downstream boundary equal each other for sake of comparison.

## 5.5 Summary

Discussing the obtained results brought us extra insight in the flow over and around groynes. From the current measurements it seems likely that the expansion of flow in the groyne field does represent expansion of flow over a weir. The expansion losses were overestimated by Villemonte, but based on the current measurements this is more likely due to the high sensitivity of Villemonte at large submergence levels that due to a fundamental difference of expansion of flow over groynes and weirs.

The channel resistance cannot be explained by expansion losses only however and there seems to be a large influence of the three-dimensional flow induced by the flow around the groyne tip which creates vertical flows that redistribute a significant part of the discharge at the groyne tip toward the main channel and deeper into the groyne field. The determination of the effect of the three-dimensional flow might be the most important feature to assess the total groyne resistance.

There furthermore is an effect of flow around the groyne field. Estimation of an upper bound of the influence of lateral flow around the groyne showed that there can be a mayor influence of lateral flow on the channel resistance, and that this effect is enhanced by the physical model, which only includes a part of the main channel in the topography.

## 6 Conclusions

The first objective of this study is to quantify the resistance that highly submerged groynes add to a flow section. Measurement of the head losses and determination of discharge coefficients over groynes made that this objective is fulfilled with the current research. The same measurements can be used for the validation of subgrid models of highly submerged groynes, which is the last objective of this research. Differentiation of the effect of each important process that could influence the groyne resistance was not possible with the current measurements. The second objective of this study, to describe the comparability between flow over highly submerged groynes and flow over weirs, is partly fulfilled for that reason. Having obtained a large amount of measurements from flow over groynes it is possible to answer the research question.

### **What are the dominant physical flow processes in a flow cross section with a series of groynes?**

In the literature study we have constructed a conceptual picture of the flow associated with groyne flow. Each flow process adds new requirements for the modelling of groynes. Not every process in a flume is relevant however, where the groyne resistance preferably is modelled including as few processes as possible. The flow measurements indicated what the dominant physical processes are.

Most of the mentioned processes are observed. These include the contraction and expansion of flow of the groyne, as shown in Figure 28 and Figure 29; the vertical separation and expansion of flow downstream of the groyne crest, as shown in Figure 29; and the vortex shedding from the groyne tip, as sketched in Figure 24. Furthermore a part of the discharge in the groyne field will flow around the groyne rather than over it, as showed in Figure 30 and quantified in Table 3. The observed lateral flow in Figure 28 and the region of low flow in Figure 31 indicate a large effect of three-dimensional flow on the flow resistance.

At the groyne weir-like head losses are observed, as showed in Figure 27. In the groyne field the expansion losses do not dominate the bed shear, due to the high bed roughness in the physical model. Both processes are important to include in the analysis of the flow resistance.

The bypassing is observed and seems to have an impact on flow over the groynes. The total effect of bypassing might be small compared to the bed shear stress. The bypassing however adds another source of friction in the channel that comes as an addition to the weir like expansion.

An important flow feature is the existence of a region of low flow at the groyne tip, such as observed by the PTV and the EMS. The existence of this low flow region cannot be explained in a two dimensional sense, and most probably exists as an effect of secondary circulations due to the way water flows around the groyne tip. The secondary circulations seemed to effectively redistribute flow over the transverse, resulting in a region of low flow at the groyne tip, in a region of high flow in the mixing layer between the main channel and groyne field and in a region of high flow deeper into the groyne field.

### **Where does the energy dissipate in a flow section with a series of groynes?**

There are different distinct energy sinks when modelling a series of groynes. The first is the extra resistance in the groyne field due to the flow expansion over the groyne. The second is a resistance in the whole channel. There is relatively more energy dissipation in the groyne field than in the other channels, causing a redistribution of discharge. This dissipation of energy can be linked to the expansion losses of flow over the groyne. This extra resistance in the groyne field due to expansion losses is not dominant however. A friction in the whole flume caused by the groynes dominated the resistance of the cross section. This friction indicated an exchange process between the main channel and the groyne field that is more effective than can be explained by the streamwise velocity gradients over the transverse. The streamwise velocity gradients over the transverse were small in all simulations, which indicate a very minor influence of lateral shear in the experiment, which correspond to the lack of large eddies in the flume, as observed in the autocorrelation functions in Figure 34. Lateral exchange of momentum is therefore to a lesser extend done by the shear between regions of low and high flow, but probably more by the redistribution of mass due to secondary circulations. A last effect is the lateral flow around the groyne, which can explain some of the head loss over the groyne, and increases the channel resistance of the whole flume.

### **To what extent does a groyne behave like a weir?**

In the groyne field the dominant flow pattern was of acceleration and deceleration over the groyne. This was first observed in the surface velocity graphs in Figure 28, and then in the vertical flow profiles in Figure 29. The reattachment length has the same magnitude of that of a backwards facing step. The measured Carnot loss over the groyne corresponded to those modelled in a two-dimensional vertical weir model, which indicate that the expansion losses over a groyne does resemble weir-like flow expansion and that there is no reduced expansion loss due to sideways levelling of the under pressure, such as suggested by Jongeling et al. (Jongeling, Goede, & Keser, 2012). The similarity between groynes and weirs is present from the groyne at  $y = 2.4$  m to the end at  $y = 3.8$  m.

At the groyne tip no sign of flow separation is found, and there seems to be no similarity with weir flow at the groyne tip measured at  $y = 2.2$  m. The main effect the groyne tip seemed to have is to induce a three-dimensional flow pattern around the groyne. This three-dimensional flow does seem to influence the head loss observed over the groyne, so that head loss estimated as a Carnot loss does not equal the observed head loss over the groyne. The observed head loss is then the sum of the contributions. This makes it difficult to determine what the exact effect is of flow expansion, and what is due to other flow processes.

The exact location of the transition between weir-like expansion over the groyne and non-weir-like flow over the groyne tip is not determined. The transition is between  $y = 2.2 - 2.4$  m, with the main body of the groyne starting at  $y = 2.3$  m. The transition, for this groyne geometry, is therefore close to the geometrical transition between the groyne tip and the main body.

### **What is the total effect groynes have on the resistance of a flow section?**

The first effect of the groyne is an expansion loss, which is a local process and should be predictable as an expansion loss following a backward facing step. There seems to be a large effect of secondary flow, which effectively transfers discharge through a cross-section, and will therefore influence the total groyne resistance. There is some flow around the groyne, which transfers mass around the groyne through the main channel and floodplain. This bypassing will have an effect on the water level slope.

### **Can this resistance be predicted by weir expansion losses?**

Using the weir formula developed by Van Broekhoven (2007) it was possible to reproduce the Carnot expansion losses. Applying the Villemonte weir formulation (Sieben, 2011) overestimates the weir expansion losses. The latter is based on the Carnot losses, and should give equal results to the Carnot losses. Based on the current measurements it seems more likely however that the implementation of the blockage ratio in Villemonte does not reproduce the Carnot head losses very well for very high submergence levels, rather than indicating that the expansion of flow over a groyne is fundamentally different than flow over weirs. It seems most likely that weir head loss formulas are applicable for the simulation of flow over groynes, but that the formula used to model the weir head loss in the Dutch rivers, Villemonte, might overestimate the head loss for large submergence levels. Modelling of the head losses over groynes as weir expansion losses would require a thorough understanding however of the effect that three-dimensional flows induced by the flow around the groyne have on the channel resistance. The quantification of this effect might prove to be more difficult than adapting weir formula to fit the measurements, without explicitly modelling the effect of the three-dimensional flow.



## 7 Recommendations

From the current measurements it was concluded that the vertical expansion of flow did represent weir expansion losses. Differences of the observations with the Villemonte formula were explained by the large submergence, for which the formula is very sensitive. It is recommended to do experiments in the same way as done here with lower water levels. When for those water levels the Villemonte equation keeps overestimating the expansion losses it might indicate that the conclusion drawn here are not correct and expansion of flow over a groyne does differ from vertical expansion over a weir.

There seemed to be a large influence of three-dimensional flow. It is recommended to capture one transact for each simulation with a large amount of three-dimensional measurements in the horizontal and vertical. Firstly this should be done far away from the groynes. Lastly this should be done around the groyne. From these measurements it is possible to quantify the effect of secondary flows, and separate them from the effect of bed shear stress. The latter could not be done in these experiments.

An important reason why the simulations without groynes were done was to assess the bed shear stress. It proved impossible however to obtain useful numbers that represented the bed shear stress. This includes measurements in three directions (Besseling, 2021) as well as in two directions. It is recommended to do measurements of the flow in a straight tilting flume with the same roughness installed to clearly separate the effect of secondary flows and the bed shear stress.

The measurements did not suffice to capture the complex flow around the groyne tip. With the streamwise velocity dominant over the other flow components it might be very difficult to measure all relevant details at the groyne tip even with ADV measuring in 3 directions at 200 Hz. It is therefore recommended to investigate the flow around the groyne tip in a 3D (non-hydrostatic) model, (using a flexible mesh) to obtain a large modelling precision and more efficiently determine the effect of the complex flow.

For the numerical modelling of this experiment, and the validation of the subgrid weir models, it is recommended to first construct a three-dimensional model that can reproduce the observed flow as a better benchmark for the subgrid modelling, as it might be more convenient to quantify the effect of complex flow in a numerical model than by measurement of the flow. For the three-dimensional model it might be important to use a different eddy viscosity model than the  $k - \epsilon$  model, as Ambagts (2019) was only able to reproduce the wake flow with changes in the turbulent modelling and Kuhnle et al. (2008) observed deviations between the three dimensional model and flow measurements because of the turbulence modelling in the wake with the  $k - \epsilon$  model. Having a three-dimensional numerical model verified on the flow measured here allows the differentiation of the effect of different flow processes and allows the fitting of subgrid models to the three-dimensional model, without including non-weir-like processes in the subgrid formula.

It is recommended to wait with fitting the Villemonte formula on the obtained discharge coefficients from this experiment until the effect of the complex flow is quantified, so that the effect of those can be separated from vertical expansion losses, which is preferably the only process that is represented by a weir expansion loss formula. It is not recommended to model the groyne tip as a compound weir because at the groyne tip there is no sign of expansion losses. Furthermore the Villemonte equation is exceptionally sensitive when the height of the groyne crest reduces to zero, so that slight errors in either the data or the fitting might have a large impact on the modelling of the total groyne resistance.

There are some recommendations regarding follow-up experiments in the same flume to improve the physical modelling. First of all it is recommended to further improve the inflow conditions, by splitting up the inflow into three separately controllable compounds, so that the downstream discharge distribution can be enforced upstream.

The next recommendation for experiments in the same flume is to repeat some of the measurements which could not be used in this thesis. These include measurement of the flow velocities in the floodplain for all cases without groynes (E01-E13) and measurement of the flow around the groynes for the cases G01 and G02.

The periodic motions as observed by others were not observed in these experiments. These motions were the reason for choosing a point measurement time of 5 minutes. The last recommendation for experiments in the same flume is to assess with the new devices whether large scale motions are still not observed. If these large scale motions are still not observed the measurement time can be reduced significantly to speed up the measurements.



## Bibliography

- Ambagts, L. (2019). *Flow over and around submerged groynes - Numerical modelling and analysis of a groyne flume experiment*. Delft: Delft University of Technology.
- Arcement, G. J. (1989). *Guide for Selecting Manning's Roughness Coefficients for Natural Channels and Flood Plains*. Denver: United States Government Printing Office.
- Besseling, R. M. (2021). *Bed roughness of river channels - Determination and analysis of the bed roughness of a groyne flume experiment by using the ADV*. Delft: Delft University of Technology.
- Blumenthal, K., & Ubels, J. (1961). *Verantwoording betreffende de ontstaanswijze van de tabellenmethode voor het berekenen van overlaten bij stroombaanberekeningen*. Arnhem: Rijkswaterstaat.
- Bos, M. G. (1989). Discharge measurement structures. *International Institute for Land Reclamation and Improvement (ILRI)*, 20, 401.
- Broekhoven, R. W. (2007). *Het effect van kribverlaging op de afvoercapaciteit van de Waal ten tijde van hoogwater*. Delft: Delft University of Technology.
- Chavarrías, V. (2020). *Modelling laboratory groynes: set-up of a Delft3D-FM model 11205235-015-ZWS-0001*. Delft: Deltares.
- Chavarrías, V., Busnelli, M., & Sloff, K. (2020). *Morphological models for IRM: Rhine branches 1D*. Deltares. Delft: Deltares.
- Chavarrías, V., Platzek, F., & Yossef, M. (2019). *Laboratory experiment for submerged groynes: results from preliminary numerical simulations 11203682-005*. Memo, Deltares.
- Clauser, F. H. (1954). Turbulent Boundary Layers in Adverse Pressure Gradients. *Journal of the Aeronautical sciences*, 91-108.
- Colebrook, C. F., & White, C. M. (1937). *Experiments with Fluid Friction in Roughened Pipes*. London.
- Deltares. (2020). *Instrument, Programmable electromagnetic liquid velocity meter*. Manual.
- Elger, D. F., LeBret, B. A., Crowe, C. T., & Roberson, J. A. (1975). *Engineering Fluid Mechanics*. Hoboken: Wiley.
- Fenton, J. D. (2003). The effect of obstacles on surface levels and boundary resistance in open channels. *30th IAHR Congress*, (pp. 24-29). Thessaloniki.
- Fischer, H. B., Imberger, J., List, E. J., Koh, R. C., & Brooks, N. H. (1979). *Mixing in Inland Coastal Waters*. San Diego: Academic Press.
- Gao, J., Agarwal, K., & Katz, J. (2021). Experimental investigation of the three-dimensional flow structure around a pair of cubes immersed in the inner part of a turbulent channel flow. *Journal of Fluid Mechanics*(918).
- Graf, W. H., & Song, T. (1995). Bed-shear stress in non-uniform and unsteady open-channel flows. *Journal of hydraulic research*, 33(5), 699-704.
- Hüsener, T., Faulhaber, P., & Baron, M. (2012). Modifikationen in bestehenden Stromregelungssystemen an Wasserstraßen - Untersuchung mit gegenständlichen und numerischen Verfahren. *Wasserbausymposium 2012* (pp. 395-402). Graz: Technische Universität Graz.
- Jain, S. (2001). *Open-channel flow*. New York: John Wiley and Sons.
- Jansen, M. (2020). *Compound weirs, Analytical Discharge Computations*. Delft: Delft University of Technology.
- Jongeling, J., Goede, E. d., & Keser, J. v. (2012). *Stroomlijnen van kribben in WAQUA. Memo 1002047-000-ZWS-0012*. Delft: Deltares.

- Karman, V. (1930). *Mechanical similtude and turbulence, reprint form Nachrichten von der Gesellschaft der Wissenschaften zu Gottingen*. Washington: NASA.
- King, H. W. (1939). *Handbook of hydraulics for the solution of hydraulic problems*. McGraw-Hill Book Company.
- Kruijt, M. (2013). *Resistance of submerged groynes*. Delft: Delft University of Technology.
- Kuhnle, R. A., Jia, Y., & Alonso, C. A. (2008). Measured and Simulated Flow near a Submerged Dpur Dike. *Journal of hydraulic engineering*, 134(7), 916-924.
- Micro-Epsilon. (2008). *Instruction Manual optoNCDT 1302*. Ortenburg.
- Morley, S., Brito, T., & Welling, D. (2017). Measures of Model Performance Based On the Log Accuracy Ratio. *Space Weather*, 16, 69-88.
- Nakagawa, H., & Nezu, I. (1986). Experimental investigation on turbulent structures of backward-facing step in an open channel. *Journal of hydraulic research*, 25(1), 67-88.
- Nieuwstadt, F. T., Boersma, B. J., & Westerweel, J. (1998). *Turbulence, Introduction to Theory and Application of Turbulent Flows*. Springer. doi:10.1007/978-3-319-31599-7
- Nieuwstadt, F. T., Boersma, B. J., & Westerweel, J. (1998). *Turbulence, Introduction to Theory and Application of Turbulent Flows*. Springer.
- Nikuradse, J. (1950). *Laws of Flow in Rough Pipes*. Washington: National Advisory Comittee for Aeronautics.
- Omer, A., & Yossef, M. F. (2017). *Modelling of flow over weirs and groynes - Qualitative comparison between results of numeral models and laboratory experiments 11200536-011*. Deltares.
- Prandtl, L., & Tietjens, O. (2003). *Applied Hydro- and Aeromechanics*. Dover: Dover Publications Inc.
- Prooijen, B. C. (2004). *Shallow Mixing Layers*. Delft: Delft University of Technology.
- Prooijen, B. C., Battjes, J. A., & Uijttewaal, W. S. (2005). Momentum Exchange in Straight Uniform Compound Channel Flow. *Journal of Hydraulic Engineering*, 131(3), 175-183.
- Proust, S., Bousmar, D., Paquier, A., & Zech, Y. (2010). Energy losses in cmpound open channels. *Advances in Water Resources*, 33(1), 1-16.
- Rantz, & S.E. (1982). *Measurement and computation of streamflow: Volume 1. Measurement of stage and discharge*. U.S. Geological Survey Water-Supple Paper 217.
- Rastogi, A. K., & Rodi, W. (1978). Predictions of Heat and Mass Transfer in Open Channels. *Journal of the Hydraulics Division*, 104(3), 397-420.
- Rice, C. E. (1974). *Hydraulics of Main Channel-Floodplain Flows*. Stillwater: Oklahoma Water Resources Center.
- Rijkswaterstaat. (2016). *WAQUA/TRIWAQ - two- and three-dimensional shallow water flow model. Technical documentation*.
- Rijn, L. v. (1990). *Principles of fluid flow and surface waves in rivers, estuaries, seas, and oceans*. Oldemarkt: Aqua Publications.
- Schiereck, G. J. (2016). *Introduction to bed, bank and shore protection*. Delft: Delft Academic Press.
- Schijndel, S. A., & Jagers, H. R. (2002). *Anticiperend onderzoek kribben*. Delft Hydraulics, WL, The Netherlands.
- Schlichtig, H., & Gersten, K. (1955). *Boundary-Layer Theory*. New York: McGraw-Hill.
- Shiono, K., & Knight, D. W. (1991). Turbulent open-channel flows with variable depth across the channel. *Journal of Fluid Mechanics*, 222, 617-646.

- Sieben, A. (2003). *Gestroomlijnde zomerkaden, de invloed van het dwarsprofiel op energieverliezen bij overlaten*. Rijkswaterstaat.
- Sieben, A. (2011). *Overzicht en synthese beschikbare data overlaatproeven, Update 2011*. Rijkswaterstaat.
- Sieben, A. (2017). *Overzicht metingen stroming over kribben*.
- Song, T., & Chiew, Y. M. (2001). Turbulence Measurement in Nonuniform Open-Channel Flow Using Acoustic Doppler Velocimetry (ADV). *Journal of Engineering Mechanics*, 127(3), 219-232.
- Strurn, T. W. (2001). *Open Channel Hydraulics*. Singapore: McGraw-Hill.
- Tanner, W. F. (1963). Spiral Flow in Rivers, Shallow Seas, Dust Devils, and Models. *Science*(139), 41-42.
- Uijttewaai, W. S. (2005). Effects of Groyne Layout on the Flow in Groyne Fields: Laboratory Experiments. *Journal of Hydraulic Engineering*, 131(9), 782-791.
- Uijttewaai, W. S. (2019). *Laboratory experiment for submerged groynes: experimental design and implementation*. Delft: Delft University of Technology.
- Uijttewaai, W. S., Lehmann, D., & Mazijk, A. v. (2001). Exchange processes between a river and its groyne fields: model experiments. *Journal of Hydraulic Engineering*, 127(11), 928-936.
- Villemonte, J. R. (1947). Submerged weir discharge studies. *Engineering news record*, 139(26), 54-56.
- Vreugdenhil, C. B. (1994). *Numerical Methods for Shallow-Water Flow*. Utrecht: Kluwer Academic Publishers. doi:10.1007/978-94-015-8354-1
- Walker, J. F. (1988). General Two-Point Method for Determining Velocity in Open Channel. *Journal of Hydraulic Engineering*, 114(7), 801-805.
- Yang, K., Cao, S., & Knight, D. W. (2007). Flow Patterns in Compound Channels. *Journal of Hydraulic Engineering*, 133(2), 148-159.
- Yossef, M. F. (2004). The effect of the submergence level on the resistance of groynes, an experimental investigation. *The 6th Conference on Hydrosience and Engineering (IHCE\_2004)*. Brisbane, Australia.
- Yossef, M. F. (2005). *Morphodynamics of Rivers with Groynes*. Delft: Delft University of Technology.
- Yossef, M. F. (2017). *Hydraulic modelling of standard and streamlined groynes 11201089-000*. Delft: Deltares.
- Yossef, M. F., & Visser, T. (2018). *Effect of groyne schematisation on WAQUA model results 11202188-008*. Delft: Deltares.
- Yossef, M. F., & Vriend, H. J. (2011). Momentum Exchange in Straight Uniform Compound. *Journal of Hydraulic Engineering*, 137(5), 504-516.
- Zagonjolli, M. (2017). *Sensitivity analysis on the groyne modelling in WAQUA 1230071-003*. Deltares. Delft: Deltares.
- Zagonjolli, M., Platzek, F., & Kester, J. v. (2017). *Modelling the flow over a groyne and weir in WAQUA 11200536-008*. Delft: Deltares.
- Zhao, G. (2016). *Breach growth in cohesive embankments due to overtopping*. Delft: Delft Academic Press.
- Zheleznyakov, G. V. (1950). *Gidravlicheskie osnovaniya metodov rechnoi gidrometrii (Hydraulic Basis of the Methods of River Hydrometry)*. Moskva-Leningrad: Izdatelstvo Akademii Nauk, SSSR.
- Zijlema, M. (2011). *CIE4340, Computational modelling of flow and transport*. Delft: Delft University of Technology.

Zuurveld, J. (1998). *Hoofdstroming contra menglaag. De invloed van een menglaag op het begin van bewegen van bodemmateriaal*. Delft: Delft University of Technology.

## Appendix A

### Derivation momentum balance of the groyne field with bypassing discharge

The goal of this appendix is to include the bypassing around the groyne as a lateral advection in a one-dimensional equation for the groyne resistance. This is done by considering the conservation of momentum in a body of water downstream of the groyne, as shown in Figure 42. This is the region of flow expansion over the groyne, and bypassing around the groyne re-enters the domain downstream of the groyne. Subscript 2 refers to the groyne crest. Subscript 3 refers to the transect downstream of the groyne crest. The procedure followed for this derivation is to split the discharge in the groyne field in the part that is flowing over the groyne  $Q_g$ , and the bypassing discharge  $Q_b$ , which together form the discharge in the groyne field  $Q_{gf} = Q_g + Q_b$ . The first assumption is that  $Q_g$  enters the domain over the full width of the groyne field so that  $Q_g = U_2 \cdot d_2 \cdot B_{gf}$ . The second assumption is that the bypassing discharge enters the domain from the side only, so that  $Q_b = V_{in} \cdot \frac{1}{2}(h_2 + h_3) \cdot \Delta x$ . The resulting momentum balance is rewritten such that it is again a one dimensional equation including a loss term that stands for the effect of including the bypassing as a lateral advection.

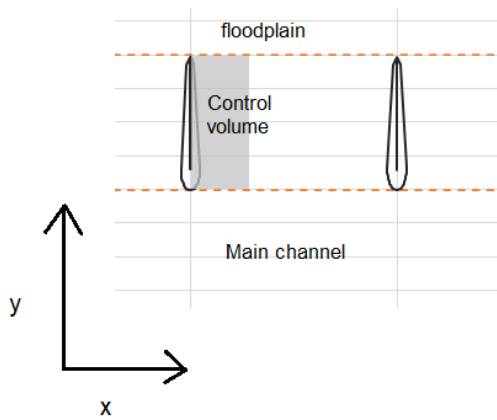


Figure 42; location of control volume for inclusion of bypassing as lateral advection

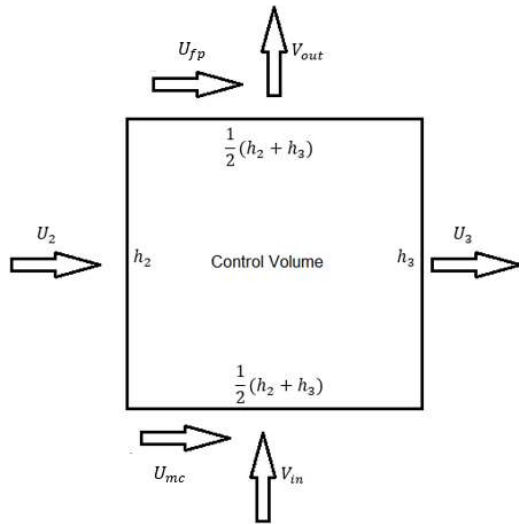


Figure 43; control volume from the groyne cresh to downstream showing a flux into the balance area of size  $\Delta y, \Delta x$

In this volume the momentum flux is conserved. The balance for the control volume in Figure 43 reads (neglecting the bed shear stress):

$$\rho U_2^2 h_2 \Delta y - \rho U_3^2 h_3 \Delta y + \rho U_{mc} V_{in} \frac{1}{2} (h_2 + h_3) \Delta x - \rho U_{gf} V_{out} \frac{1}{2} (h_2 + h_3) \Delta x = \rho (gh_3^2 - gh_2^2) \Delta y \quad (53)$$

For this derivation we assume the reference level  $z_0$  is the bottom of the groyne field, so that  $d_2 = h_2 - h_g$  and  $h_2, h_3$  are the total water depth in the groyne field. In the momentum balance there is no sideways outflow ( $V_{out} = 0$ ) and  $\Delta y = B_{gf}$ . Division by  $\rho B_{gf}$  now gives:

$$U_2^2 d_2 - U_3^2 h_3 + \frac{1}{2} U_{mc} (h_2 + h_3) V \frac{\Delta x}{B_{gf}} = gh_3^2 - gh_2^2 \quad (54)$$

The first assumption is that the flow over the groyne enters the domain over the full width of the groyne field:

$$Q_g = U_2 \cdot d_2 \cdot B_{gf} \quad (55)$$

The second assumption is that the bypassing discharge enters the domain from the side only:

$$Q_b = V_{in} \cdot \frac{1}{2} (h_2 + h_3) \cdot \Delta x \quad (56)$$

This means that:

$$Q_{gf} = Q_g + Q_b; U_2 = \frac{Q_g}{d_2 B_{gf}}; V = \frac{Q_b}{\Delta x \frac{1}{2} (h_2 + h_3)}; U_3 = \frac{Q_{gf}}{h_3 B_{gf}}$$

Implementing these assumptions in equation (54) results in:

$$\frac{Q_g^2}{d_2^2 B_{gf}^2} d_2 + \frac{1}{2} U_{mc} (h_2 + h_3) \frac{Q_b}{\Delta x \frac{1}{2} (h_2 + h_3)} \frac{\Delta x}{B_{gf}} + gh_2^2 = \frac{Q_{gf}^2}{h_3^2 B_{gf}^2} h_3 + gh_3^2 \quad (57)$$

Which simplifies to:

$$\frac{Q_g^2}{d_2^2 B_{gf}^2} + U_{mc} \frac{Q_b}{B_{gf}} + gh_2^2 = \frac{Q_{gf}^2}{h_3^2 B_{gf}^2} + gh_3^2 \quad (58)$$

It is desirable however to rewrite the equation in terms of  $Q_{gf}$  and  $Q_b/Q_{gf}$ . The first is convenient to measure and the latter is dimensionless and can be the subject of further research determining relations for  $Q_b/Q_{gf}$  related to the topography and hydraulic stage of the flow. Rewriting the flow in this manner also results in a form in which it is no longer necessary to include the actual discharge on the groyne in an analytical model.

To achieve such a form one applies  $Q_g = Q_{gf} - Q_b$ :

$$\begin{aligned} & \frac{(Q_{gf} - Q_b)^2}{d_2^2 B_{gf}^2} + U_{mc} \frac{Q_b}{B_{gf}} + gh_2^2 = \frac{Q_{gf}^2}{h_3^2 B_{gf}^2} + gh_3^2 \rightarrow \\ & \left( \frac{Q_{gf}^2}{d_2^2 B_{gf}^2} + \frac{Q_b^2}{d_2^2 B_{gf}^2} - \frac{Q_{gf} Q_b}{d_2^2 B_{gf}^2} \right) + \frac{U_{mc} Q_{gf} Q_b}{U_{gf} h_3 B_{gf}^2} + gh_2^2 = \frac{Q_{gf}^2}{h_3^2 B_{gf}^2} + gh_3^2 \rightarrow \\ & \left( \frac{Q_{gf}^2}{d_2^2 B_{gf}^2} - \frac{Q_b}{Q_{gf}} \frac{Q_{gf}^2}{d_2^2 B_{gf}^2} + \left( \frac{Q_b}{Q_{gf}} \right)^2 \frac{Q_{gf}^2}{d_2^2 B_{gf}^2} \right) + \frac{U_{mc} Q_b}{U_{gf} Q_{gf}} \frac{Q_{gf}^2}{h_3 B_{gf}^2} + gh_2^2 = \frac{Q_{gf}^2}{h_3^2 B_{gf}^2} + gh_3^2 \end{aligned} \quad (59)$$

The first part in (59) contains a reduction of the work done flowing over the groyne compared to the situation without bypassing. The second part is an increase in work due to the lateral inflow of bypassing discharge.

In (59) all terms related to  $\left(\frac{Q_b}{Q}\right)^2$  are neglected. As long as the amount of bypassing is only small this gives a small error only as  $\left(\frac{Q_b}{Q}\right)^2 \ll \frac{Q_b}{Q}$ :

$$\begin{aligned} & \left( \frac{Q_{gf}^2}{d_2 B_{gf}^2} - \frac{Q_b}{Q} \frac{Q_{gf}^2}{d_2 B_{gf}^2} \right) + \frac{U_{mc}}{U_{gf}} \frac{Q_b}{Q_{gf}} \frac{Q_{gf}^2}{h_3 B_{gf}^2} + g h_2^2 = \frac{Q_{gf}^2}{h_3 B_{gf}^2} + g h_3^2 \rightarrow \\ & \left( 1 - \frac{Q_b}{Q_{gf}} \right) \frac{Q_{gf}^2}{d_2 B_{gf}^2} + \frac{U_{mc}}{U_{gf}} \frac{Q_b}{Q_{gf}} \frac{Q_{gf}^2}{h_3 B_{gf}^2} + g h_2^2 = \frac{Q_{gf}^2}{h_3 B_{gf}^2} + g h_3^2 \end{aligned} \quad (60)$$

Which gives a balance in momentum flux in one dimension by multiplying with  $\rho B_{gf}$ :

$$\rho \left( 1 - \frac{Q_b}{Q_{gf}} \right) \frac{Q_{gf}^2}{A_2} + \rho g B_{gf} h_2^2 = \rho \left( 1 - \frac{U_{mc}}{U_{gf}} \frac{Q_b}{Q_{gf}} \right) \frac{Q_{gf}^2}{A_3} + \rho g B_{gf} h_3^2 \quad (61)$$

Equation (62) contains two differences with the momentum conservation neglecting bypassing. Firstly the kinetic energy inflowing at the groyne is reduced by  $(1 - Q_b/Q)$ . This is a logical conclusion considering that less flow goes over a groyne. Secondly there is an extra term acting on the main flow with a size  $(U_{mc}/U_{gf}) \cdot (Q_b/Q)$ . This term originates from the bypassing entering the domain downstream of the groyne.

To include the effect together with the groyne friction loss one can include the above mentioned extra contributions in the linearization of the momentum balance, as performed by Fenton (2003), which determined the loss over an obstacle:  $D = M_1 - M_3$ . The force acting on the groyne is the difference in the momentum flux upstream and downstream with  $D = \frac{1}{2} \rho C_D U^2 a$ . In which  $a$  the area of the object in the transverse direction ( $= h_g \cdot B_{gf}$ ):

$$\frac{1}{2} \rho C_D U^2 a = \rho \left( g A h + \frac{Q^2}{A} \right)_1 - \rho \left( g A h + \frac{Q^2}{A} \right)_3; \text{ (Fenton, 2003)} \quad (62)$$

The friction formulation for an obstacle  $\frac{1}{2} \rho C_D U^2 a$  closely resembles the kinetic energy at the inflow boundary. In fact:

$$\frac{1}{2} \rho C_D U^2 a = \frac{1}{2} C_D \frac{h_g}{h_2} \rho \frac{Q_g^2}{A_2} \quad (63)$$

The first effect of bypassing, that is the reduction of expansion loss over the groyne, can therefore be included in the formulation of the drag friction of the obstacle by multiplying it with  $(1 - Q_b/Q)$ .

The effect of bypassing in the lateral advection can be added to the momentum balance at the downstream end. Following the linearization of Fenton the resulting water level slope due to groynes becomes:

$$\frac{\Delta h}{h_3} = \left( 1 - \frac{Q_b}{Q_{gf}} \right) \frac{1}{2} C_D \frac{a}{A_3} \frac{Fr_3^2}{Fr_3^2 - 1} + \frac{U_{mc}}{U_{gf}} \frac{Q_b}{Q_{gf}} \frac{Fr_3^2}{Fr_3^2 - 1} \quad (64)$$

Including multiple groynes and considering the water level slope over the whole groyne results in:



$$-\frac{\partial h}{\partial x} = \left(1 - \frac{Q_b}{Q_{gf}}\right) \frac{1}{2} C_D \frac{h_g}{S} \frac{Fr^2}{1 - Fr^2} + \frac{U_{mc}}{U_{gf}} \frac{Q_b}{Q_{gf}} \frac{h}{S} \frac{Fr^2}{1 - Fr^2} \quad (65)$$

The term  $\frac{Fr^2}{1 - Fr^2}$  is the same to which the bed shear stress coefficient  $g/C^2$  is multiplied and shows how these contributions can be included in the global momentum balance. The division  $1 - Fr^2$  is due to the inclusion of advection. In a stationary flow this division is not included in the bed shear stress, but is included in the groyne resistance still as the advection is relevant in accelerating and decelerating flow over a groyne.

Inclusion of the groyne resistance in the momentum balance results in:

$$-\left(\frac{\partial h}{\partial x}\right)_{gf} = \left(\frac{g}{C_{gf}^2} + \left(1 - \frac{Q_b}{Q_{gf}}\right) \frac{1}{2} C_D \frac{h_g}{S} + \frac{U_{mc}}{U_{gf}} \frac{Q_b}{Q_{gf}} \frac{d_{gf}}{S}\right) \frac{1}{\frac{1}{Fr_{gf}^2} - 1} \quad (66)$$

Upstream of the groyne the same derivation can be done for the bypassing discharge flowing from the groyne field into the main channel. Relating the inflowing discharge to the bypassing discharge relative to the discharge in the groyne field adds a multiplication however of  $Q_{gf}/Q_{mc}$ :

$$-\left(\frac{\partial h}{\partial x}\right)_{mc} = \left(\frac{g}{C_{mc}^2} + \frac{U_{gf}}{U_{mc}} \frac{Q_{gf}}{Q_{mc}} \frac{Q_b}{Q_{gf}} \frac{d_{mc}}{S}\right) \frac{1}{\frac{1}{Fr_{mc}^2} - 1} \quad (67)$$

## Appendix B

This appendix shows the measurement points for each different simulation in the horizontal and vertical plane.

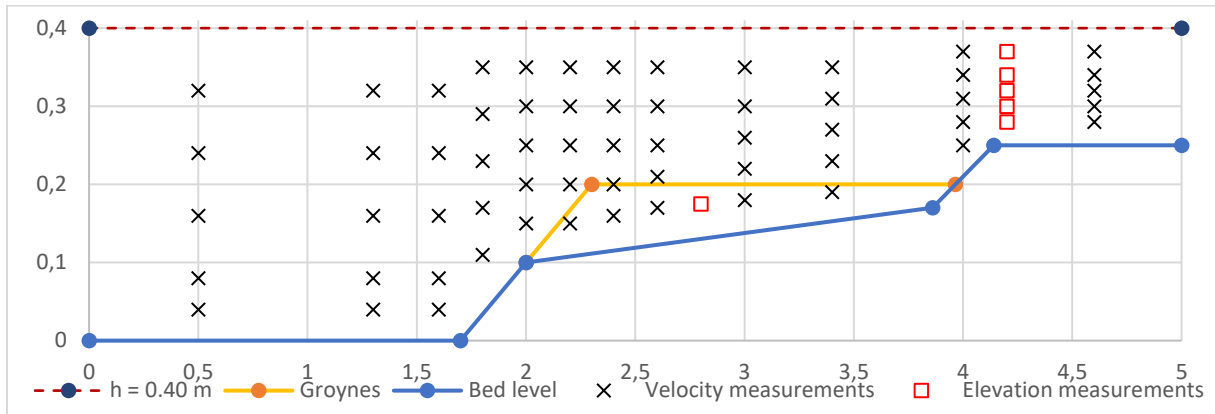


Figure 44; Measurement point in one cross section for the simulations with water depth  $d = 40$  cm. The axes are in [m]

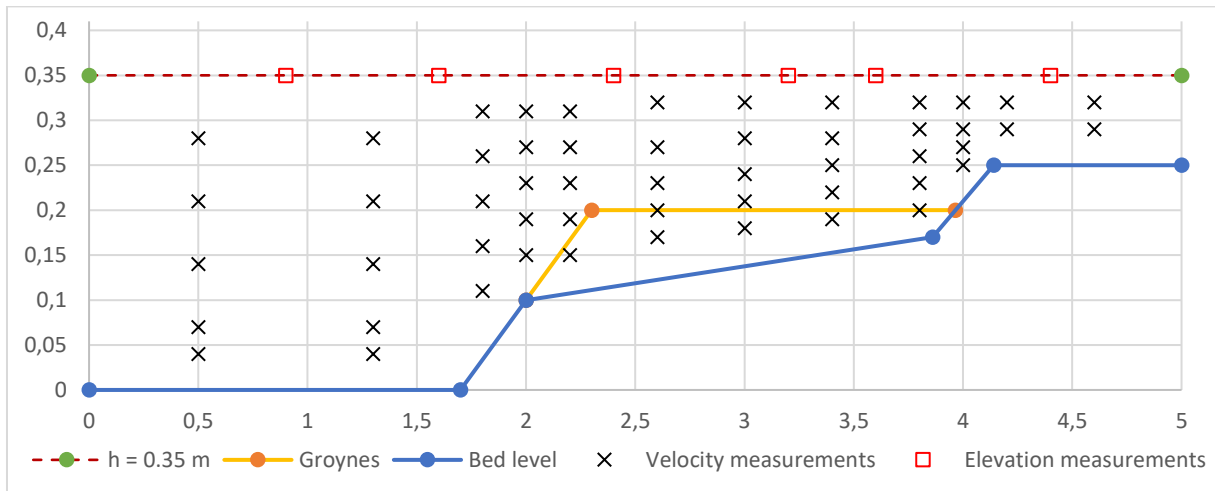


Figure 45; Measurement point in one cross section for the simulations with water depth  $d = 35$  cm. The axes are in [m]

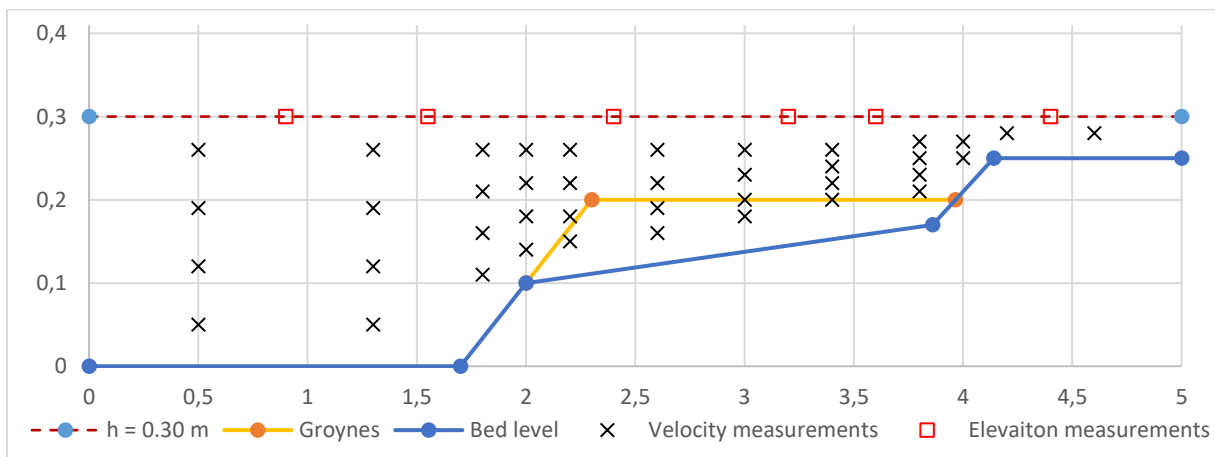


Figure 46; Measurement point in one cross section for the simulations with water depth  $d = 30$  cm. The axes are in [m]

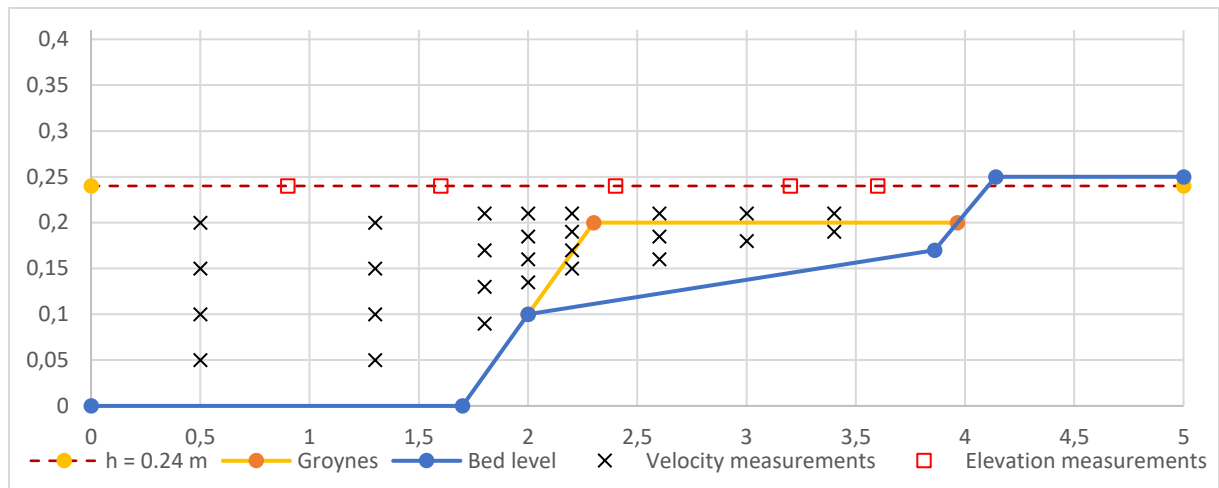


Figure 47; Measurement point in one cross section for the simulations with water depth  $d = 24$  cm. The axes are in [m]

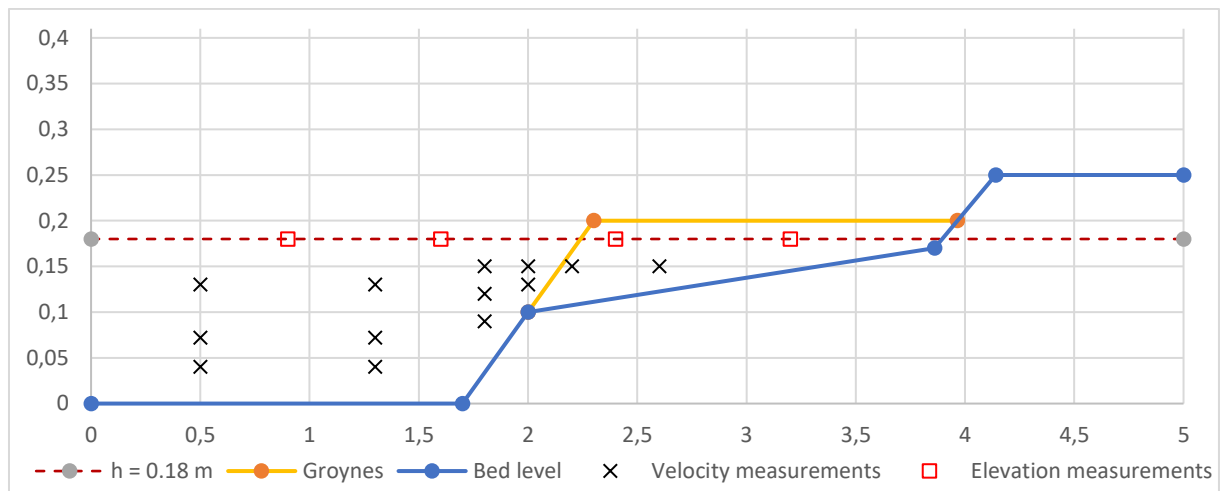


Figure 48; Measurement point in one cross section for the simulations with water depth  $d = 18$  cm. The axes are in [m]

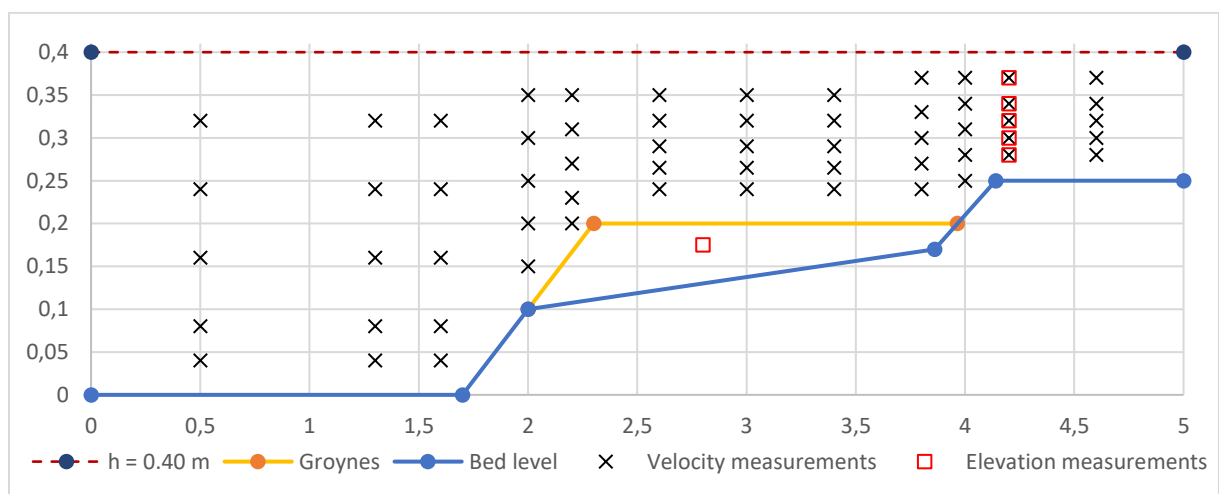


Figure 49; Measurement point on top of one groyne for the simulations with a water depth of  $d = 40$  cm. The axes are in [m]

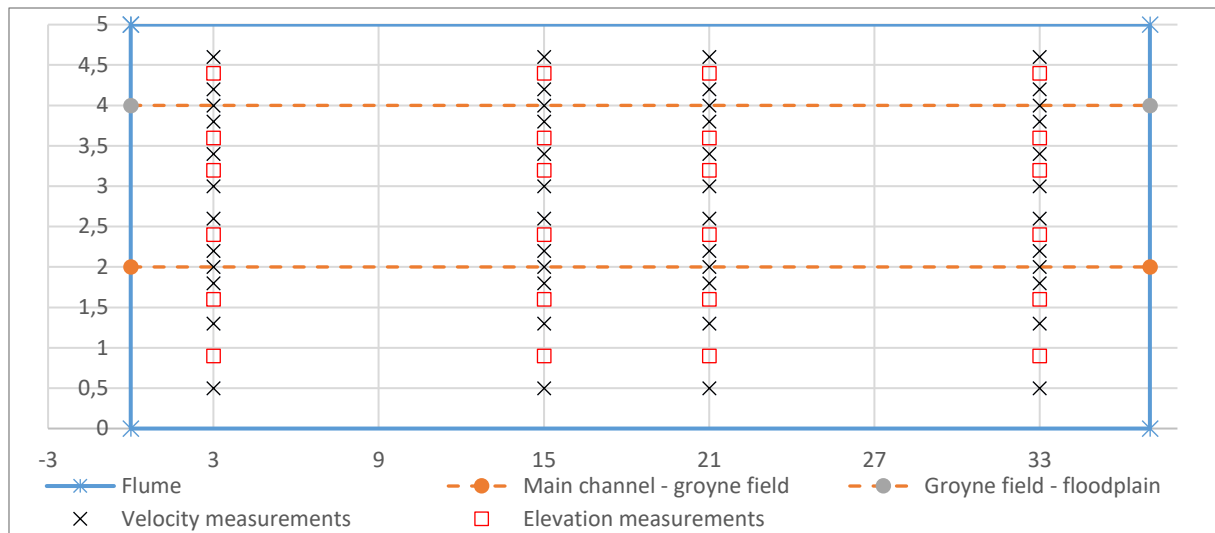


Figure 50; Location the measurement points of the cross sections for the simulations without groynes with water depths of 30, 35 and 40 cm. The axes are in [m]. In blue the area measured with the PTV.

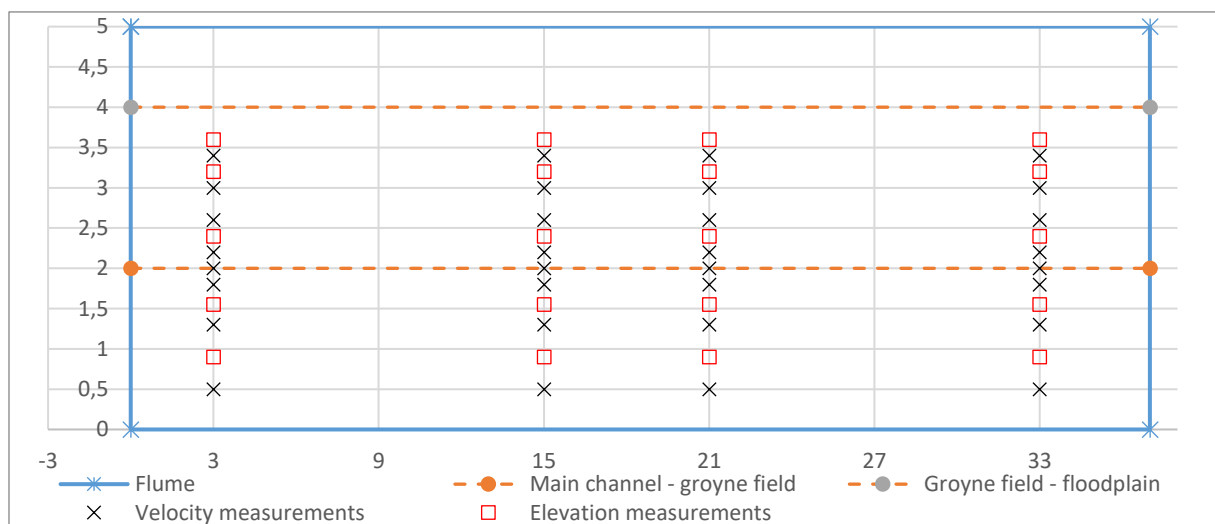


Figure 51; Location the measurement points of the cross sections for the simulations without groynes with a water depth of 24 cm. The axes are in [m]. In blue the area measured with the PTV.

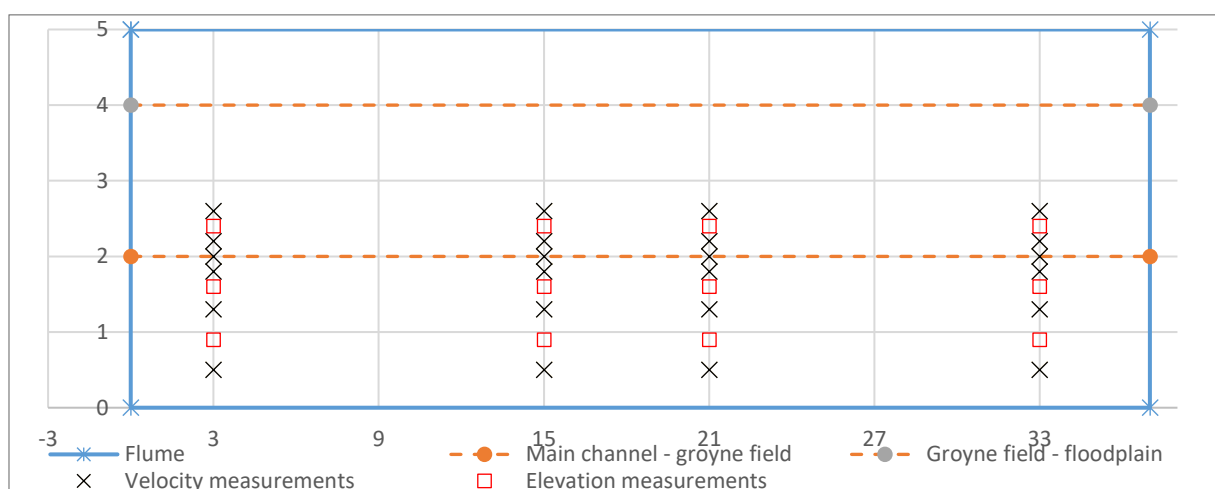


Figure 52; Location the measurement points of the cross sections for the simulations without groynes with a water depth of 18 cm. The axes are in [m]. In blue the area measured with the PTV.

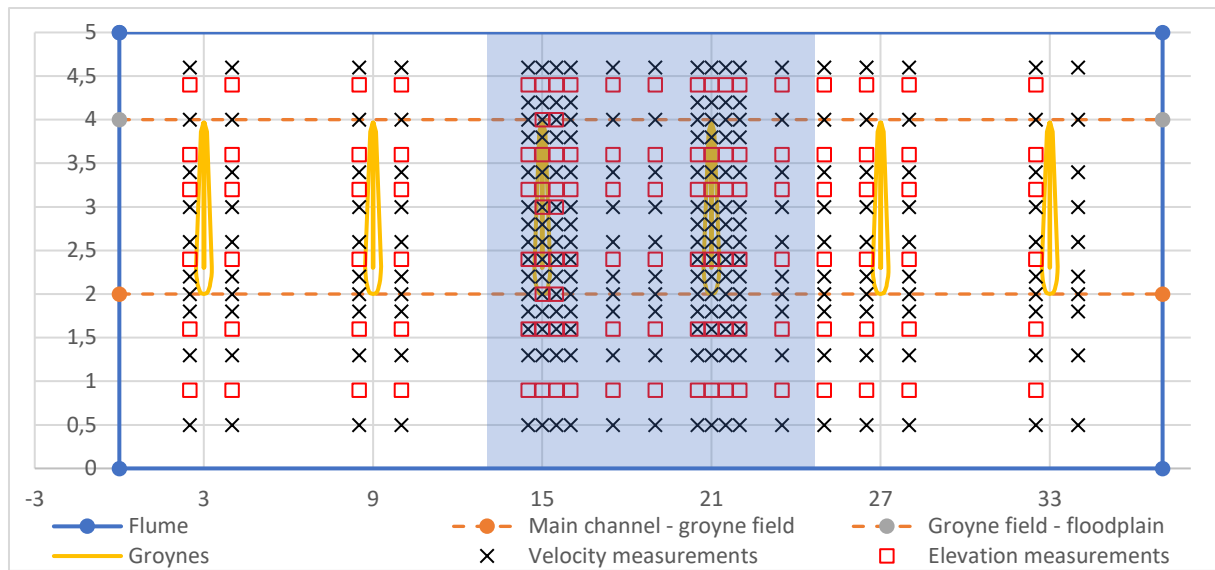


Figure 53; Location the measurement points of the cross sections for the simulations with groynes with water depths of 30, 35 and 40 cm. The axes are in [m]. In blue the area measured with the PTV.

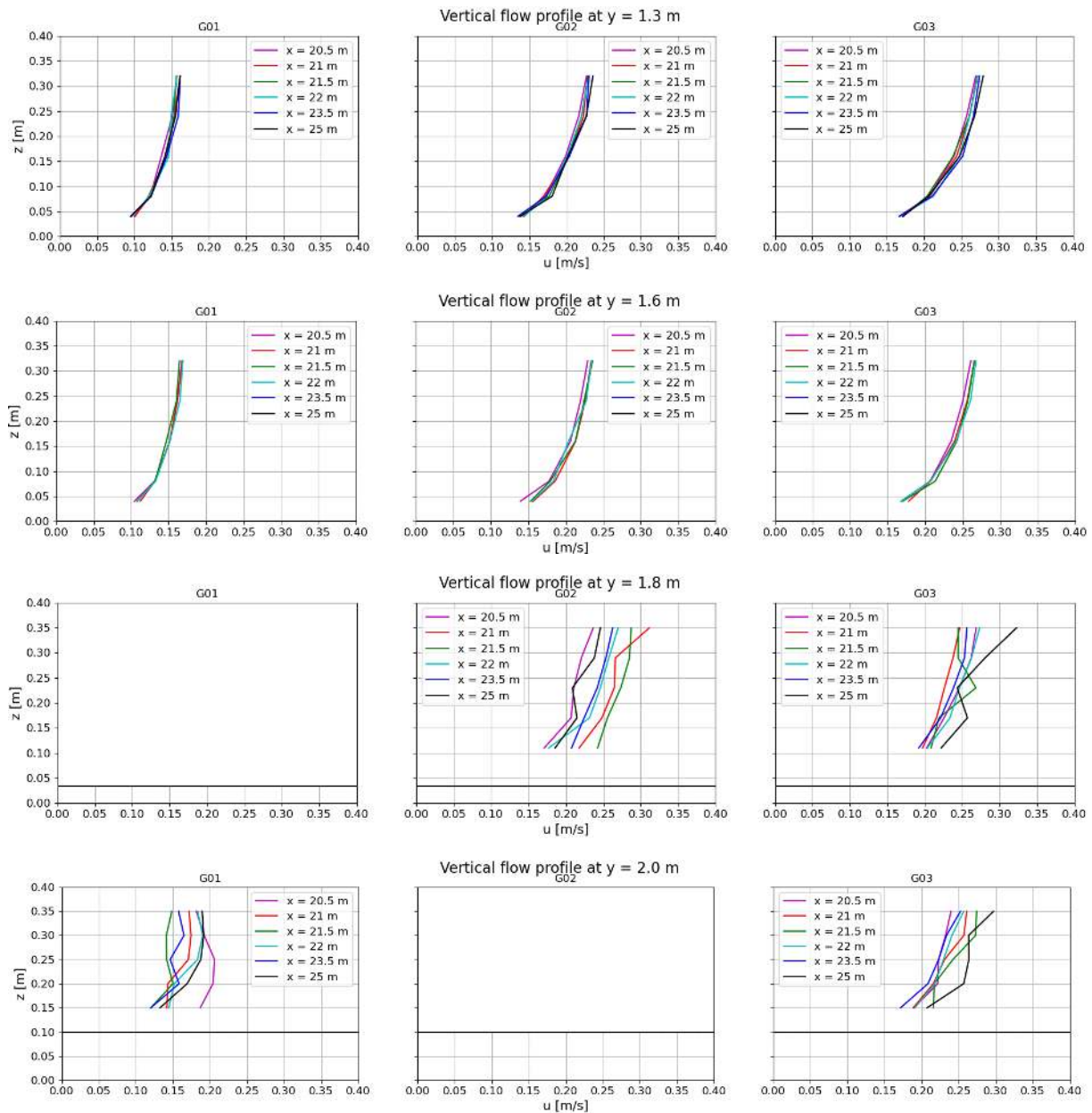
## Appendix C

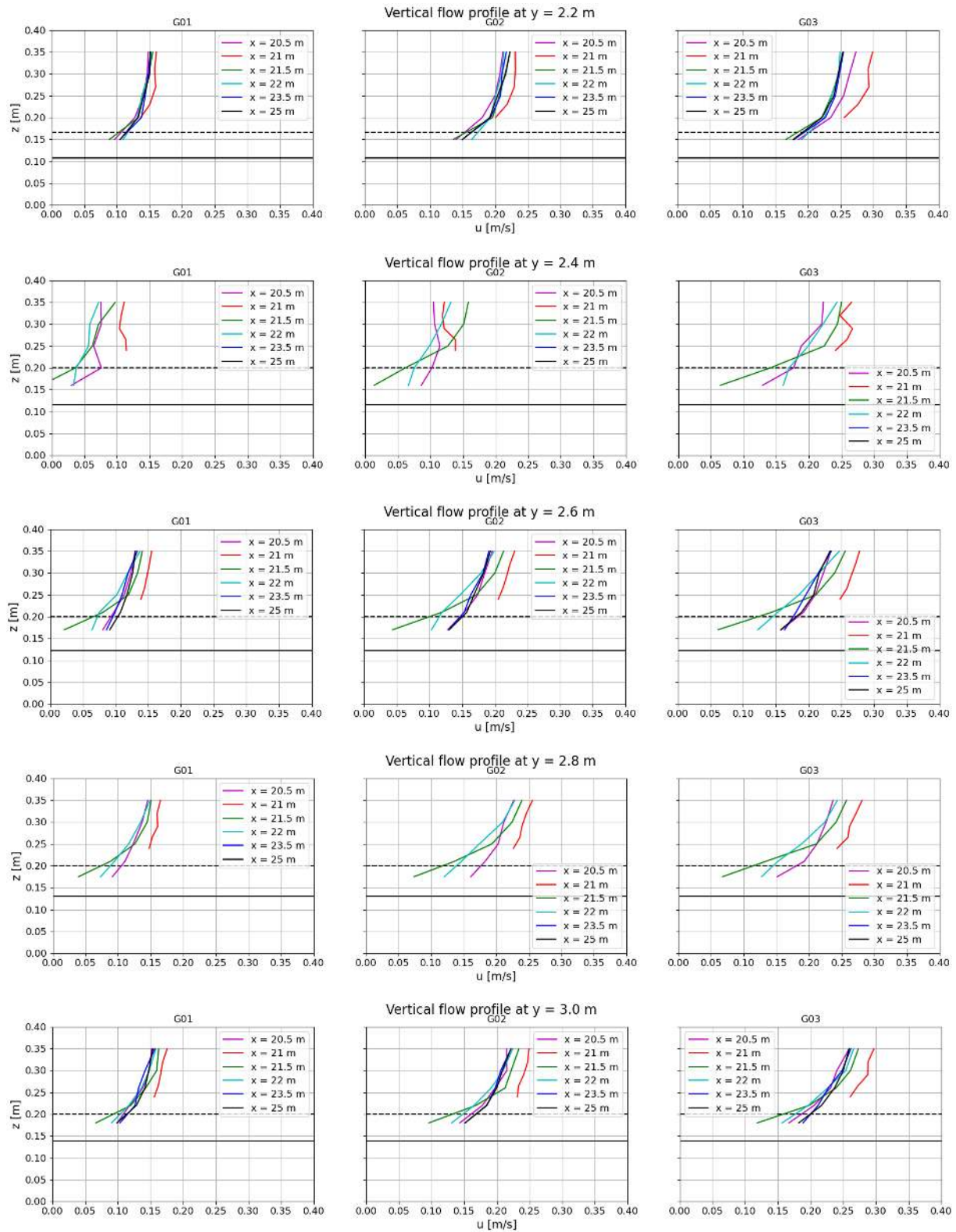
### Streamwise velocities and relative fluctuations in flow over groyne

This appendix shows all the relevant quantities measured with the EMS around the groyne. These relevant quantities are the streamwise velocities and the turbulent fluctuations. The results are shown for the three different cases G01 – G03 for the measured transects at  $x = 20.5$ ; 21; 21.5; 22; 23.5; 25 m.

The flow profiles at  $y = 1.8$  and  $y = 2.0$  were measured with the oldest EMS, which on some of the measurement days didn't perform well due to construction work next to the flume. These construction works gave large peaks in the electrical input signal, which the oldest devices were sensitive to. Results from those days from those devices have been excluded from the graphs.

#### Vertical flow profiles







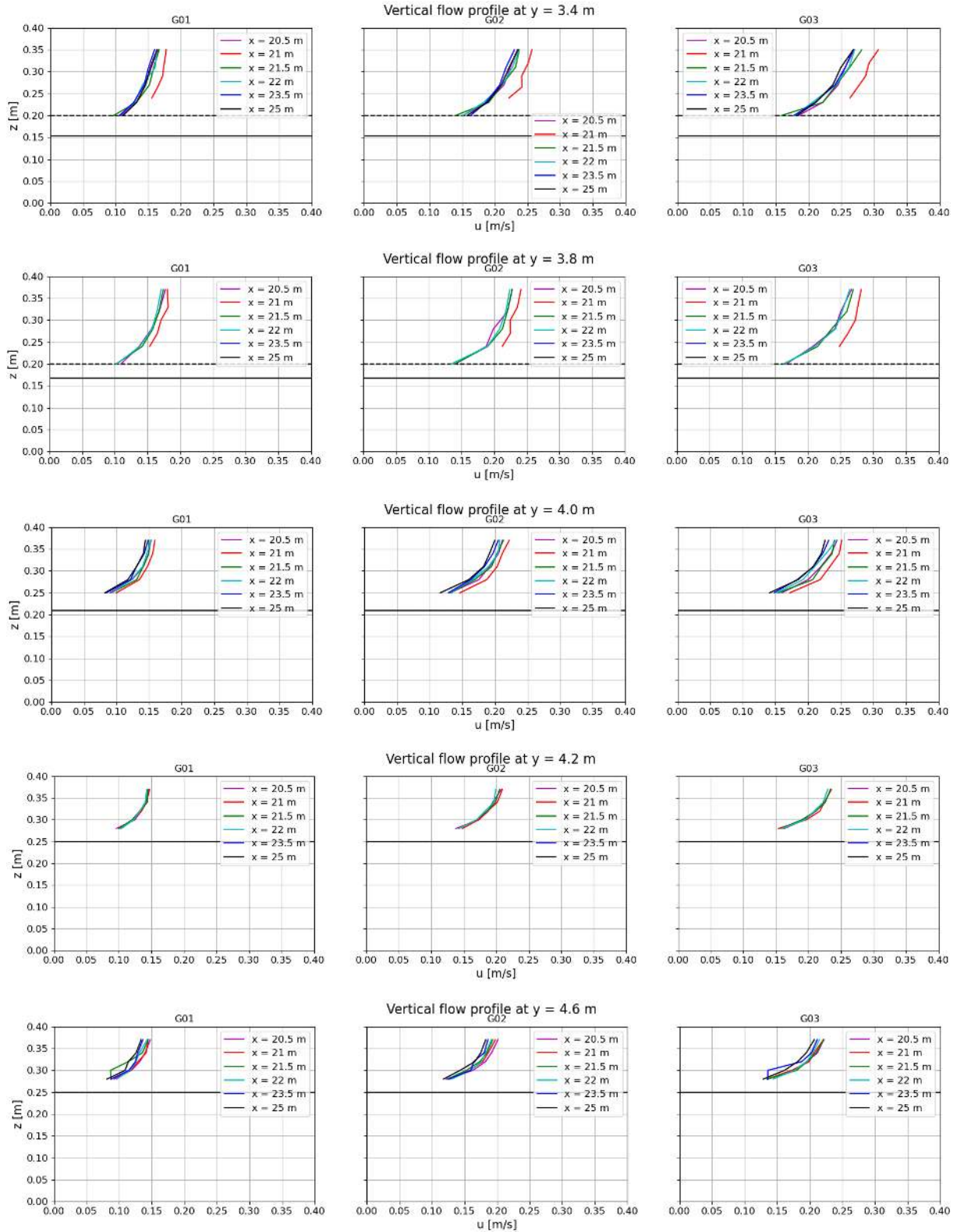
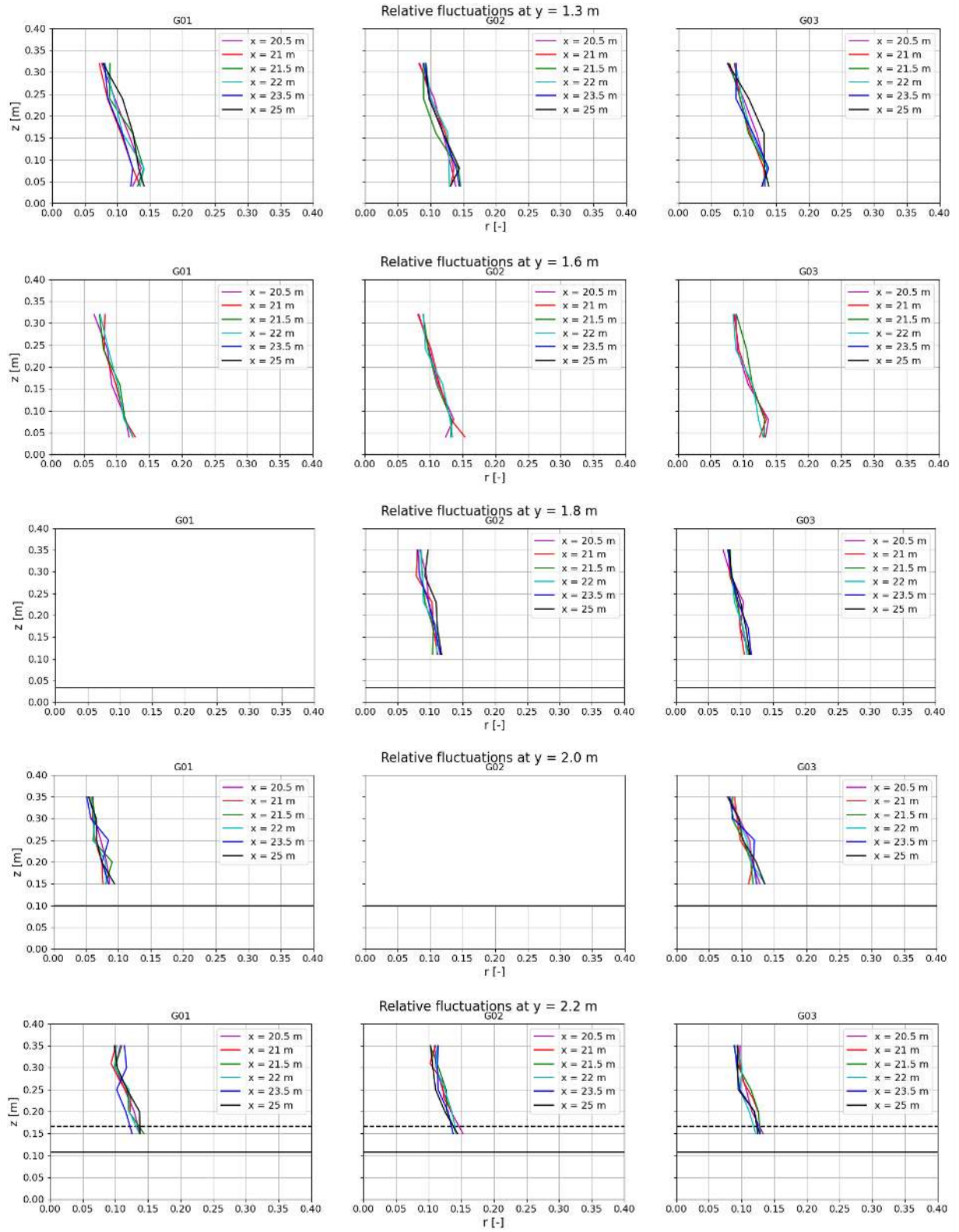
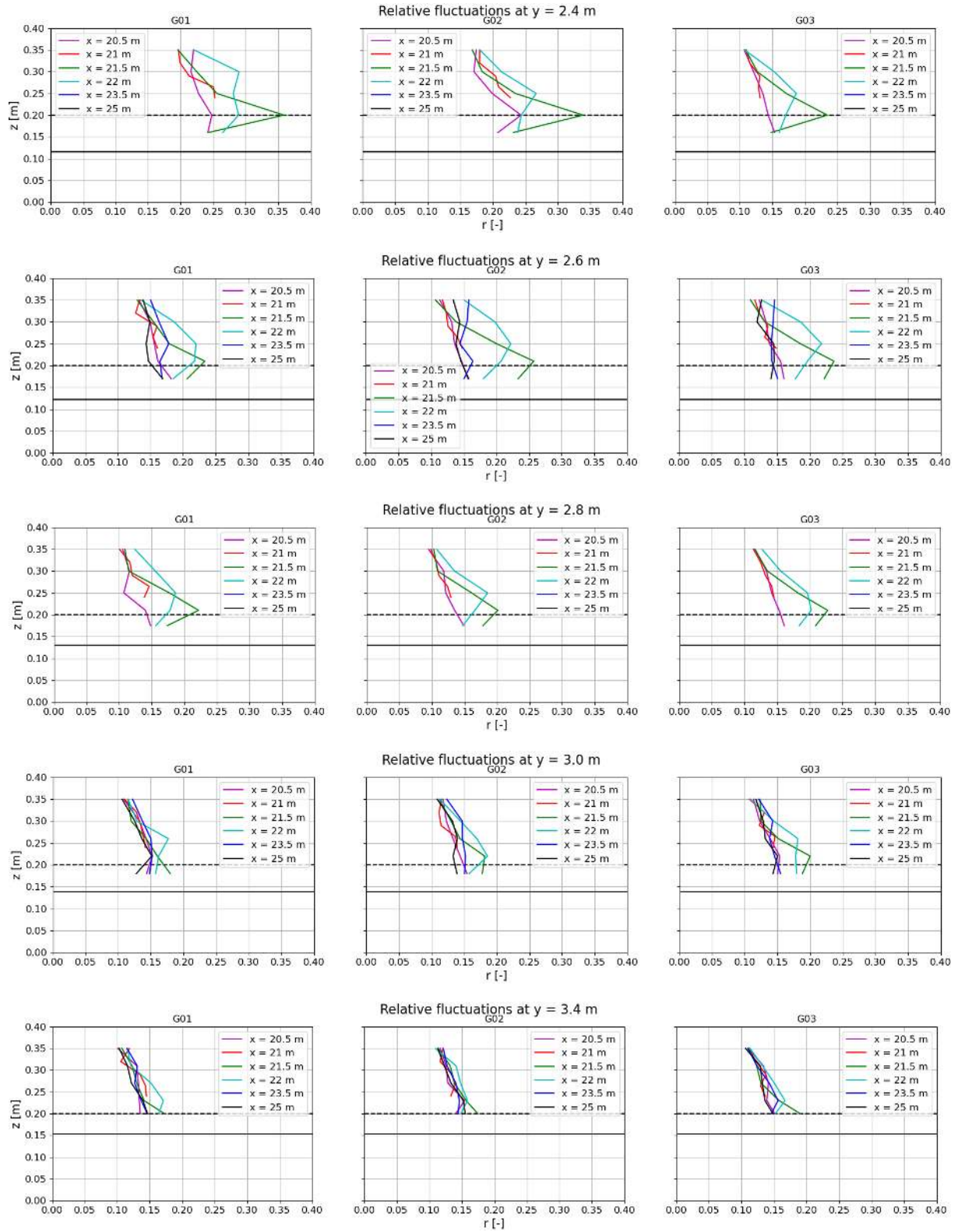


Figure 54; Vertical velocity profiles from  $x = 20.5$  m to  $x = 25$  m. From just upstream of the fourth groyne to far downstream. The bed level is shown in as a black line. The groyne height is showed as a black dotted line.

## Relative turbulent fluctuations





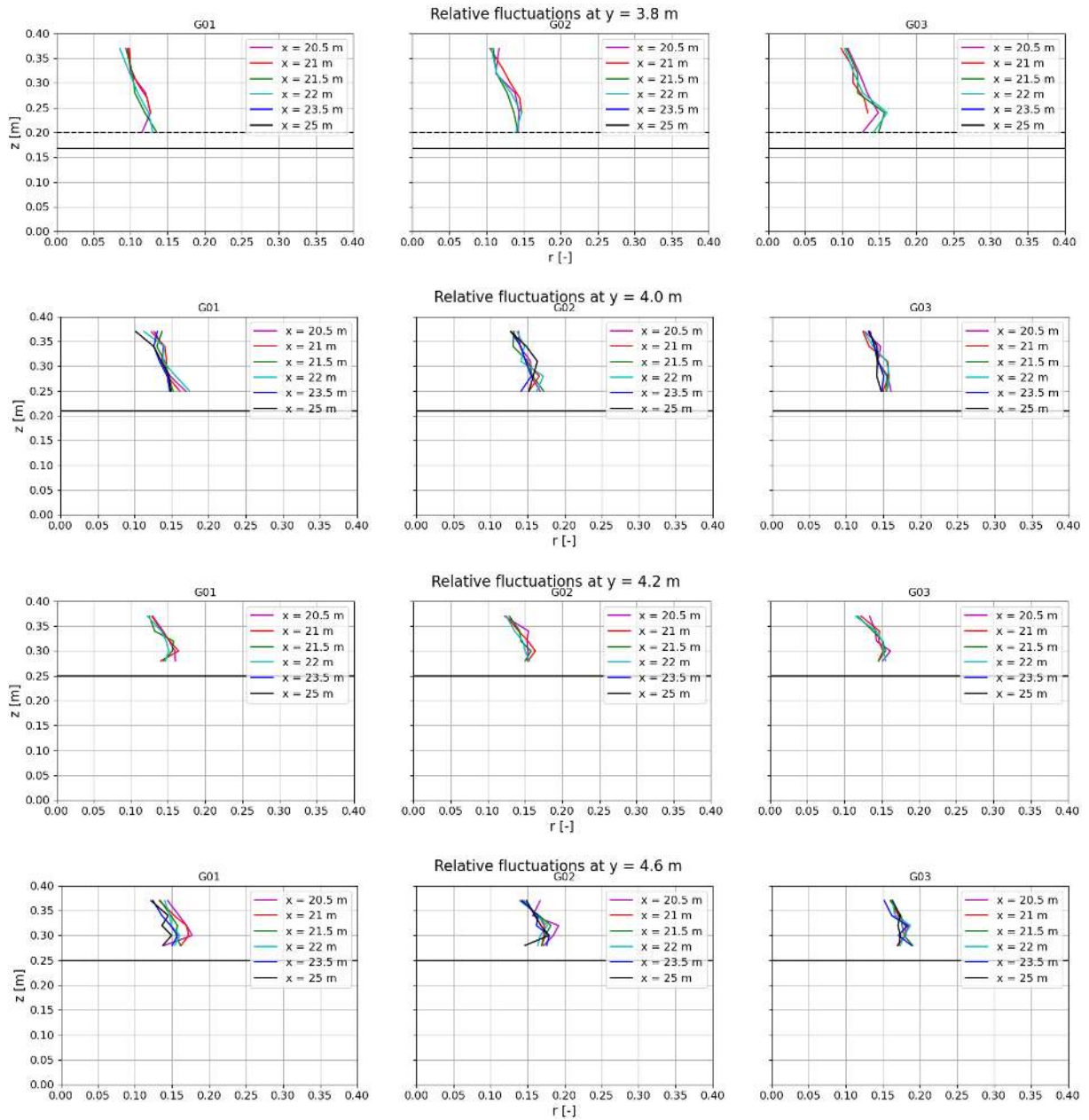


Figure 55; Relative fluctuation from  $x = 20.5$  m to  $x = 25$  m. From just upstream of the fourth groyne to far downstream. The bed level is shown in as a black line. The groyne height is showed as a black dotted line. The fluctuations are normalized on the depth average flow velocity at  $x = 21$  m, the location of the groyne.



## Appendix D

### Influence of the boundary conditions

Before describing the observed flow it is important to quantify the effect of the boundary conditions on the model. It was already mentioned by Chavarrias et al. (2019) that the discharge distribution at the inflow greatly influences the lateral distribution of the discharge and its uniformity over the flume length. The result of pilot testing therefore was an blockade of the inflow. The blockade is 30 cm high at the floodplain and linearly decreasing in height till the edge of the groyne field to a height of 10 cm for the case without groyne, as shown in Figure 56. For the case with groynes the geometry of the groyne is constructed in front of the inflow.

The resulting uniformity of the lateral distribution of the discharge is investigated in this appendix.

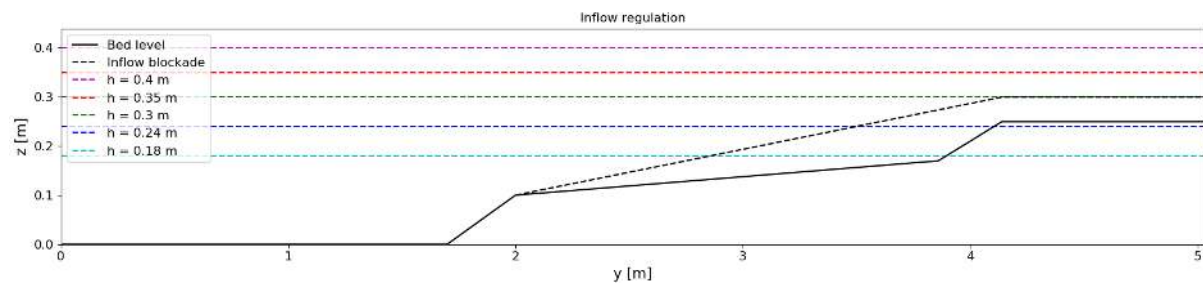


Figure 56; Discharge regulation by blockading part of the inflow

#### Lateral distribution of discharge

In Figure 57 the streamwise development of the lateral distribution of discharge is showed for all simulations, with equal water levels in the same subgraph. There is an overall pattern of decreasing flow velocity in the floodplain and an increasing flow velocity in the main channel. The inflow conditions consistently don't agree with the downstream conditions with too much water entering the domain at the floodplain. This is even the case for water levels of 0.3 m and lower, where the inflow is blockaded almost completely at the floodplain of groyne field. In these cases the lateral distribution of discharge does however adapt within a reasonable length, such that from the lateral distribution of discharge can be assumed constant from 21 m downstream if the inflow. For the highest water levels of 0.35 m and 0.4 m the lateral distribution of discharge does not adapt fully for the case without groynes, for which the effect is largest for the highest water levels. For the case with groynes also the lateral distribution of discharge can be assumed constant from 21 m downstream if the inflow.

The consequence of a constant lateral distribution of discharge is that the average transverse flow velocity  $V = 0$ , such that in the depth averaged shallow water equations all terms containing  $V$  can be dropped confidently. This is the case for simulations E07 – E13 and G01 – G03. For the simulations E01 – E06 the mean flow profile at the downstream end is used as a best approximation of the situation of a constant lateral distribution of discharge.

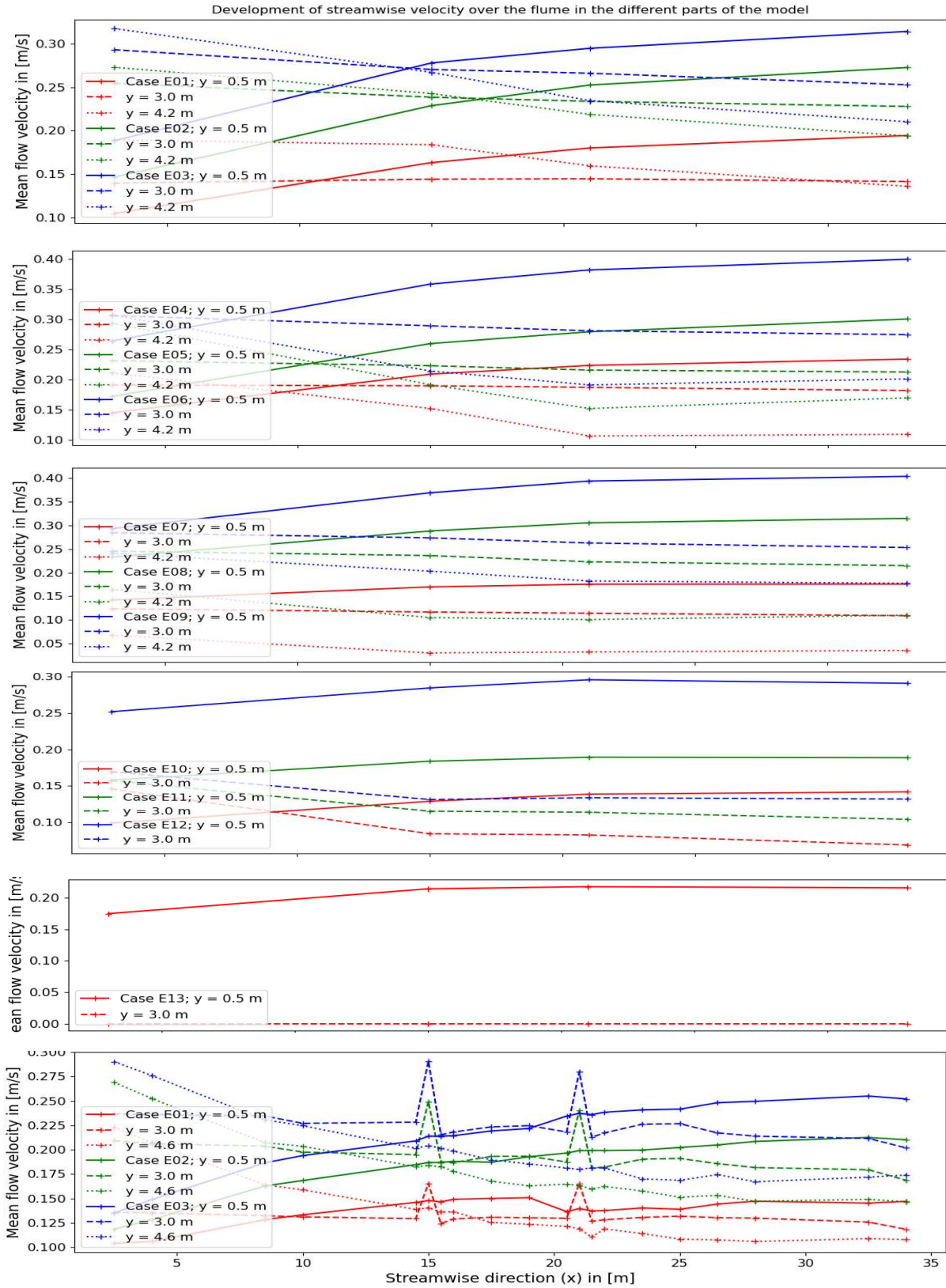


Figure 57; Development of the mean flow velocity in the main channel, groyne field and floodplain for all cases. Cases E01 – E03 in figure a; E04 – E06 in figure b; E07 – E09 in figure c; E10 – E12 in figure d; E13 in figure e; G01 – G03 in figure f



## Appendix E

### Data of groyne discharge coefficients

Groyne	$H_1$ [m]	$C_d$ [-]	$H_3/H_1$ [-]	$q$ [m <sup>2</sup> /s]	$h_g$ [m]	$y$ [m]
1	0,1787	0,2721	1,0013	0,0351	0	2
1	0,1782	0,2658	1,0010	0,0341	0,059	2,2
1	0,1780	0,2217	0,9993	0,0284	0,077	2,6
1	0,1792	0,2457	0,9980	0,0318	0,062	3
1	0,1797	0,2594	0,9944	0,0337	0,047	3,4
1	0,1787	0,1896	0,9952	0,0244	0	4
2	0,1788	0,2657	0,9992	0,0343	0	2
2	0,1781	0,2550	0,9994	0,0327	0,059	2,2
2	0,1779	0,2022	0,9980	0,0259	0,077	2,6
2	0,1788	0,2402	0,9990	0,0310	0,062	3
2	0,1785	0,2427	0,9991	0,0312	0,047	3,4
2	0,1779	0,1758	0,9985	0,0225	0	4
3	0,1808	0,2773	1,0007	0,0363	0	2
3	0,1790	0,2515	1,0000	0,0325	0,059	2,2
3	0,1769	0,1387	0,9987	0,0176	0,085	2,4
3	0,1775	0,1581	0,9981	0,0202	0,077	2,6
3	0,1781	0,2150	0,9987	0,0275	0,07	2,8
3	0,1785	0,2220	0,9987	0,0285	0,062	3
3	0,1783	0,2367	0,9996	0,0304	0,047	3,4
3	0,1772	0,2473	0,9996	0,0314	0,032	3,8
3	0,1765	0,1757	0,9994	0,0222	0	4
4	0,1818	0,3558	0,9991	0,0470	0	2
4	0,1786	0,2798	1,0008	0,0360	0,059	2,2
4	0,1759	0,1043	0,9990	0,0131	0,085	2,4
4	0,1769	0,1938	0,9990	0,0246	0,077	2,6
4	0,1777	0,2130	0,9994	0,0272	0,07	2,8
4	0,1784	0,2348	1,0001	0,0302	0,062	3
4	0,1774	0,2348	0,9999	0,0299	0,047	3,4
4	0,1766	0,2321	1,0004	0,0294	0,032	3,8
4	0,1760	0,1573	1,0015	0,0198	0	4
5	0,1785	0,4896	1,0059	0,0629	0	2
5	0,1771	0,2886	1,0002	0,0367	0,059	2,2
5	0,1766	0,1887	0,9985	0,0239	0,077	2,6
5	0,1776	0,2395	0,9994	0,0306	0,062	3
5	0,1774	0,2349	0,9988	0,0299	0,047	3,4
5	0,1761	0,1552	0,9988	0,0195	0	4
6	0,1775	0,2845	1,0005	0,0363	0	2
6	0,1769	0,2898	1,0005	0,0368	0,059	2,2
6	0,1764	0,1815	0,9989	0,0229	0,077	2,6
6	0,1773	0,2177	0,9995	0,0277	0,062	3
6	0,1770	0,2282	0,9999	0,0290	0,047	3,4
6	0,1757	0,1504	1,0002	0,0189	0	4
1	0,1808	0,3605	1,0009	0,0472	0	2
1	0,1805	0,4127	1,0017	0,0540	0,059	2,2
1	0,1806	0,3587	0,9982	0,0469	0,077	2,6
1	0,1817	0,3730	0,9981	0,0493	0,062	3
1	0,1811	0,4008	0,9986	0,0527	0,047	3,4
1	0,1803	0,2707	0,9966	0,0353	0	4
2	0,1810	0,3900	0,9981	0,0512	0	2
2	0,1803	0,4000	0,9992	0,0522	0,059	2,2
2	0,1801	0,3075	0,9955	0,0401	0,077	2,6

2	0,1811	0,3563	0,9974	0,0468	0,062	3
2	0,1801	0,3571	0,9981	0,0465	0,047	3,4
2	0,1792	0,2439	0,9973	0,0315	0	4
3	0,1825	0,4174	1,0010	0,0555	0	2
3	0,1808	0,3768	0,9991	0,0494	0,059	2,2
3	0,1785	0,2272	0,9964	0,0292	0,085	2,4
3	0,1793	0,2658	0,9957	0,0344	0,077	2,6
3	0,1800	0,3292	0,9973	0,0429	0,07	2,8
3	0,1805	0,3318	0,9971	0,0434	0,062	3
3	0,1793	0,3420	0,9991	0,0443	0,047	3,4
3	0,1785	0,3193	0,9991	0,0410	0,032	3,8
3	0,1791	0,2385	0,9982	0,0308	0	4
4	0,1810	0,1798	0,9977	0,0236	0	2
4	0,1801	0,3999	1,0001	0,0521	0,059	2,2
4	0,1769	0,1970	0,9986	0,0250	0,085	2,4
4	0,1784	0,2894	0,9978	0,0372	0,077	2,6
4	0,1795	0,3286	0,9973	0,0426	0,07	2,8
4	0,1800	0,3306	0,9993	0,0430	0,062	3
4	0,1782	0,3363	0,9995	0,0431	0,047	3,4
4	0,1774	0,3055	0,9998	0,0389	0,032	3,8
4	0,1780	0,2151	0,9999	0,0275	0	4
5	0,1772	0,1877	1,0016	0,0239	0	2
5	0,1782	0,4006	1,0006	0,0514	0,059	2,2
5	0,1775	0,2769	0,9979	0,0353	0,077	2,6
5	0,1788	0,3304	0,9986	0,0426	0,062	3
5	0,1778	0,3338	0,9987	0,0427	0,047	3,4
5	0,1756	0,2066	0,9984	0,0259	0	4
6	0,1722	0,3398	0,9898	0,0414	0	2
6	0,1689	0,4178	0,9873	0,0494	0,059	2,2
6	0,1682	0,2644	0,9836	0,0311	0,077	2,6
6	0,1753	0,3113	0,9933	0,0390	0,062	3
6	0,1772	0,3259	0,9987	0,0414	0,047	3,4
6	0,1749	0,2164	0,9999	0,0270	0	4
1	0,1817	0,3844	1,0013	0,0508	0	2
1	0,1819	0,4802	1,0027	0,0635	0,059	2,2
1	0,1830	0,4245	0,9943	0,0567	0,077	2,6
1	0,1845	0,4190	0,9937	0,0566	0,062	3
1	0,1847	0,4736	0,9963	0,0641	0,047	3,4
1	0,1824	0,3051	0,9953	0,0405	0	4
2	0,1819	0,4176	0,9976	0,0552	0	2
2	0,1815	0,4622	0,9995	0,0609	0,059	2,2
2	0,1815	0,3740	0,9950	0,0493	0,077	2,6
2	0,1828	0,4047	0,9963	0,0539	0,062	3
2	0,1829	0,4286	0,9968	0,0572	0,047	3,4
2	0,1810	0,2743	0,9964	0,0360	0	4
3	0,1827	0,4474	1,0012	0,0596	0	2
3	0,1817	0,4394	0,9990	0,0580	0,059	2,2
3	0,1798	0,2865	0,9942	0,0372	0,085	2,4
3	0,1806	0,3228	0,9942	0,0422	0,077	2,6
3	0,1812	0,3529	0,9957	0,0464	0,07	2,8
3	0,1821	0,3778	0,9956	0,0500	0,062	3
3	0,1816	0,4071	0,9993	0,0537	0,047	3,4
3	0,1801	0,3695	0,9991	0,0481	0,032	3,8
3	0,1791	0,2660	0,9989	0,0344	0	4
4	0,1827	0,4677	1,0003	0,0622	0	2
4	0,1816	0,4620	0,9977	0,0609	0,059	2,2
4	0,1789	0,3993	1,0006	0,0515	0,085	2,4
4	0,1798	0,3511	0,9970	0,0457	0,077	2,6

4	0,1804	0,3490	0,9976	0,0456	0,07	2,8
4	0,1814	0,3911	0,9991	0,0515	0,062	3
4	0,1804	0,3857	0,9994	0,0504	0,047	3,4
4	0,1790	0,3552	1,0005	0,0459	0,032	3,8
4	0,1784	0,2449	1,0002	0,0315	0	4
5	0,1817	0,4997	0,9942	0,0660	0	2
5	0,1796	0,4610	1,0004	0,0598	0,059	2,2
5	0,1790	0,3278	0,9963	0,0423	0,077	2,6
5	0,1804	0,3871	0,9980	0,0505	0,062	3
5	0,1800	0,3772	0,9975	0,0491	0,047	3,4
5	0,1784	0,2443	0,9979	0,0314	0	4
6	0,1791	0,4027	0,9990	0,0521	0	2
6	0,1790	0,4708	1,0006	0,0608	0,059	2,2
6	0,1783	0,3239	0,9965	0,0416	0,077	2,6
6	0,1796	0,3668	0,9976	0,0476	0,062	3
6	0,1791	0,3786	0,9984	0,0489	0,047	3,4
6	0,1774	0,2482	1,0000	0,0316	0	4

## Appendix F

### Observation of flow without groynes

To gain insight in the flow dynamics of the case without groynes the water levels, depth averaged flow velocities and the relative turbulence at the surface and the autocorrelation at specific points in the mixing layer are shown for the cases E01 to E13 in Figure 58 – Figure 62.

#### Observed uncertainties in measurements

The observed depth averaged velocity profiles are limited to  $y = 4.2$  m, due to the malfunctioning of the sixth device, due to a great sensitivity to the proximity of other devices electric signal. This device also measured at  $y = 4.0$  m, in the centre of the mixing layer between the groyne field and floodplain.

The fifth device, measuring at  $y = 3.6$  m and  $y = 4.2$  m prove sensitive to its position in the transverse. This induced an uncertainty of approximately 0.5 V on the measured velocities at  $y = 4.2$  m. In total very few and very uncertain information is available on the flow velocities in the floodplain for all cases without groynes.  $y = 3.8$  m and  $y = 5$  m there is one useful vertical velocity profile at  $y = 4.2$  m, which has a possible zero error of 0.5 V, or close to 0.05 m/s.

Manufacturing standards of the EMS state that the daily drift of the signal is at most 0.1 V. The observed daily drift of the signal is up to 0.2 V however. The uncertainty with the used EMS is therefore large. Calibration of the EMS that was performed after the measurements were done, showed that all EMS measured higher flow velocities that should be. The errors were for that reason damped slightly by the calibration of the EMS.

#### Water level slopes

Figure 58 shows the water level for the cases E01-E13. For all plots the measured water levels are normalized per streamwise section to match each other either  $x = 21$  m (cases E). This to be able to see trends more easily. It prove not possible to quantify the exact influence of mounting the different devices at different locations over the transverse, as explained in Chapter 3.2.1. There is a mean flow toward the main channel in the upstream part if the model. There is a lateral water level slope expected therefore. This isn't observable however with uncertainty over the lateral direction.

The water levels scale with the discharge and the water depth, as expected from flow where the bed shear stress is the dominant energy sink.

#### Mean flow in the channel compounds

The depth average velocity in the channels scales well with the water depth and the discharge in the main channel and groyne field, which indicated that a basic balance between the pressure gradient and the bed shear stress can describe the flow in those parts of the transect well.

#### Main channel – groyne field mixing layer

In the mixings layer a gradual change in depth average velocity is expected. Furthermore a large turbulence is expected due to lateral shear and eddies should be visible in the auto-correlation function of the transverse velocity. These are all properties of shear flow.

The large eddies were not observed by eye nor dye. Large eddies are also not visible in the auto-correlation function of the transverse signal in the mixing layer in Figure 62. There is no significant difference between the auto-corelation functions in the middle of the channel compounds and the mixing layers. There is some periodicity observed in the floodplain. The timescale is very small however, and does not represent eddies with a characteristic length of the flow depth or width of the mixing layer. The observed periodicity is best explained by the surface waves.

The relative turbulence is slightly increased in the mixing layer. This either indicates lateral shear as an consequence of a velocity gradient, or it is only an effect of an unexpected lower flow velocity in the mixing layer.

The observed velocity difference between the main channel and groyne field is small. This can explain the lack of large eddies forming, with only very weak lateral shear.

The flow velocities in the mixing layer are lower than the flow velocities around them, which does not comply with the expected flow velocity from the contribution of bed friction and lateral shear. This is possibly an effect of secondary circulations, where flow from the bottom of the main channel of groyne field rise towards the surface in the mixing layer, slowing the flow down.

#### No flow velocity in floodplain and groyne field

For a water level of 0.3 m the flow velocity reduces to zero in the floodplain (the floodplain is submerged with 0.05 m water). The floodplain stops contributing to the conveyance capacity of the flume. For E13, with  $h = 0.21$  m something similar seems to hold, but now the groyne field stops contributing to the discharge capacity of the cross section.

This cannot be explained with only bed shear and a pressure gradient and indicates the effect of secondary circulations, which shuts down the discharge through those very shallow parts of the channel.

#### Conclusion on physical processes in model without groynes

The main processes in the physical model are the pressure gradient in balance with the bed shear stress. From analysis of the mixing layer it follows that the exchange in the mixing layer is rather small. Because of the small differences between the flow velocity in the main channel and the groyne field and the existence of a region of low flow in the mixing layer as a secondary effect, it can be challenging to estimate parameters that govern the exchange of momentum in a horizontal shear layer based on the current measurements. There is no clear indication on the actual width of the mixing layer for this reason, and no clear point to fit the parameter  $\beta$  on in equation (20). There are some flow processes that indicate a considerable influence of secondary circulations. Furthermore, the flow velocities in the main channel, groyne field and floodplain consistent within a channel compound. This allows the estimation of different flow terms in a compound channel model. Most important is the estimation of bed shear stress parameters. Preferably an estimate for the influence of secondary circulations is made, with the estimation of values of  $\Gamma$  as in equation (14).

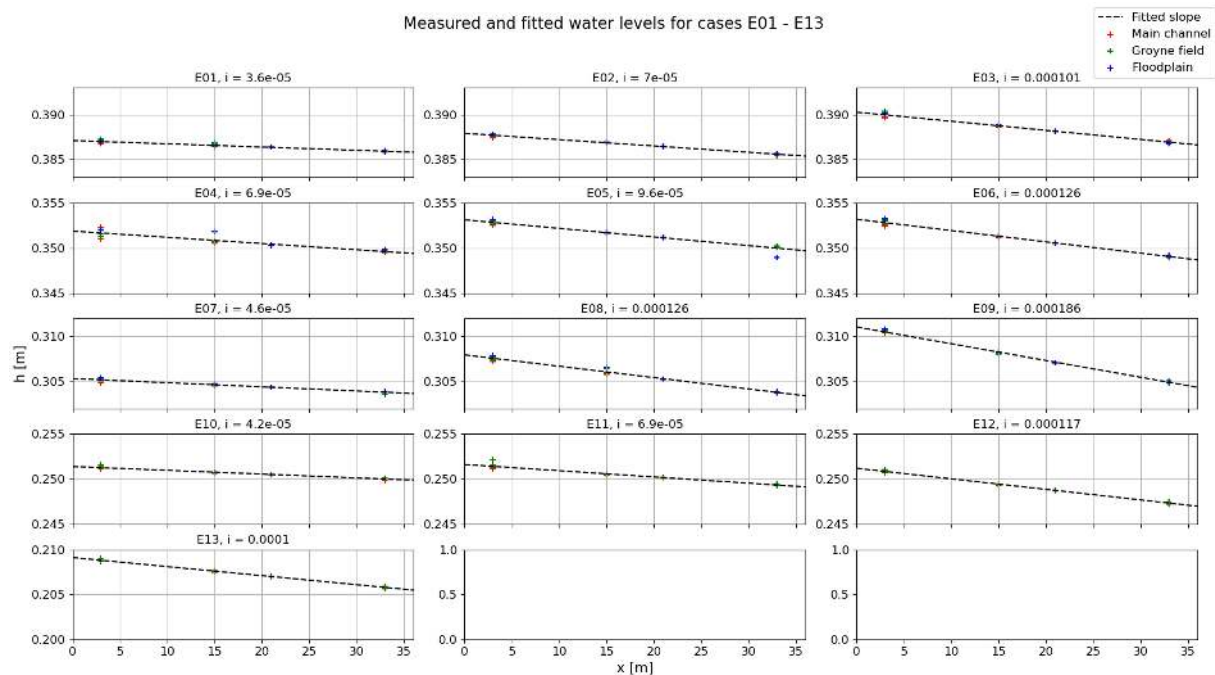


Figure 58; Measured water level slopes for cases E01-E13 without groynes

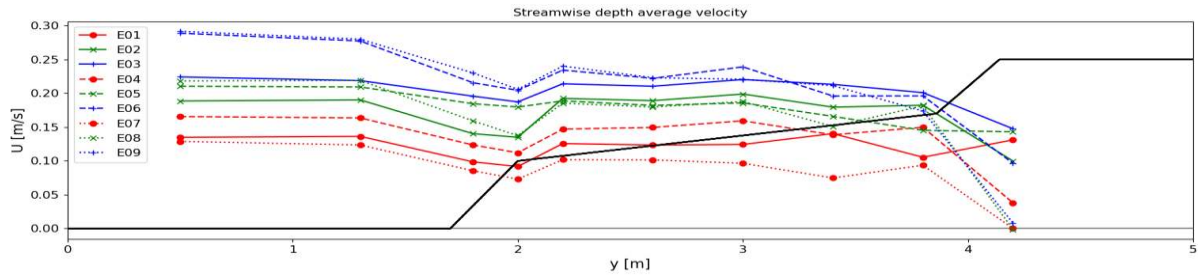


Figure 59; Depth average velocity for the cases E01 – E09. Colors correspond to similar Froude numbers in the simulation. Line styles correspond to different water levels.

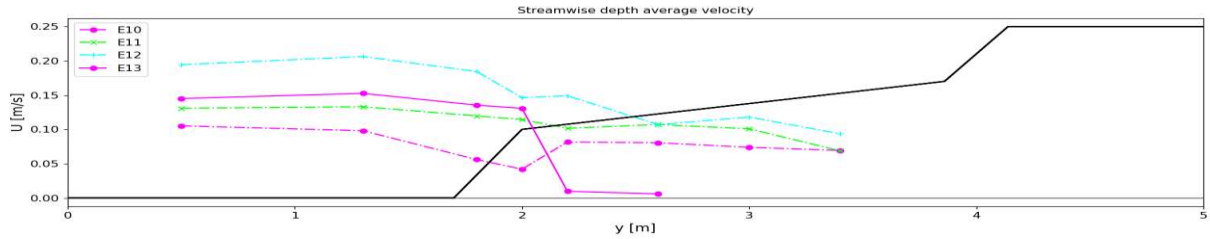


Figure 60; Depth average velocity for the cases E10 – E13

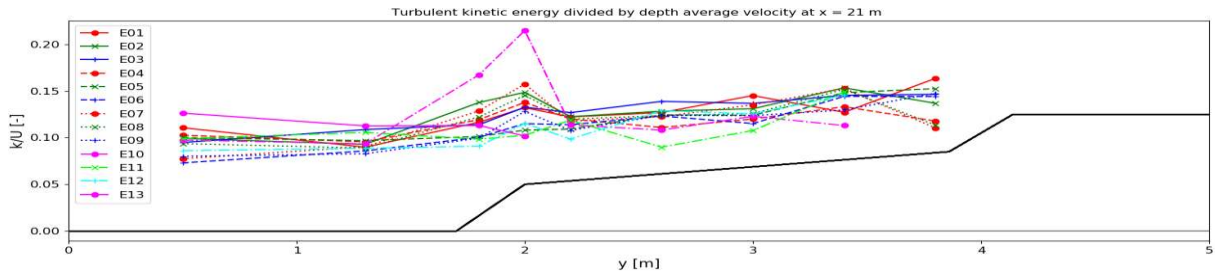


Figure 61; Relative turbulence for the cases E01 – E13

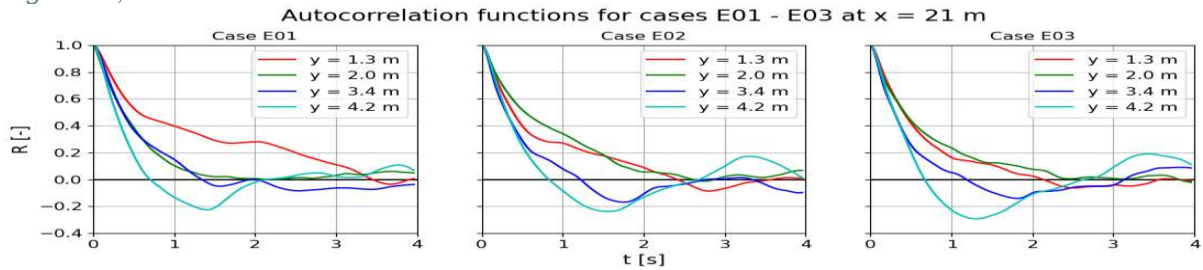


Figure 62; Autocorrelation function of transverse velocity component at  $x = 21$  m for different places in the transverse for case E01 – E03

## Appendix G

### Fitting of bed roughness on the cases E01 – E13 to measured average flow using a 1D compound channel model

For the analysis of the groyne resistance it is of importance to have an estimate of the bed shear stress. Obtaining the influence of the bed shear stress also allows estimating the influence the effect of other processes such as the lateral shear and secondary circulations. Appendix shows the derivation of the theoretical bed shear stress from the logarithmic flow profile in the parts of the flume where the flow can be considered fully developed. This gave  $k_s = 0.068 \pm 0.031$  m. This roughness height should be the starting point of any analytical model.

The compound channel model is solved equation (34) for each channel, assuming that the water level slope in each channel is equal and that the total discharge is the sum of the discharges in the channels. The most simplified form of the compound channel model includes a balance between the water level slope, the bed shear stress and the advection, and solves four equations to obtain the water level slope and the flow velocities in the different channels:

$$Q = B_{mc} d_{mc} U_{mc} + B_{gf} d_{gf} U_{gf} + B_{fp} d_{fp} U_{fp} \quad (68)$$

$$-\frac{\partial h}{\partial x} = \left( \frac{g}{C_{mc}^2} Fr_{mc}^2 + \frac{d_{mc}}{B_{mc}} \frac{g}{C_{wall}^2} Fr_{mc}^2 \right) \frac{1}{1 - Fr_{mc}^2} \quad (69)$$

$$-\frac{\partial h}{\partial x} = \left( \frac{g}{C_{gf}^2} Fr_{gf}^2 \right) \frac{1}{1 - Fr_{gf}^2} \quad (70)$$

$$-\frac{\partial h}{\partial x} = \left( \frac{g}{C_{fp}^2} Fr_{fp}^2 + \frac{d_{fp}}{B_{fp}} \frac{g}{C_{wall}^2} Fr_{fp}^2 \right) \frac{1}{1 - Fr_{fp}^2} \quad (71)$$

To include the effect of the side walls a roughness height  $k_{s,wall} = 6.27 \cdot 10^{-4}$  m is chosen, equivalent to roughness values used by Yossef (2005) as the same flume is used. One difference between both experiments is the bed roughness is different, but not the side wall roughness. This value of  $k_s$  for the considered range of water depths also correspond to roughness values of smooth concrete panels, with Manning  $n = 0.011 - 0.013$  (Arcement, 1989). With the given value of  $k_s$ ,  $C$  is determined using Colebrook-White (equation (12)).

The compound channel model uses a simplified form of the physical model, taking the average depth of the sloping groyne field, and taking the average depth of the groyne crest height, and neglects the slopes between the different channels, as showed in Figure 63.

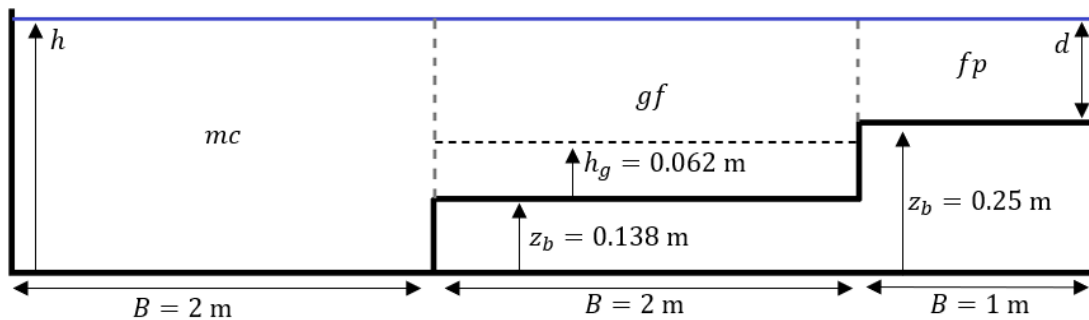


Figure 63; Overview of analytical compound channel model, not to scale. The depth of the groyne field is the average depth in the groyne field. The groyne crest is at 0.2 m above reference, so that  $h_g = 0.062$  m. Simplification of the analytical model includes neglecting the bed slope in the groyne field, neglecting the gradual transition between channel compounds and neglecting the groyne tip.



Using  $k_s = 0.068 \pm 0.031$  m for the bed roughness one would obtain the water level slopes as shown in Figure 64. The predicted water level slopes do not correspond to the measured water level slopes and would give very large water level slopes. It would be difficult to get the water level slopes better predicted including more physical processes such as the secondary circulations and the lateral exchange in the horizontal mixing layers. *Figure 59* however indicates a pronounced influence of the secondary circulations, which should generally exist in a compound channel (Shiono & Knight, 1991). Secondary circulations in the flow make that the flow is no longer one-dimensional, which was the assumption fitting the roughness height based on the Law of the Wall. For that reason it is reasonable to recalibrate the roughness height on the measured average flow in the physical model. Doing so makes the roughness height an empirical fitting factor. It should however be related to the size of the gravel  $D_{50} = 8$  mm. This would mean that  $k_s$  should be lower than the value found in Appendix and larger than  $2D_{90} = 16$  mm. This last constrain is due to the spreading of the particles, where the large spacing between the particles mean that each particle is a larger obstacle to the flow compared to the situation for which values of  $k_s$  are commonly determined, with a densely packed bed.

The optimal value for the bed roughness can be found integrating all terms in the momentum balance over the width:

$$-\frac{\partial h}{\partial x} = \frac{\sum B_i \frac{g}{C_i^2} Fr_i^2}{\sum B_i (1 - Fr_i^2)} \quad (72)$$

The obtained value of  $k_s = 0.032 \pm 0.015$  m. Figure 65 shows the predicted water levels using this roughness height. Figure 66 shows the predicted discharge distribution. For the cases with a higher water level the model predicts the water level slopes well, while not predicting the discharge distributions right. This is the other way around for the cases with a lower water level.

This indicates that other processes play a role besides the bed shear stress. One important process to include might be the effect of secondary circulations. Determining secondary circulations as in equation (14) is at this point very difficult however because the measurements do not suffice to derive  $\Gamma$ . For reasonable values of  $k_s$  ( $k_s \geq 2D_{90}$  and  $k_s \leq 0.068$ ) the effect of secondary circulations as a residual term varies significantly with standard deviations larger than the found average values themselves. Another process to consider including is the lateral exchange in the horizontal mixing layer. The velocity gradient in the flume are very small however, which limits our ability to estimate the width of the mixing layer and estimate the magnitude of the empirical factor  $\beta$ . With no observed large turbulent eddies in the simulations it is expected that dissipation in the horizontal mixing layer is very small and that not modelling the horizontal mixing layer will not make much of a difference.

Later investigations capturing 3D velocities could verify the influence of secondary circulations. For the purpose of assessing the groyne resistance the residual resistance of the flume in the case without groynes is assessed applying different values for the bed roughness height  $k_s$  for the main channel and the groyne field. This is done by separately solving the compound channel momentum equations on the measured water level slopes and flow velocities. The obtained residual roughness height for the main channel and the floodplain  $k_s = 0.042 \pm 0.002$  m. The obtained residual roughness height in the groyne field  $k_s = 0.012 \pm 0.002$  m. The large difference between both values needs further investigation so that different physical processes can be distinguished and included in the momentum balance in other terms than  $k_s$ . The predicted water level slopes are shown in Figure 67 and the predicted discharge distributions are shown in Figure 68. The water level slopes and discharge distributions are predicted well for the high water levels for which the simulations with groynes are done. For that reason these values will be used to assess the groyne resistance, bearing in mind that extra work is needed to better represent the different physical processes acting in the flume.

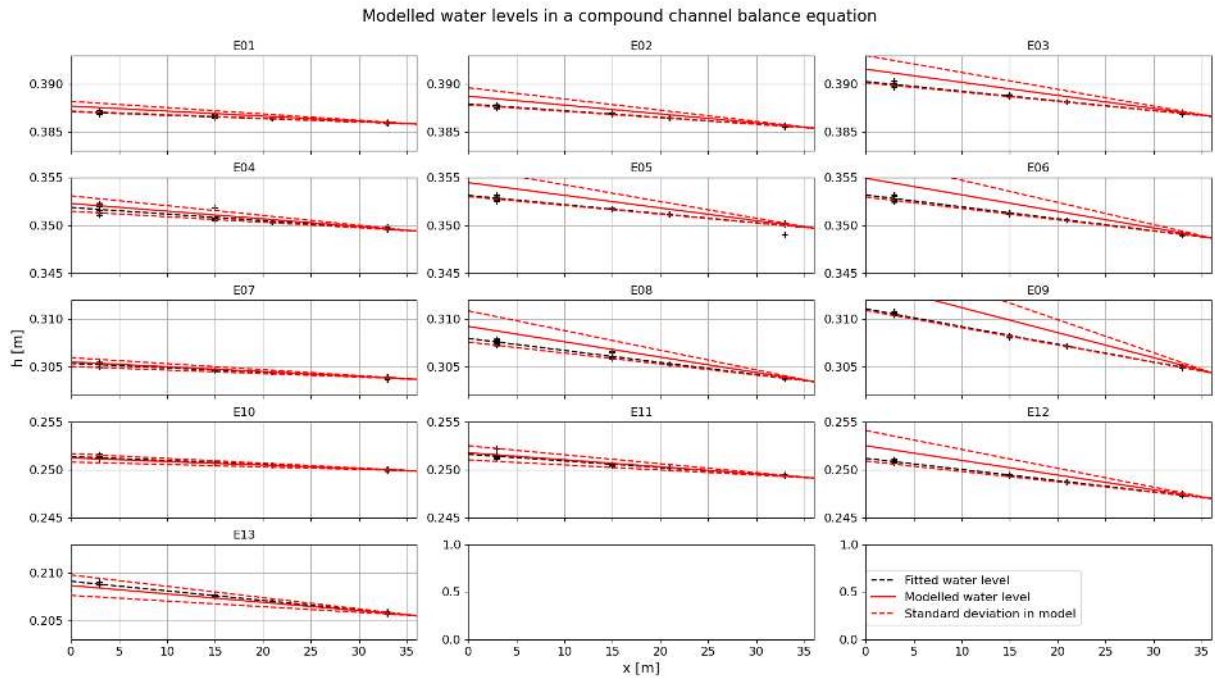


Figure 64; modelled water level slopes using  $k_s = 0.068 \pm 0.031$  m.

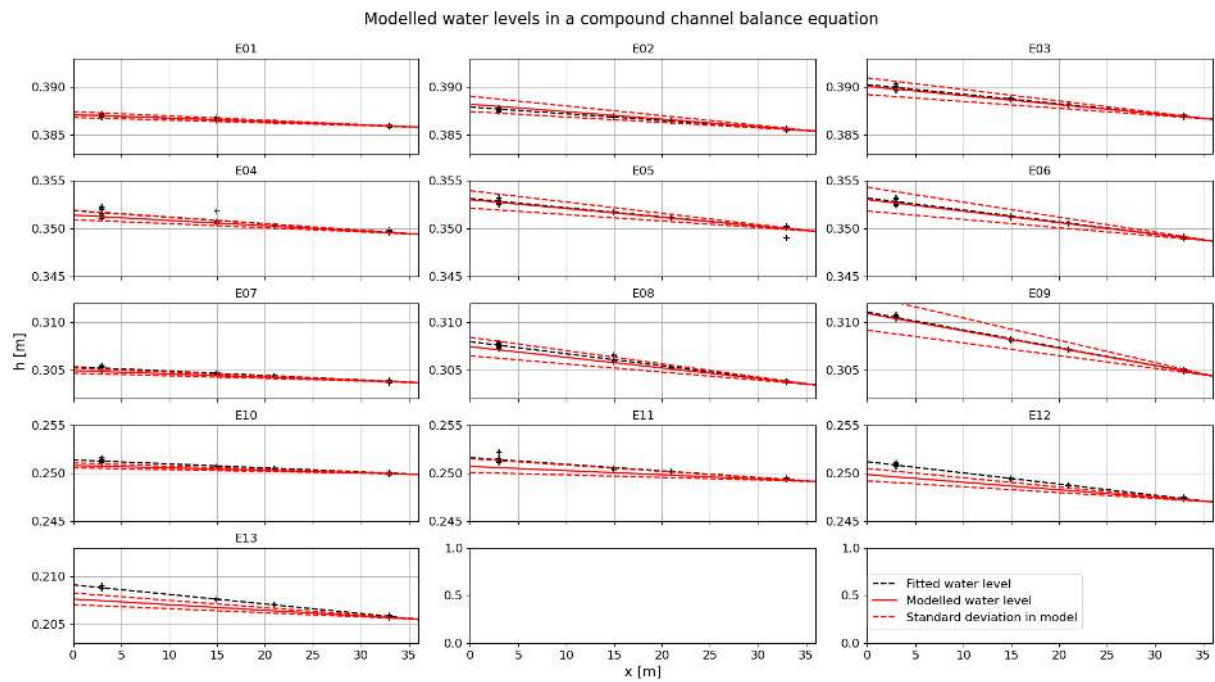


Figure 65; modelled water level using  $k_s = 0.032 \pm 0.015$  m.

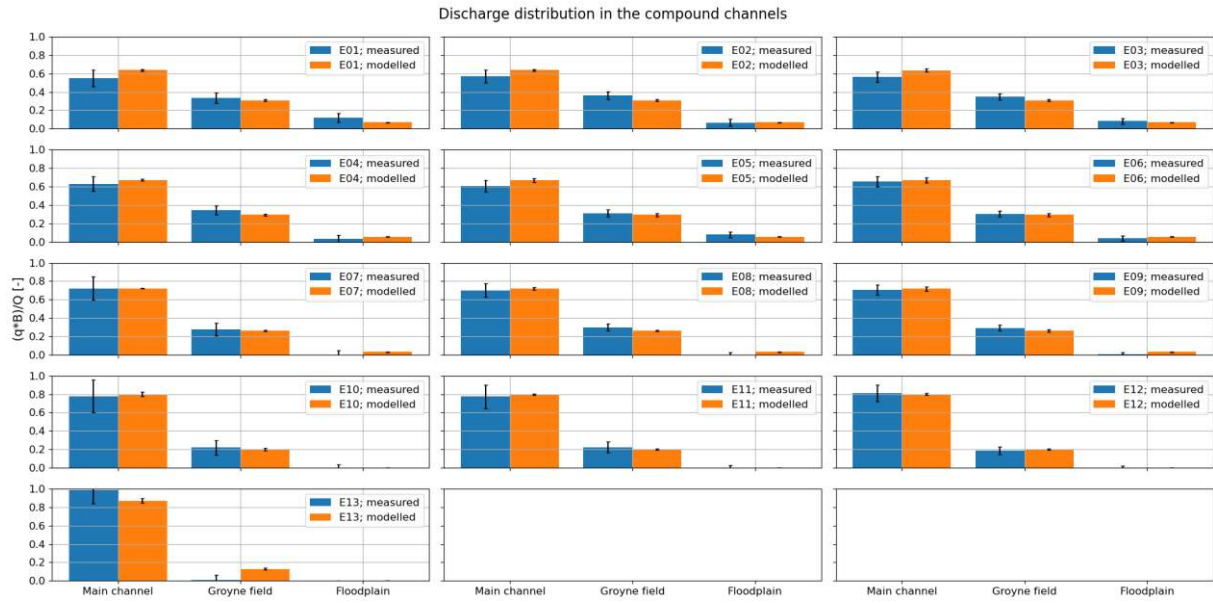


Figure 66; modelled discharge distribution in the compound channel using  $k_s = 0.032 \pm 0.015 \text{ m}$ .

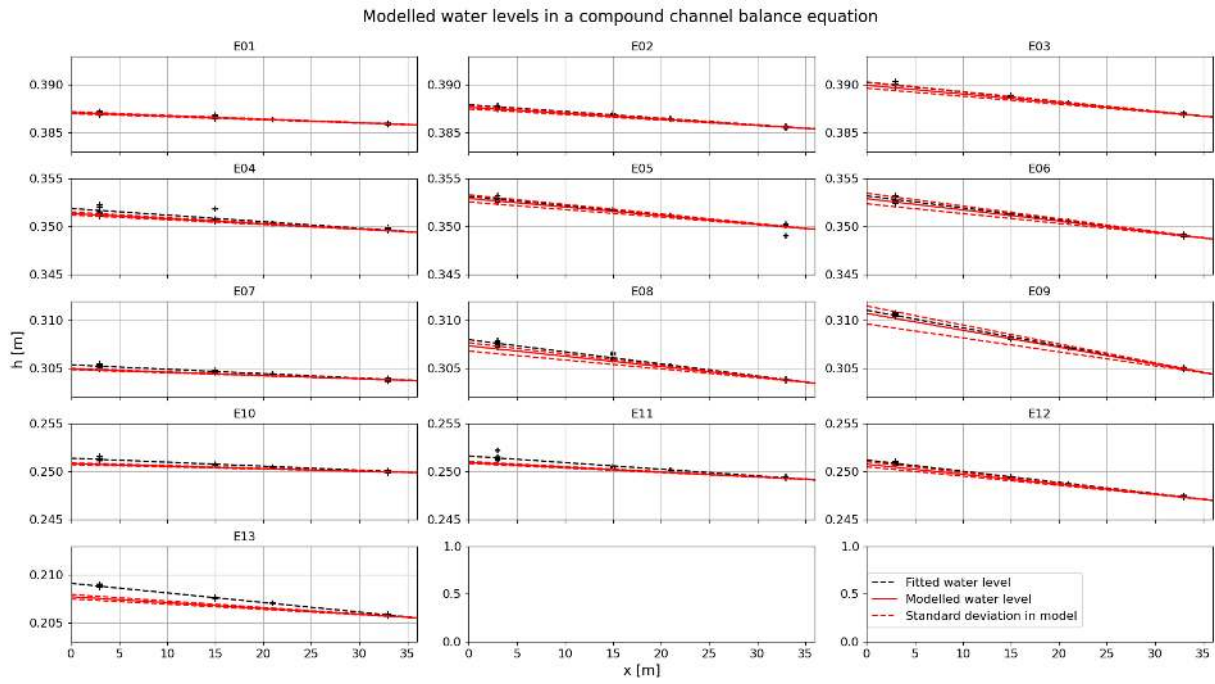


Figure 67; modelled water level slopes in the compound channel using  $k_s = 0.042 \pm 0.002 \text{ m}$  in the main channel and floodplain and  $k_s = 0.012 \pm 0.002 \text{ m}$  in the groyne field.

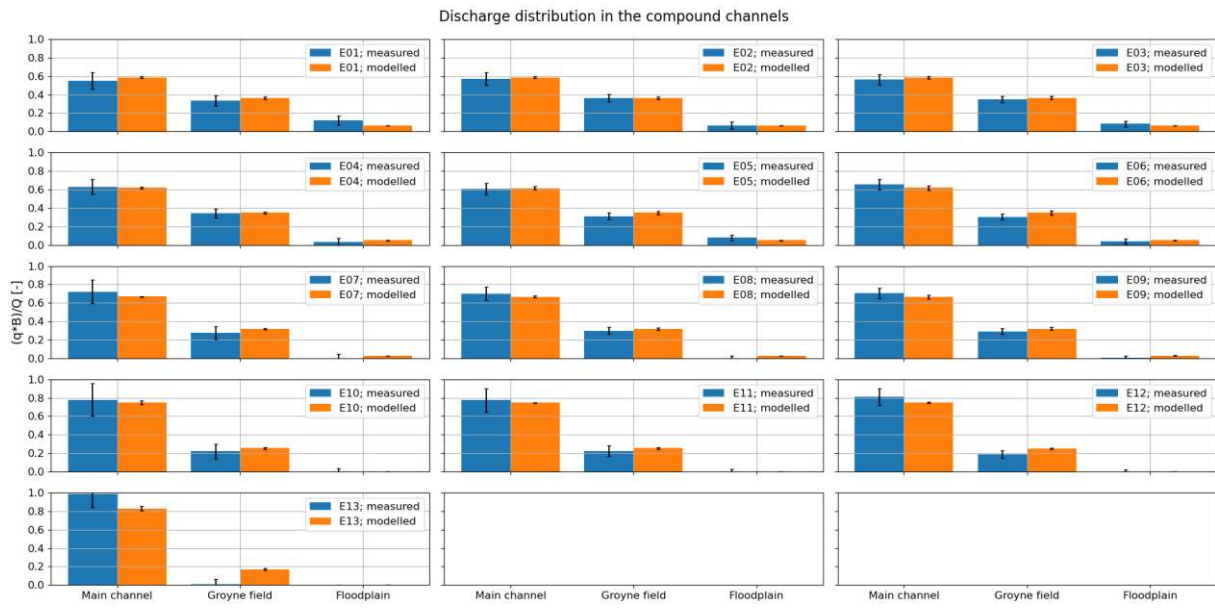


Figure 68 modelled discharge distributions in the compound channel using  $k_s = 0.042 \pm 0.002 \text{ m}$  in the main channel and floodplain and  $k_s = 0.012 \pm 0.002 \text{ m}$  in the groyne field.

## Appendix H

### Determination theoretical bottom friction height assuming fully developed one-dimensional flow

In this appendix additional analysis are done to determine the bed friction factors that is related to the logarithmic flow profile in fully developed one-dimensional flow. In the first part the procedure to get bed friction values is explained. After that the resulting friction parameters are determined. Lastly the accuracy of the methods of determining the bed shear stress are assessed.

#### Procedure fitting the Law of the Wall

When determining the different component of the flow resistance one needs a value for the boundary condition at the bottom, empirical values are required which enables us to determine the bed shear stress. Besseling (2021) concluded that the bed roughness for this specific experiment can be determined fitting the vertical streamwise velocity profile to the Law of the Wall (eq (11)):

$$\frac{u(z)}{u_*} = \frac{1}{\kappa} \ln \frac{z}{z_0}$$

The result of fitting a vertical flow profile is a bed shear velocity  $u_*$  and a zero point  $z_0$ , the point where the idealized velocity profile goes to zero. Besseling found a Manning  $n = 0.0245 \text{ s/m}^{1/3}$  or a Nikuradse roughness height  $k_s = 0.059 \text{ m}$  for this geometry. These values were derived using 16 respectively 12 flow profiles with a water level of  $40 \text{ cm}$ , and includes only flow profiles in the main channel.

As our experiment includes more water levels and focusses on all regions of the flume the same fitting of the Law of the Wall is done on the velocity points where reasonably developed wall flow can be assumed. Locations that are considered are far from the inflow, and not in a mixing layer. Also the velocity profiles at  $y = 4.6 \text{ m}$  (outside the mixing layer in the floodplain) are not taken into account due to device malfunctioning. The used vertical streamwise velocity profiles are from the simulations E1 - E13 at the streamwise location  $x = 15, 21, 33 \text{ m}$  and the transverse locations  $y = 0.5, 1.3, 2.6, 3.0, 3.4 \text{ m}$ . The results of the fitting of the Law of the Wall are shown in Figure 69.

For the modelling of bed shear stress single roughness parameters are desired which can be used in their respective method of calculating the bed roughness. The models that are considered are using a Chezy coefficient  $C$  or are using a Manning  $n$ :

$$\tau_b = \frac{\rho g}{C^2} U^2 \quad (73)$$

$$\tau_b = n^2 \frac{\rho g}{\sqrt[3]{d}} U^2 \quad (74)$$

When using (76) one can choose to implement a single roughness  $C$ , or derive this from the roughness height, as done by Colebrook and White (Colebrook & White, 1937):

$$C = 18 \log \frac{12d}{k_s} \quad (75)$$

Here the friction parameter to be determined is the roughness height  $k_s (= 30z_0)$ , which is supposed to be a property of the bed, and not of the flow, which isn't necessarily the case for the Manning  $n$  or using a single Chezy value.

From the obtained shear velocity and the mean flow velocity and water depth at each point the two different friction parameters are determined, the Chezy number  $C$  and Manning  $n$ :

$$C = \frac{U}{u_*} \sqrt{g} \quad (76)$$



$$n = \frac{u_* \sqrt[6]{d}}{U \sqrt{g}} = \frac{\sqrt[6]{d}}{C} \quad (77)$$

The results of fitting the Law of the Wall are therefore a constant Nikuradse roughness height  $k_s$ , a constant Chezy coefficient  $C$  and a constant Manning coefficient  $n$ . The use of a single Chezy coefficient is equivalent to using a single dimensionless friction coefficient  $c_f$ ,  $f$  or  $\lambda$ . Most commonly used methods of determining the bed roughness are covered this way. Having obtained values of those parameters the performance of the different methods is tested against the bed friction in each point using the friction velocity:

$$\tau_b = \rho u_*^2 \quad (78)$$

Comparing the uncertainty of the different roughness values and the accuracy of the predicted bed roughness versus the bed roughness as obtained from fitting the Law of the Wall one can finally conclude on the best method of determining the bed shear stress at every velocity point.

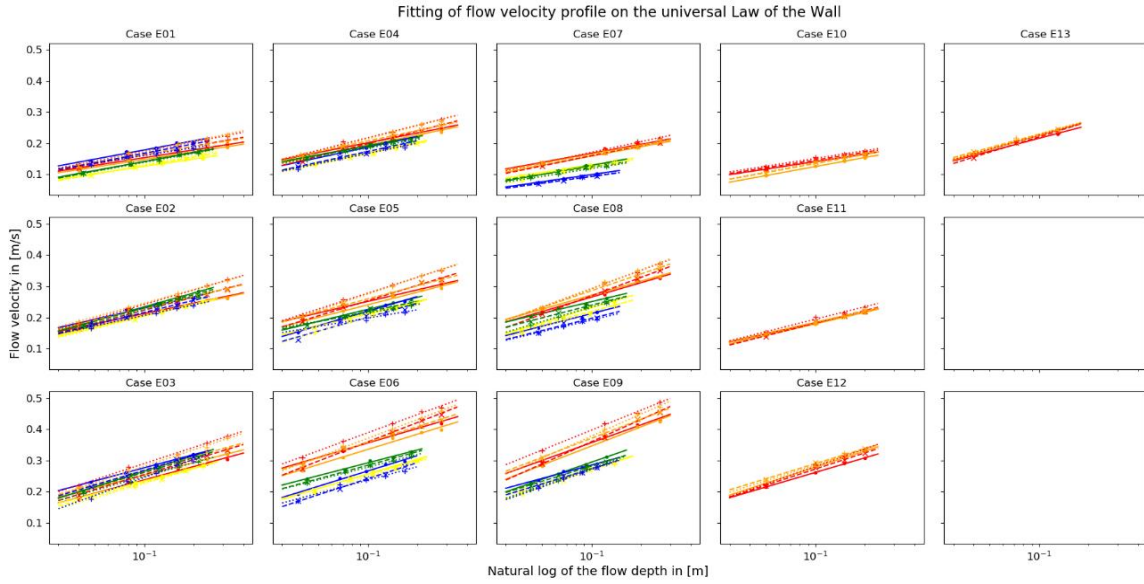


Figure 69; Results of fitting the Law of the Wall to each vertical streamwise flow profile

### Obtained friction factors

The fitting results in a shear velocity  $u_*$  and a zero point  $z_0$  for each flow profile. These quantities are plotted against the water depth and mean flow velocity in Figure 70. The  $z_0$  is shown in a more useful form  $k_s (= 30z_0)$ , the Nikuradse roughness height. The corresponding  $C$  and  $n$  are also shown in Figure 70.

Generally friction factors depend on the water depth and mean flow velocity. This can be seen by the division of the shear velocity with the mean flow velocity  $u_*/U$ . The dependency on the water depth is taken into account in the Manning  $n$  in  $\sqrt[6]{d}$ . This is not the case when using the Chezy number  $C$ , or equivalent dimensionless friction numbers  $c_f$ ,  $f$  or  $\lambda$ .

The effect of not taking the dependency of the water depth into account is visible in Figure 70, where the use of a single Chezy value clearly does not represent the data well when plotted for different water levels.

The roughness height  $k_s$  and the Manning  $n$  show no clear dependency on the water level or mean flow velocity, making them preferable above using a single Chezy  $C$ . The standard deviation of the obtained  $k_s$  is large however, with the coefficient of variation  $CV = 0.46$ , while for  $n$  the  $CV = 0.12$ .

Otherwise the derived friction parameters are:

- Chezy  $C$ :  $\mu_C = 31 \text{ m}^{1/2}/\text{s}$   $\sigma_C = 5 \text{ m}^{1/2}/\text{s}$
- Roughness height  $k_s$ :  $\mu_{k_s} = 0.068 \text{ m}$   $\sigma_{k_s} = 0.031 \text{ m}$
- Manning  $n$ :  $\mu_n = 0.026 \text{ s}/\text{m}^{1/3}$   $\sigma_n = 0.003 \text{ s}/\text{m}^{1/3}$

The values  $n$  and  $k_s$  as found by Besseling ( $n = 0.0245$ ,  $k_s = 0.059$ ) fall well within the uncertainty bounds of the here derived values for  $n$  and  $k_s$ . For the analysis of the obtained bed shear stress the here derived values are used ( $n = 0.026$ ,  $k_s = 0.068$ ).

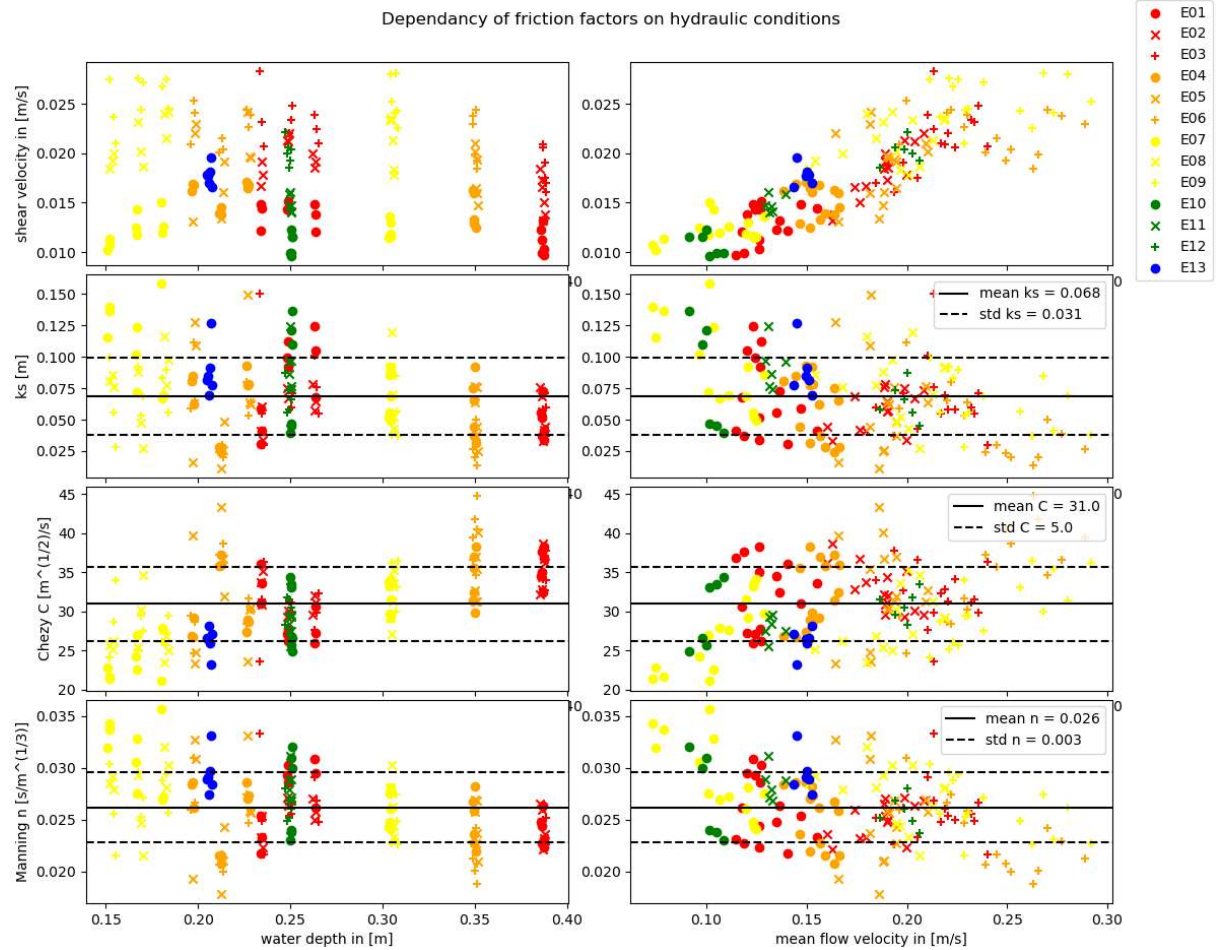


Figure 70; Plots of obtained bed friction factors over the water depth and mean flow velocity. From top to bottom: shear velocity  $u_*$ , Nikuradse roughness height  $k_s$ , Chezy smoothness coefficient  $C$  and Manning's roughness coefficient  $n$ . Different colors and marker style indicate different experiments. The mean value and bounds of one standard deviation are shown also for the  $k_s$ ,  $C$  and  $n$ .



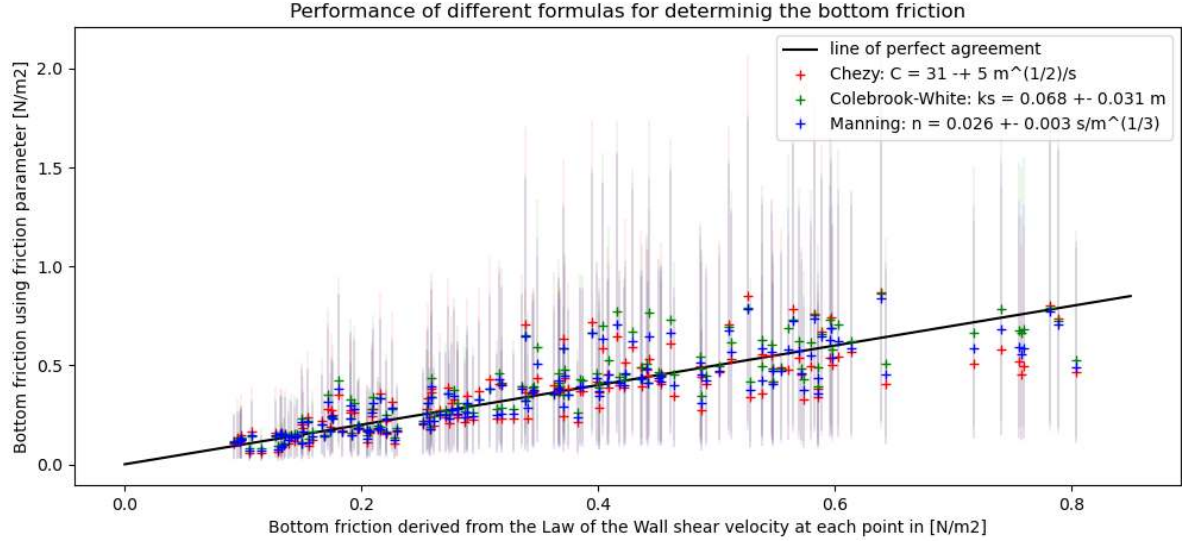


Figure 71; Comparison of calculated bed shear stress using empirical formulations over the bed shear stress as defined by the shear velocity obtained from fitting the Law of the Wall. The limits of the uncertainty bounds are the calculated bed shear stress using the one standard deviation of the derived variables  $C$ ,  $n$  and  $k_s$ .

### Bed shear stress modelling

In this chapter the performance of the bed shear stress models is tested using the above derived empirical friction factors,  $C$ ,  $n$  and  $k_s$ . All empirical friction factors enter on different places in their method of determining the bed shear stress. The quality of the models is bed shear stress models is assessed by comparing them to the bed shear stress as obtained from the local friction velocity. The comparison of these methods are visualized in Figure 71.

The reference data for the bed shear stress is obtained from the definition of the local shear velocity:

$$\tau_b = \rho u_*^2$$

The predictive models are:

- Chezy:  $\tau_{b:C} = \frac{\rho g}{C^2} U^2$ ;  $C = 31 \pm 5 \text{ m}^{1/2}/\text{s}$
- Colebrook-White:  $\tau_{b:k_s} = \frac{\rho g}{C^2} U^2$ ;  $C = 18 \log \frac{12d}{k_s}$ ;  $k_s = 0.068 \pm 0.031 \text{ m}$
- Manning:  $\tau_{b:n} = n^2 \frac{\rho g}{\sqrt[3]{d}} U^2$ ;  $n = 0.026 \pm 0.003 \text{ s/m}^{1/3}$

A good predictive model has a small bias, small error and is robust regarding sensitivity of uncertainty in the empirical values. For the assessment of the bias and the robustness the Symmetric Signed Percentage Bias (Morley, Brito, & Welling, 2017) is determined for each model using the mean value and the values  $\pm 1$  standard deviation. Here a model is regarded robust when the bias is small using the standard deviation of the empirical factors. The error is assessed using the Median Symmetric Accuracy (Morley, Brito, & Welling, 2017). The Median Symmetric Accuracy and the Symmetric Signed Percentage Bias are defined as, respectively:

$$e^{\text{Median}(|\ln \frac{\tau_{b:\text{model}}}{\tau_b}|)} - 1 \quad (79)$$

$$\text{signum} \left( \text{Median} \left( \ln \frac{\tau_{b:\text{model}}}{\tau_b} \right) \right) * \left( e^{\text{Median}(|\ln \frac{\tau_{b:\text{model}}}{\tau_b}|)} - 1 \right) \quad (80)$$

The resulting Median Symmetric Accuracy and the Symmetric Signed Percentage Bias for each model is:

Chezy:

- Median Symmetric Accuracy for  $C = 31 \text{ m}^{1/2}/\text{s}$ : 0.27
- Symmetric Signed Percentage Bias for  $C = 31 \text{ m}^{1/2}/\text{s}$ : -0.06
- Symmetric Signed Percentage Bias for  $C = 36 \text{ m}^{1/2}/\text{s}$ : -0.43
- Symmetric Signed Percentage Bias for  $C = 26 \text{ m}^{1/2}/\text{s}$ : 0.34

Colebrook-White:

- Median Symmetric Accuracy for  $k_s = 0.072 \text{ m}$ : 0.16
- Symmetric Signed Percentage Bias for  $k_s = 0.072 \text{ m}$ : 0.04
- Symmetric Signed Percentage Bias for  $k_s = 0.040 \text{ m}$ : -0.29
- Symmetric Signed Percentage Bias for  $k_s = 0.104 \text{ m}$ : 0.30

Manning:

- Median Symmetric Accuracy for  $n = 0.027 \text{ s}/\text{m}^{1/3}$ : 0.19
- Symmetric Signed Percentage Bias for  $n = 0.027 \text{ s}/\text{m}^{1/3}$ : 0.04
- Symmetric Signed Percentage Bias for  $n = 0.024 \text{ s}/\text{m}^{1/3}$ : -0.21
- Symmetric Signed Percentage Bias for  $n = 0.030 \text{ s}/\text{m}^{1/3}$ : 0.29

## Discussion

Having a measure for the bias, error and robustness a choice has to be made on which model to use for modelling the bed shear stress.

Firstly using a single friction factor  $C$  neglects the influence of the water level on the bed friction. The bias of the model using  $C$  is very small, but this is due to overfitting on the available data.  $1/C \sim u_*$  therefore using a mean value of the friction velocity will give the same mean value as averaging multiple friction velocities that determined  $C$ . The low accuracy of using  $C$  shows the shortcoming of this method, with an error of 27%. Using smaller and larger values of  $C$  also results in a large bias. Overall the method has bad predictability and isn't robust.

Using Colebrook-White and the roughness height  $k_s$  is the most accurate of the three methods. It does have a small bias, which is of less relevance however as the bias is far smaller than the accuracy. Using larger and smaller values of  $k_s$  resulted in a moderate error. This shows that the method is quite robust regarding uncertainties in the  $k_s$ , as the deviating values of  $k_s$  deviate quite from the average  $k_s = 0.068 \text{ m}$ . This is due to the way  $k_s$  is implemented in determining the bed shear stress, in the logarithm.

The use of Manning  $n$  gives slightly less accurate results than using Colebrook-White, with an equal bias. Implementing deviating values of  $n$  result in a moderate error, with larger values of  $n$  inducing a larger error. For smaller  $n$  the bias is smaller than when using smaller  $k_s$ . The deviations in the value of  $n$  were rather small, the Manning  $n$  had the smallest standard deviation of the three variables. The error upon implementing the standard deviation isn't small however, indicating a less robust model regarding uncertainties in  $n$ . This is due to the way  $n$  is implemented with  $\tau_b \sim n^2$ .

The choice is between the use of the Colebrook-White formula with  $k_s = 0.068 \pm 0.031 \text{ m}$ , and the use of Manning's formula with  $n = 0.026 \pm 0.003 \text{ s}/\text{m}^{1/3}$ . The first approach gives the smaller error and is robust regarding uncertainty in the friction factor. The second formula uses a friction factor with only a small standard deviation. Both options seem viable.

## Appendix I

### Photo's of physical model and measurement equipment



Figure 72; Picture of physical model taken from the downstream end



Figure 73; inflow region with the blue flow straighteners, and white wave dampers





Figure 74; Inflow region taken from the flow straighteners. On the right the inflow from the pump. The inflow is divided into two parts: behind a turbulent region where the water flows in, which overflows into the region here the flow enters the physical model



Figure 75; downstream boundary, divided from the physical model by netting to prevent PTV tracking particles from entering the reservoir or the pump





Figure 76; Behind the netting is the outflow. On the left the pump which is the main outflow and determined the amount of discharge through the flume. Right of it is the inflow from the water reservoir, which is used to fill the physical model and is used to compensate water leakage in the experiment. Left is the overflow weir to the reservoir, which keeps the water level constant.



Figure 77; The side wall at the main channel side is concrete for the largest part and a part glass





Figure 78; the side wall at the floodplain side are wooden planks



Figure 79; the measurements carriage, with 6 EMS installed and 3 laser altimeters installed



*Figure 80; The EMS on the right, the laser altimeter on the left. The altimeter measures a the distance between a set reference to a paper floating of the surface of the water.*



*Figure 81; gravel bed of the experiment with approximately 5500 stones per square meter*



*Figure 82; Picture of groyne in the model*